Modelling and Short-Term Forecasting of High Wind Speed Events at Operational Wind Farms

by

Matthew Groch

Dissertation presented for the degree of Doctor of Philosophy in the Faculty of Engineering at Stellenbosch University

Professor H. J. Vermeulen

December 2019

Declaration

By submitting this dissertation electronically, I declare that the entirety of the work contained therein is my own, original work, that I am the sole author thereof (save to the extent explicitly otherwise stated), that reproduction and publication thereof by Stellenbosch University will not infringe any third party rights and that I have not previously in its entirety or in part submitted it for obtaining any qualification.

Date: December 2019

Abstract

The increasing penetration of wind energy has prompted a reform of the prototypical operational practices of conventional power systems, especially systems dominated by thermal generation sources. The variable nature of wind energy generation requires that further investments be made into more flexible plant with faster start-up capabilities to safeguard against potential shortfalls in generation. These rapid response services are dispatched by the System Operator in reaction to large power ramps to ensure that energy balance is maintained. Rapid response services, however, typically assumes the form of storage or gas turbines, which are procured at a high cost.

In the context of wind power ramping phenomena, High Wind Speed Shutdown (HWSS), potentially, represents the most severe risk to power system stability. It is clear from the available literature, that HWSS has not been extensively investigated to date. Although the need for forecasting and quantification of the impacts of HWSS feature strongly in the available literature, no models have thus far been formulated to describe this phenomenon, and no event-based forecasting models have been proposed in response to this research question.

This dissertation targets two major aspects of HWSS, namely the modelling, quantification, and comparison of the relative risk of HWSS events, and the short-term operational forecasting of HWSS events. It is evident from the literature that the development of a dedicated HWSS forecasting model will assist in the management and mitigation of the short-term risk associated with HWSS events. The development of site-specific models with which to quantify and compare temporal risk will, furthermore, aid in the siting of wind farms in regions with a low susceptibility for HWSS events.

Two novel event-based forecasting techniques are proposed for the short-term forecasting of HWSS events, namely an Artificial Neural Network (ANN) model approach, and a hybrid model using an original statistical downscaling methodology. Both of the proposed model topologies utilise an ensemble wind speed forecast derived using the Weather Research and Forecasting (WRF) model, as well as additional environmental variables such as wind direction and temperature. The results prove that both models demonstrate good accuracy for the forecasting of localised high wind speed events which occur at the micro-scale level, which is in line with HWSS events.

A technique is proposed for site characterisation and comparison of HWSS events for wind farm site planning. The proposed technique utilises a probabilistic spatial wind speed distribution to determine turbine-level wind speeds. A rule-based methodology is applied to extract HWSS events from micro-scale wind speeds. The resulting binary event series is analysed using survival theory to create a time-to-event model for subsequent analysis and relative probabilistic comparison of risk between sites.

Uittreksel

Die toenemende indringing penetrasie van windenergie het daartoe gelei dattot verandering in die gewone operasionele praktyke van konvensionele kragstelsels, veral stelsels wat deur termiese kragstasies oorheers word, hervorm word. Die veranderlike eienskappe aard van windenergie kragopwekking vereis dat verdere beleggings in meer buigsame aanlegte met vinniger aanlegvermoë aktiveringsvermoë gedoen gemaak moet word om teen moontlike tekorte aan kragin opwekking te beskerm. Hierdie stelsel vir vinnige reaksiedienste word deur die stelseloperateur ingeskakel na aanleiding van groot krag verhoogings toenamesveranderings om te verseker te maak dat die energiebalans gehandhaaf word. Vinnig reaksiedienste aanvaar neem tipies die vorm van berging of gasturbines, wat teen 'n hoë koste verkry word.

In die konteks van die oprit van windkrag veranderingsverskynsels, is die hoë windsnelheidsuitsetting windsnelheidsafskakeling (HWSS) moontlik die ernstigste grootste risiko wat die stabiliteit van die kragstelsel kan beinvloed. Dit is duidelik vanuit die beskikbare literatuur dat HWSS tot op hede nog nie breedvoerig ondersoek is nie.Uit die beskikbare literatuur verskyn dit dat HWSS tot op hierdie punt nog nie volledig ondersoek is nie. Alhoewel die behoefte aan voorspelling en kwantifisering van die impak van HWSS sterk in die beskikbare literatuur voorkom, daar is daar tot dusver geen modelle geformuleer om hierdie verskynsel te beskryf nie, en daar is geen gebeurtenisgebaseerde -voorspellingsmodelle in antwoord op hierdie navorsingsvraag voorgestel nieontwikkeld.

Hierdie proefskrif fokus op twee belangrike hoof aspekte van HWSS, naamlik die modellering, kwantifisering en vergelyking van die relatiewe risiko van HWSS-gebeure, en die korttermyn operasionele voorspelling van HWSS-gebeure. Uit die literatuur is dit duidelik dat die ontwikkeling van 'n pasgemaakte HWSS-voorspellingsmodel sal bydra bystand verleen totmet die bestuur en verligting vermidering van die korttermynrisiko wat met HWSS-gebeure verband hou. Die ontwikkeling van liggingspesifieke modelle waarmee tydelike tydgebonde risiko gekwantifiseer en vergelyk kan word, sal verder help met die plasing van windplase in gebiede met 'n lae waarskynlikheid vir HWSS-gebeure.

Twee nuwe gebeurtenisgebaseerde gebeurtenisgebaseerde-voorspellingstegnieke word voorgestel vir die korttermynvoorspelling van HWSS-gebeure, naamlik 'n Kunsmatige Neurale Netwerk (ANN) - benadering, en 'n bastermodel hibriedmodel met behulp van 'n oorspronklike statistiese afskaleringafmetingsmetodologie. Beide van die voorgestelde modeltopologieë gebruik ‘n verskeidenheid windspoedvoorspellings wat afgelei is met behulp van die Weather Research and Forecasting (WRF) model, sowel as addisionele omgewingsveranderlikes soos windrigting en temperatuur. Die resultate bewys dat beide modelle 'n goeie akkuraatheid toon vir die voorspelling van 'n hoë windsnelheid gebeur afgelei op mikroskaalvlak, wat ooreenstem met die voorspelling van

HWSS-gebeuregelokaliseerde gebeure met 'n hoë windsnelheid wat op mikroskaalvlak plaasvind.

'n Tegniek word voorgestel vir die area karakterisering en vergelyking van HWSS-gebeure vir die plasingsbeplanning van windplase. Die voorgestelde tegniek maak gebruik van 'n probabilistiese waarskynlike ruimtelike windsnelheidsverspreiding om windsnelhede op turbine-vlak te bepaal. 'n Reëlgebaseerde metodologie word toegepas om HWSS-gebeure uit mikroskaal-windsnelhede te onttrek. Die resulterende reeks van binêre opsies word met behulp van oorlewingsteorie geanaliseer om 'n tyd-tot-gebeurtenis-model te skep vir daaropvolgende ontleding en relatiewe probabilistiese waarskynlike vergelyking van risiko tussen windplaseareas.

Acknowledgements

First and foremost, I would like to thank my supervisor, Professor H. J. Vermeulen, for being an excellent mentor. I am deeply grateful for your incredible guidance and support.

I would like to acknowledge my colleges from E222, most notably Chantelle Janse van Vuuren. Thank you for the coffee breaks, for tolerating my cluttered work space, and for all of the interesting discussions. I would also like to thank Nelius Bekker for all of the advice, and willingness to assist whenever I was in need of help.

I am grateful to the following people and organisations for their technical and financial support. The Center for High Performance Computing (CHPC) for the computing resources for the forecasting simulations. Charles Crosby at the CHPC for his assistance with the WRF simulations. The Council for Science and Industrial Research (CSIR) for the wind reanalysis dataset. Dr. Bernard Bekker for assisting in the procurement of the wind farm data, and the Center for Renewable and Sustainable Energy Studies (CRSES) for funding my research.

Words cannot express how grateful I am to my mother. Thank you for encouraging me in all of my pursuits, for being my biggest supporter, and for the countless sacrifices you have made over the years which ultimately led to this point.

And finally to Caileigh for your support and understanding. You were by my side throughout, and experienced every minute of the journey with me. Thank you for picking up the slack, for granting me the freedom to put in the necessary time, for accepting the working weekends, the cancelled plans, the late nights and the early mornings without complaint. Without you, and your unwavering support, this truly would not have been possible.

Table of Contents

List of Figures

List of Tables

Nomenclature

Abbreviations

ACM2	Asymmetric Convective Model version 2
AI	Artificial Intelligence
ANN	Artificial Neural Network
AR	Auto Regressive
ARIMA	Auto Regressive Integrated Moving Average
ARMA	Auto Regressive Moving Average
CAM	Community Atmospheric Model
CFD	Computational Fluid Dynamics
ECMWF	European Center for Medium-Range Weather Forecasts
GFS	Global Forecasting System
HR	Hazard Ratio
HWRT	High Wind Ride-Through
HWSS	High Wind Speed Shutdown
IQR	Inter-Quartile Range
MA	Moving Average
MAE	Mean Absolute Error
MAPE	Mean Absolute Percentage Error
MCC	Meso-scale Convective Complex
MM5	Fifth generation Meso-scale model
MVPT	Mean-Variance Portfolio Theory
MYJ	Mellor-Yamada-Janjic
NCC	National Control Center
NWP	Numerical Weather Prediction
PBL	Planetary Boundary Layer
PH	Proportional Hazards

PSO	Particle Swarm Optimisation
PV	PhotoVoltaic
RMSE	Root Mean Squared Error
RRTM	Rapid Radiative Transfer Model
WASA	Wind Atlas of South Africa
WPS	Weather Research and Forecasting Pre-processing System
WRF	Weather Research and Forecasting
WSM	Weather Research and Forecasting Single Moment

Chapter 1

Introduction

1.1 Overview

It is generally acknowledged that the incorporation of renewable energy sources such as wind energy introduces a degree of variability and uncertainty into the power generation mix, the severity of which depends on the penetration level of the renewable component. The variability of renewable generation also induces variability in the residual load profile, i.e. the cumulative load profile less the renewable generation component. This has operational implications for the conventional dispatchable generation fleet which must serve the residual load, particularly in the South African context where interties cannot be relied upon.

The variable residual load profile associated with renewable energy gives rise to more frequent cycling and ramping of the conventional generation plants, increased use of expensive peaking plants, and an elevated risk of load shedding. Conventional stations, consequently, incur increased maintenance costs due to the shorter maintenance intervals associated with increased wear and tear [1]. The negative impacts of the variable residual load profile intensifies with increased penetration of renewables, and are further compounded by increased geographical concentration of renewable plants such as wind and solar PhotoVoltaic (PV) farms. Greater flexibility of the dispatchable fleet is required to service the more frequent and stringent ramp-rate requirements [2]. The increased stochasticity associated with high wind penetration levels, furthermore, increases the risk to power system security [3], [4]. In the context of wind energy, the most severe changes in generation typically occurs as a result of rapid changes in wind speed, i.e. wind speed ramps, and High Wind Speed Shutdown (HWSS) protection activation. Under normal operating conditions, the ramping phenomenon predominantly affects dynamic or small-signal stability [5]. HWSS is commonly associated with severe weather fronts and potentially represents the most hazardous scenario [6] - [8]. Case studies suggest that generation can change from maximum to zero active power output in a matter of minutes. Cutululis *et al.*, [9] for instance, reports that 1500 MW is at risk within 30 minutes in the Danish power system.

The negative impacts associated with the increased variability can be mitigated by effective short-term forecasting [10], [11]. It is postulated, furthermore, that wind farms may be sited such that the impacts of ramping on the grid are reduce to optimal levels.

Despite the relatively short history of wind forecasting, there exists a plethora of forecasting techniques which can be employed [12]. Research in wind farm forecasting applications has experienced exponential growth in recent years, driven by the commercial and environmental interests that propel the proliferation of wind energy in many countries across the globe. Forecasting techniques are

generally formulated to minimise errors over long periods, typically for the duration of a month or longer, with the aim of fine-tuning the model for an accurate holistic forecast. This is partially driven by the need to determine the aggregated yield in the short-term horizon for optimal scheduling and dispatch, energy trading, etc. Event-specific forecasting has, however, recently gained traction with the increasing penetration of renewables [13]. Probabilistic event-based forecasting offers clear benefits as a supplementary aid to the deterministic forecast of aggregated yield. A dedicated probabilistic ramp-event forecasting tool, for instance, has the potential to assist the System Operator in timeous implementation of optimal pre-emptive actions, such as efficient dispatch and scheduling, and optimal allocation of ancillary services [14].

The research described in this dissertation focuses specifically on the modelling, analysis, and forecasting of site-specific HWSS events.

1.2 High Wind Speed Shutdown

1.2.1 Overview

HWSS events occur when the wind speeds experienced by individual turbines exceed protection thresholds. Figure 1 illustrates the operational principles associated with HWSS protection logic for a typical turbine power curve. For the given power curve, HWSS will occur under the following conditions [7]:

- The mean wind speed over a 10 minute sampling interval exceeds 25 ms^{-1}.
- The mean wind speed over a 30 second sampling interval exceeds 28 ms^{-1}.
- The instantaneous wind speed exceeds 32 ms^{-1}.

Following cut-out, the turbine will remain out of service until the mean wind speed over a 10 minute sampling interval drops below 20 ms^{-1}.

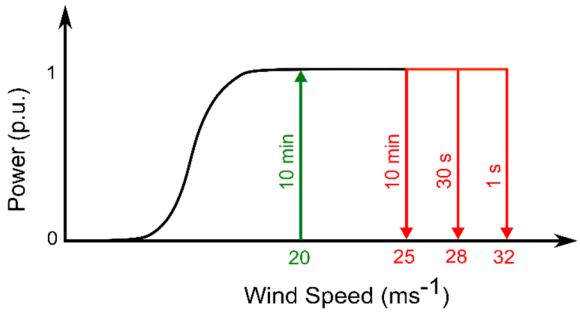

Figure 1. Power curve showing typical high wind speed shutdown protection logic [7].

The HWSS phenomenon has not been studied extensively in literature, but has attracted some recent attention in the form of empirical evaluations of the associated impact on the national grid.

1.2.2 Grid Impacts of HWSS Events Reported in Literature

Detlefsen *et al.* [8] investigated alternative methods to manage wind farms under storm conditions using the offshore Horns Rev 2 wind farm as a case study. The authors observed that offshore wind farms can shut down completely within 3 minutes due to the operation of HWSS protection. A storm management demonstration was undertaken using two approaches, namely a controlled system action for which there are several options, and the implementation of a Siemens High Wind Ride-Through (HWRT) controller. Multiple options are identified to mitigate severe imbalances if a storm that may impact the network is predicted. The authors suggest pre-emptive curtailment by either the wind farm owner, or the System Operator. This method requires accurate forecasting and efficient operational procedures to ensure minimal loss of power, safety of the network, equitable application amongst participants, and adherence to the grid code. The study showed that the HWRT controller allows turbines to stay connected to the grid for longer, which in turn results in a more gradual reduction in the wind farm power output. A disadvantage of this controller, however, is that a higher burden is placed on the turbine drive train, which reduces the life of the turbine.

Coughlan *et al.* [6] studied the effects of HWSS on the Irish national grid. The operating procedure implemented by the Irish National Control Center (NCC) is to treat a wind forecast in excess of 25 ms^{-1} as a potential HWSS situation. In these instances, the NCC assumes that 50% of the generation could be lost in the affected areas at any time. Data from 23 wind farms was analysed over the period of one year. The study showed that turbine availability due to HWSS, where an HWSS event is defined as more than 5 % of wind turbines in cut-out mode, varies substantially across sites.

Figure 2 shows a comparison of loss of generation due to HWSS events between wind farms connected to the Irish national grid for 2010. The results demonstrate that wind farm siting is of paramount importance, as the site impacted most severely experiences a loss of more than tenfold the cumulative megawatt hours compared to the site which was impacted the least severely. Table 1 shows an excerpt of the results presented for the empirically derived average percentage of turbines lost at a wind farm due to HWSS versus wind speed at various wind farms connected to the Irish national grid. The x indicates that the corresponding wind speed did not occur at the wind farm during the study period. The results show that wind farms experience HWSS events at different wind speeds. It is concluded that this is due to the different turbine models, as well as the layout of the wind farm.

The study, furthermore, reports the empirical time-delayed HWSS correlation between wind farm sites. Table 2 shows a subset of the data presented by Coughlin *et al.* [6]. The results represent the probability of shutdown at wind farms in one county following shutdown at pre-cursor wind farms within another county in intervals of 1 hrs, 2 hrs, 3 hrs, and 4 hrs. This type of analysis can assist an NCC in assessing risk and reserve requirements during the passage of a storm. The results demonstrate that site coincidence may be used as an input into risk-based forecasting, along with other factors such as wind

direction. This study concluded that a more in depth analysis of HWSS events is required, particularly in view of the increasing penetration of wind energy.

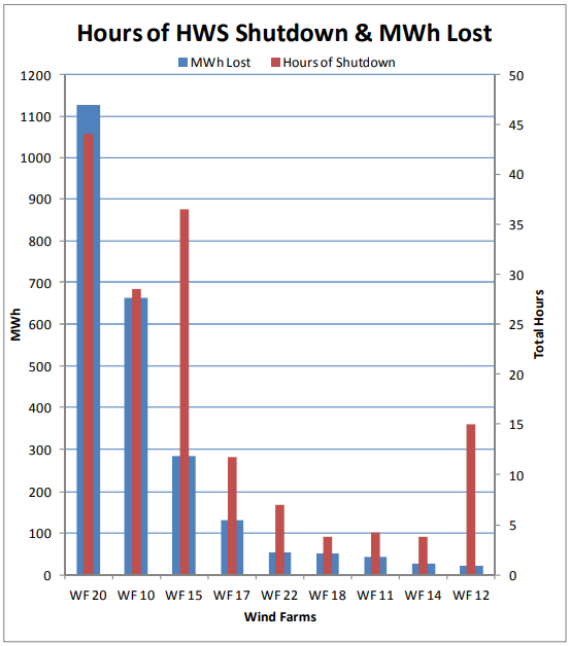

Figure 2. Megawatt hours lost due to HWSS events for wind farms connected to the Irish national grid in 2010 [6].

Table 1. Excerpt of the results presented for the empirically derived average percentage of turbines lost at a wind farm due to HWSS versus wind speed at various wind farms connected to the Irish national grid [6].

Wind Farm ID	Max Output (MW)	Wind Speed													
		18	19	20	21	22	23	24	25	26	27	28	29	30	31
20	86	0 %	4 %	10 %	30 %	47 %	50 %	50 %	50 %	50 %	75 %	80 %	100 %	100 %	100 %
13	60.3	0 %	0 %	0 %	0 %	0 %	0 %	0 %	0 %	0 %	0 %	0 %	0 %	0 %	0 %
9	60	0 %	0 %	0 %	0 %	0 %	0 %	x	x	x	x	x	X	x	x
6	57	0 %	0 %	15 %	15 %	15 %	15 %	20 %	60 %	70 %	70 %	70 %	70 %	85 %	85 %
18	56	0 %	0 %	0 %	6 %	6 %	39 %	39 %	x	x	x	x	X	x	x
5	48	0 %	0 %	0 %	0 %	0 %	5 %	18 %	x	x	x	x	X	x	x
10	45	0 %	0 %	0 %	27 %	27 %	47 %	86 %	93 %	93 %	93 %	93 %	93 %	93 %	93 %
3	42	0 %	0 %	0 %	0 %	0 %	0 %	0 %	0 %	x	x	x	X	x	x

Table 2. Empirically derived probability of the occurrence of time-delayed HWSS occurrence at wind farms in various counties in the Irish national grid [6].

Hour	County	Number of Windfarms	Number of Shutdown Events	Cavan	Clare	Cork	Donegal	Kerry	Limerick	Tipperary	Leitrim
1	Cavan	2	1							100 %	
	Cork	3	12					25 %			
	Donegal	4	8		13 %						13 %
	Kerry	7	16			6 %					
	Limerick	2	3		33 %		33 %				33 %
	Tipperary	1	2				50 %				
	Leitrim	1	9		11 %		22 %				

In September 2012, the grid code review panel of National Grid formed an HWSS workgroup to ascertain whether HWSS warranted any modifications to the UK grid code [15]. The investigation focused on the following concerns:

- The sudden disconnection of bulk wind generation over a short time period due to HWSS.
- The sudden reconnection of disconnected wind farms and, consequently, the resulting challenge in controlling the system frequency.
- The possibility of forecasting the probability and effect of HWSS events.
- The need to specify connection and disconnection rates for wind farms.

The workgroup report noted the following current and potential HWSS mitigation measures [15]:

- Implementation of a HWRT controller.
- Pre-emptive shutdown procedures.
- Bilateral agreements with wind farms.
- An internal HWSS forecast.

This report, furthermore, concluded that:

- HWSS does not currently warrant any changes to the grid code as events occur too infrequently and do not significantly impact the system. Wind farms shut down slowly as a weather front moves over.
- With the current penetration, the System Operator can respond to HWSS adequately. It is noted, however, that this must be reviewed in the near future as wind penetration increases.
- The increasing share of renewables is displacing synchronous generation, which equates to lower system inertia, and makes it more challenging for the System Operator to maintain a frequency balance.
- An improved HWSS forecasting model is required, as forecasting errors in excess of 1 GW can occur. This can also assist in reducing balancing costs.
- As the analysis was retrospective, the issue must be reviewed within two years.
- A measure of the probabilistic megawatts at risk, or unexpected reconnection, could be useful to the System Operator.
- HWSS experiences vary from country to country.

The workgroup concluded that there is currently adequate operational reserves in the UK to manage the generation losses due to HWSS events. It is also stated, however, that this may not be the case in the near future, as the share of renewable generation increases. Forecasting is identified as an area which requires advanced research.

MacDonald *et al.* [7] proposed the use of individual turbine cut-out events as early warning systems.

This study analyses measured data from two wind farms located approximately 180 km apart. The investigation concludes that HWSS does not always result in the shutdown of the entire wind farm. It is demonstrated that complete shutdown occurs approximately 5 to 10 % of the time that incidents occur at the sites in question. It is concluded that the ramp rates resulting from the loss of generation due to HWSS events poses a threat to power system security, and that this is also true for partial loss of the wind farm due to HWSS events. Over the 3 years and 5 months for which the study was conducted, 6 minutes was the fastest disconnection time for an entire wind farm due to HWSS.

1.3 Project Motivation

The key points highlighted by the above review of the literature pertaining to HWSS events can be summarised as follows:

- Site selection is of importance when considering HWSS. Some sites are prone to a high number of events, whereas others are not.
- The onset of HWSS events varies between sites due to terrain complexities, turbine placement, surface roughness, etc. Site-specific models are therefore required to model HWSS events.
- Some sites exhibit coincidence of HWSS with the progression of weather fronts over the sites.
- While HWSS scenarios are currently manageable, high penetration cases will be problematic. Research is required for future scenarios with higher penetrations with regards to system inertia and sudden loss of generation. The studies done thus far have been deterministic in nature.
- Further research is required to forecast HWSS more accurately. This will assist in reducing balancing costs in inter-connected networks, as well as to alleviate risk for interconnected and isolated networks.
- HWSS experiences vary across countries.
- Historical case study data shows a substantial number of events that resulted in the complete shutdown of the wind farm. Complete shutdown of the wind farm can occur within 6 minutes which if not correctly forecast will result in a large and unexpected imbalance.
- The mitigation methods proposed for HWSS events include the implementation of an HWRT controller and pre-emptive curtailment. Both have negative effects. The HWRT controller increases wear and tear, which reduces the life span of the turbine. Pre-emptive curtailment requires accurate forecasting models.
- A case study for the Danish system, which has a high penetration of wind energy, suggests that 1.5 GW is currently at risk of being lost within 30 minutes due to HWSS. This emphasizes the importance of forecasting of HWSS events.

It is clear from the available literature that HWSS has not been extensively investigated to date. Although forecasting and quantification of the impacts of HWSS feature strongly in the available literature, no models have thus far been formulated to describe this phenomenon, and no event-based

forecasting models have been developed. The need for further work in this field is generally acknowledged.

The research presented in this dissertation targets two major aspects of HWSS, namely the modelling, quantification, and comparison of the relative risk of HWSS events, and the short-term operational forecasting of HWSS events. It is evident from literature that the development of a dedicated HWSS forecasting model will assist in the management and mitigation of the short-term risk associated with HWSS events. The development of site-specific models with which to quantify and compare temporal risk will, furthermore, aid in the siting of wind farms in regions with a low susceptibility for HWSS events.

1.4 Research Objectives and Novel Contributions

1.4.1 Research Aims and Objectives

Two major aims are targeted to address the research questions highlighted in the literature review. These objectives are the modelling, quantification, and comparison of the relative risk of HWSS events, as well as the development of a short-term forecasting model for HWSS events. These aims give rise to the following specific objectives:

- Development of a suitable site-specific meso-scale wind speed forecasting model.
- Identification and/or development of a model for the downscaling of wind speed forecasts to micro-scale level.
- Development of an HWSS event model.
- The combination of models into a computationally-expedient processing chain for the short-term forecasting of HWSS events.
- Development of a technique for the quantification and comparison of the relative temporal risk between wind farm sites.

1.4.2 Novel Contributions

1.4.2.1 Overview

Research into the formulated objectives include some novel contributions, as described in the subsections that follow.

1.4.2.2 Development of a Multi-Model Ensemble Synthesis Methodology Using the Mean-Variance Portfolio Theory

It is proposed to apply Mean-Variance Portfolio Theory (MVPT) to the multi-model, multi-scheme, Numerical Weather Prediction (NWP) ensemble forecasts to achieve improved short-term forecasting

of site-specific wind speeds. This technique is shown to be computationally expedient, and yields improved results over averaging of the ensemble member forecasts.

1.4.3 Development of a Novel Statistical Downscaling Model

A computationally efficient, statistical downscaling model is proposed to predict wind turbine wind speeds using historical data and a meso-scale forecast using a Monte Carlo approach. This work incorporates various original contributions:

- Temporal and spatial partitioning of the dataset is undertaken to reduce biases and the effects of turbine wakes, surface roughness effects, atmospheric uncertainties etc.
- Features of the statistical spatial wind speed distributions are optimised for the tempro-spatial partitions for improved site characterisation.
- Random sampling, with an optimised seed, is employed to extract multiple archetypal wind speed profiles from the spatial wind speed distributions. Once the model is optimised, the sampled wind speeds are representative of the turbine wind speeds at the wind farm.
- A turbine ranking method is introduced for the bijective mapping of the sampled wind speeds to turbines.

1.4.4 Short-Term Forecasting of HWSS Events

Two novel approaches are demonstrated for the short-term forecasting of the number of turbines in HWSS mode at a utility-scale wind farm.

A hybrid NWP-Artificial Neural Network (ANN) model is implemented, which translates a meso-scale forecast to a number of turbines in HWSS mode. This method is shown to provide an accurate forecast for mid to large events at the expense of a large number of false alarms.

The proposed wind speed downscaling model is utilised in an alternative forecasting model topology. An ensemble of meso-scale wind speed forecasts is optimised for high wind speeds using an intermediary ANN model with custom loss functions. The synthesised meso-scale forecast is downscaled to micro-scale wind speeds at each turbine using a pre-trained statistical model. Event forecasts are subsequently derived using a proposed HWSS event model for comparison with measured events. The results show that this model yields improved forecasting results for high wind speeds, with fewer false alarms than the ANN model formulation.

1.4.5 Development of a Risk Quantification Model for HWSS Events for Site Characterisation and Comparison

Limited research has been reported to quantify the site-specific frequency, severity and relative risk of loss of generation events. A novel technique is proposed for site characterisation and comparison of

HWSS events. This has potential applications for site planning, as well as for the characterisation and comparison of risk for operational wind farms. The proposed technique utilises a probabilistic site-specific spatial wind speed distribution to determine turbine-level wind speeds. A rule-based methodology is applied to extract HWSS events from micro-scale wind speeds. The resulting binary event series is analysed using survival theory to create a time-to-event model for subsequent analysis and relative probabilistic comparison of risk between sites.

1.5 Layout of Dissertation Document

The remainder of this dissertation is structured as follows.

Chapter 2 describes the implementation and performance evaluation of a NWP-based ensemble forecasting model. This work forms the foundation of the event-based forecasting model.

Chapter 3 focusses on the development of a novel, site-specific, statistical wind speed downscaling technique. The model methodology and implementation are described, and a performance evaluation is performed.

Chapter 4 proposes two short-term wind speed event forecasting models, namely a hybrid NWP-ANN model, and the application of the novel statistical downscaling model described in Chapter 3.

Chapter 5 details the modelling, risk quantification, and characterisation of HWSS events at a wind farm site using survival analysis. This method is further extrapolated for a relative measure of risk between sites.

Chapter 6 presents the final conclusions and proposals for further research.

Chapter 2

Short-Term Wind Speed Forecasting using a Numerical Weather Prediction Model Ensemble

2.1 Overview

The main research objective addressed in this dissertation, i.e. the development of a modelling and short-term forecasting methodology for High Wind Speed Shutdown (HWSS) events, requires implementation of an effective, site-specific wind speed forecasting model. This chapter focusses on the development and implementation of a model for short-term forecasting of the wind speed at a given site, using an ensemble of meso-scale forecasts obtained using multiple Numerical Weather Prediction (NWP) models as a departure point. Two methodologies for translating the meso-scale forecasts to a single site-specific forecast are investigated, namely an Artificial Neural Network (ANN), and a novel approach using the Mean-Variance Portfolio Theorem (MVPT).

2.2 Forecasting Horizon and Scales of Motion

The forecasting time-scales reported in literature for the various classes of forecasts are indistinct. Soman *et al.* [16], for example, define very short-term, short-term and medium-term forecasting horizons as 0 to 30 minutes, 30 minutes to 6 hours, and 6 hours to 1 day ahead respectively, whereas Foley *et al.* [17] specify seconds to minutes, minutes to 2 days and 2 to 7 days for the same categories respectively. The practical application of the work presented in this study is aimed at informing scheduling and dispatch. A forecasting horizon of 24 hours is therefore adopted, which falls within the short-term time category.

The temporal resolutions required for power system studies such as scheduling, dispatch, unit commitment, generator cycling, and ramping studies necessitate that sub-hourly data be utilised [18]. The variability of renewable power generation profiles, similarly, requires data on a sub-hourly scale for accurate modelling [19]. The most common temporal resolution used for studies linked to wind energy system effects is the 10 minute sampling interval. As the focus of this work is on the forecasting of events to assist the System Operator with scheduling and dispatch, short-term dynamic fluctuations such as those introduced by gusts, etc., are not considered.

Meteorological studies analyse weather phenomena for defined scales of motion. These scales are typically denoted as macro-scale (global and synoptic scales), meso-scale, and micro-scale. Table 3 summarises the definitions of scales of motion on a temporal/spatial scale as proposed by Orlanski [20]. The definitions suggest that the temporal scale for the targeted forecasting application requires consideration of both meso and micro-scale. The macro-scale model, which typically implements global circulation models such as the Global Forecasting System (GFS), delivers the input and boundary

conditions to the meso-scale NWP model. Meso-scale phenomena typically include the formation of localised thunderstorms, low-level jets, squall lines, Meso-scale Convective Complexes (MCCs) etc.

Table 3. Scales of Motion Defined by Orlanski [20].

Scales	> 1 month	1 month 1 day	1 day 1 hour	1 hour 1 minute	1 minute 1 second	
Larger 10000 km	Standing waves, Ultra-long waves, Tidal waves					**Macro**
10000 km 2000 km		Baroclinic waves				**Macro**
2000 km 200 km		Fronts, Hurricanes				**Meso**
200 km 20 km			Nocturnal low level jet, Squall lines, MCCs, Cloud clusters			**Meso**
20 km 2 km			Thunderstorms, Urban effects			**Meso**
2 km 200 m				Tornadoes, Deep convection		**Micro**
200 m 20 m				Dust devils, Thermals, Wakes		**Micro**
20 m Smaller					Turbulence	**Micro**

2.3 Modelling Approaches

2.3.1 Overview

The forecasting models typically employed in wind energy applications may be classified into three broad categories, namely physical, statistical, and hybrid models [21]. The micro-scale wind speed forecasting approach adopted in this investigation represents a hybrid model in the sense that it combines elements of the physical and statistical modelling approaches.

2.3.2 Physical Models

Physical methods comprise techniques that utilise detailed physical descriptions of the site characteristics and meteorological information to predict the future atmospheric state [22]. This is accomplished using NWP models that solve the governing equations of atmospheric flow, including the conservation of mass, momentum, energy, and the ideal gas law. Given input and boundary conditions, these equations allow for the resolution of the atmospheric state in a defined study space. It is therefore possible, given the initial state of the atmosphere near a wind farm, to derive the wind speeds in and around the wind farm at multiple heights by solving for the atmospheric flow. Physical models generally offer superior performance beyond 3 to 6 hour forecasting horizons [23]. Consequently, the majority of short-term forecasting systems employed by utilities incorporate NWP models, coupled with post-processing corrections [24].

The most popular NWP model, the Weather Research and Forecasting (WRF) model, is a non-hydrostatic meso-scale model which was developed for atmospheric research as well as for forecasting

applications [25]. The WRF model downscales global forecasts, such as the GFS, or the European Centre for Medium-Range Weather Forecasts (ECMWF), temporally and spatially. This is accomplished through the numerical approximation of the non-linear partial differential equations representing atmospheric flow, and parameterisations for sub-grid scale processes which are spatially and temporally too confined, or too complex, to represent in the NWP model [26].

The accuracy of deterministic NWP forecasts is dependent on the local climatology and terrain complexity. Improvement of the forecasting accuracy in complex terrain is achievable by downscaling the meso-scale outputs. Bilal *et al.* [27], for example, demonstrated improved wind speed and wind direction predictions by coupling a NWP model with WindSim, a Computational Fluid Dynamics (CFD) solver.

Forecasting requires a probabilistic rather than a deterministic approach for the quantification of uncertainty. One of the most recognized approaches in probabilistic forecasting is ensemble forecasting. It is well documented that the combination of multiple models results in an improvement in any singular forecast [28]. Ensembles are typically generated by perturbing initial and/or boundary conditions, or through multi-model simulations to encapsulate various potential outcomes. Recent advancements in high-performance computing, coupled with more efficient NWP models, has rendered ensemble simulations an attractive option for forecasting applications.

2.3.3 Statistical Models

Statistical methods employ historical information to predict future values by training models to recognise patterns and functional dependencies. Further sub-classification may be made to differentiate between time series regression approaches and Artificial Intelligence (AI) techniques [16]. Popular time series regression techniques include the Auto Regressive (AR), Moving Average (MA), Auto-Regressive Moving Average (ARMA), and Auto Regressive Integrated Moving Average (ARIMA) [17]. Other techniques include linear predictors, exponential smoothing, and gray predictors [16]. The most common AI techniques include ANNs, fuzzy logic systems, and Support Vector Machines (SVM) [17]. These techniques are adept at establishing the complex, non-linear relationships between explanatory variables and the predictand.

2.3.4 Hybrid Models

Hybrid models exploit the strengths of multiple approaches to obtain a reduced forecasting error. This may be accomplished using various combinations of physical and/or statistical models [29].

2.4 Numerical Weather Prediction Model

Due to advancements in computing power, increased observational data, and improvements in the models, NWP models have become a viable option for weather forecasting. The non-linearity and

physics parameterisations of the governing model equations, however, create inherent uncertainty in the forecasts. A perfect representation of the initial state of the atmosphere cannot be accurately known and encapsulated in the model. To address these shortcomings, ensemble forecasting is utilised to create a probabilistic spread of possible atmospheric states [30]. The ensemble forecasts are then used as an indication of forecasting confidence, and to improve the deterministic forecasting accuracy.

2.5 Weather Research and Forecasting Model

2.5.1 Overview

WRF is a community-supported NWP model developed for atmospheric research, as well as for forecasting applications. This advanced meso-scale model serves a wide array of meteorological applications over a broad spatial range from tens of meters to thousands of kilometres [31]. Figure 3 shows a simplified flow chart describing the system architecture. Two input datasets are required to initialise the WRF Pre-processing System (WPS), namely a static geographical dataset and a meteorological forecast. The pre-processor defines a 3-dimensional, gridded representation of the simulation domain, and interpolates the input datasets onto the horizontally spaced grid points defined in the simulation setup. Until recently, WRF only supported isotropic spherical projections. Accordingly, the majority of the grid projections require constant grid lengths, and that the longitudinal to latitudinal grid length ratio, $\Delta x / \Delta y$, be constant over the entire domain. The resulting conflicting projections require a rotation of the horizontal, earth-relative wind components in the meteorological data to components parallel to the defined simulation grid [32].

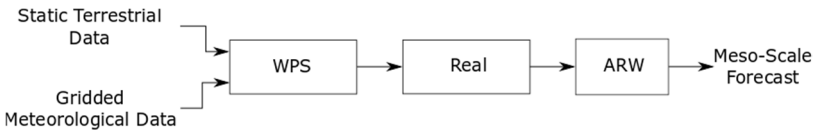

Figure 3. Simplified flow diagram describing the WRF version 3 modelling system [31].

Figure 4 displays an example of contrasting grid projections, along with the horizontal Arakawa-C staggered grid architecture, and the vertical grid depiction [32]. The wind velocity components, U, V, and W, are defined normal to the surface of the grid interfaces as they drive the boundary conditions. The thermodynamic variables, denoted by θ, are defined at the cell centre. This is because these quantities are representative of the mean values within the cell.

Once the model is initialised, WRF performs a numerical integration of the fully compressible non-hydrostatic Euler equations (conservation of mass, momentum and energy) with a mass-based terrain-following vertical coordinate system, η. The vertical coordinate, η, is defined as [32]

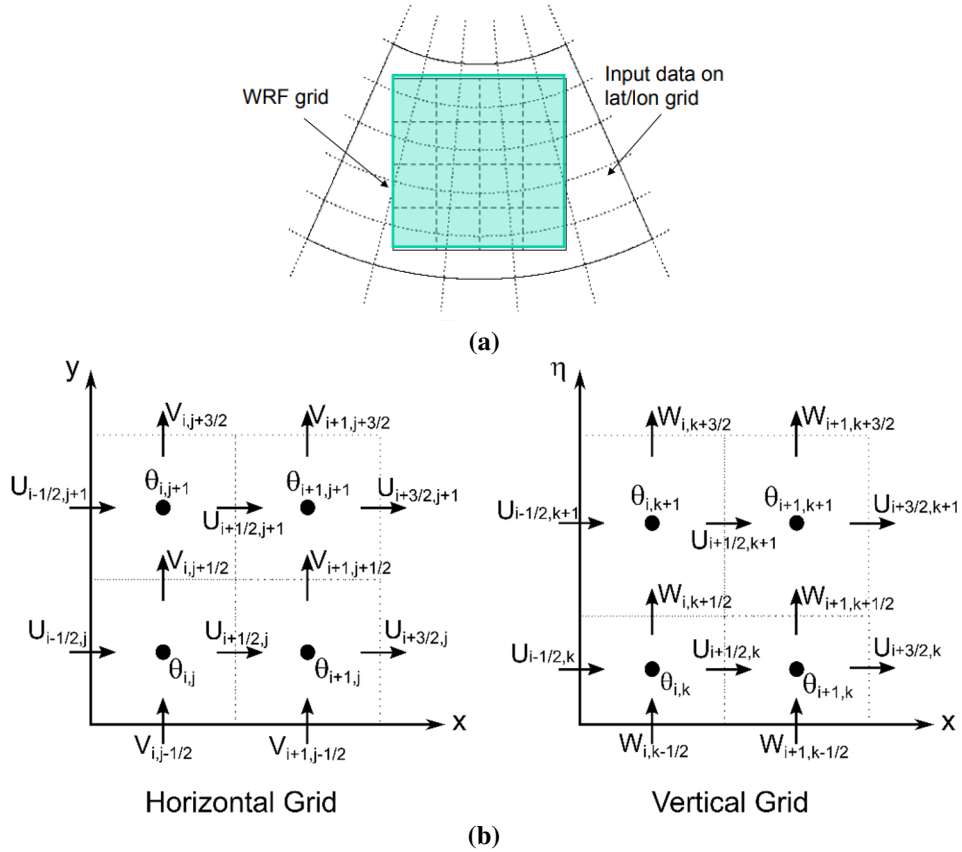

Figure 4. (a) Example of the WRF grid projection superimposed on a latitude/longitude grid, and the (b) grid discretisation architecture [32].

$$\eta = \frac{\pi_h - \pi_t}{\pi_s - \pi_t}, \tag{2.1}$$

where π_h, π_t, and π_s, denote the hydrostatic pressure, the pressure at the top boundary, and the pressure at the surface respectively. Figure 5 shows an example of the terrain-following vertical coordinate variation from a value of 1 at the surface, to zero at the upper model boundary [32].

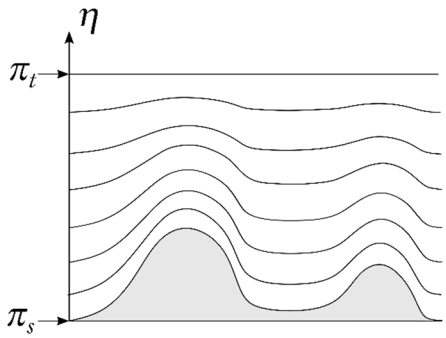

Figure 5. The mass vertical coordinate system employed by WRF version 3 [32].

The dynamical solver of WRF performs a tempro-spatial integration of the Euler equations forward in time. The equations are discretised on the 3D state space, and an approximate numerical solution is determined. The WRF solver utilises the Runge-Kutta 2nd order and 3rd order time integration scheme options, as well as 5th order advection options in the horizontal direction, and 3rd order advection in the vertical direction [32].

2.5.2 Parameterisations

Supplementary to the solution of the Euler equations, WRF utilises parameterisations to express the interaction of meteorological processes which are spatially and temporally too confined, or too complex to model. These parameterisations are fundamental to the WRF model as each model relies on different assumptions for distinct meteorological processes, which in turn renders different strengths and weaknesses for the various model formulations. The following physics parameterisation options may be adjusted in WRF [32]:

- Radiation transfer processes (long and short-wave);
- Diffusion;
- Cumulus schemes;
- Land-surface model;
- Planetary Boundary Layer (PBL);
- Microphysics.

2.5.3 Ensemble Forecasts

Ensembles are generated by manipulating the physics parameterisations inherent in the WRF model's architecture. Uncertainty estimation is a by-product of ensemble generation, as the different models provide a spread of probable atmospheric states at the same instance in time. Recent advances in computing power, coupled with the improvements gained in more streamlined NWP models, has resulted in an increased interest in short-term ensemble forecasting for operational use. The combination of these models into an optimal deterministic forecast has been explored using techniques such as fuzzy systems [33], Bayesian model averaging [34], and random forests [35].

It is commonplace in ensemble forecasting to utilise an ensemble average to produce a deterministic forecast. Surcel *et al.* [36] demonstrated that this method oftentimes returned an improved forecast skill when compared with any singular ensemble member forecast. The ensemble average, $\hat{y}_{ens\_ave}$, is defined as follows:

$$\hat{y}_{ens\_ave}(i) = \frac{1}{M}\sum_{m=1}^{M} v^{f}{}_{m}(i), \tag{2.2}$$

where M denotes the number of ensemble members in the set, and $v^{f}{}_{m}$ denotes the m^{th} member in the ensemble member set. For comparative purposes, the methodologies proposed in this investigation are compared to the average defined in (2.2) by using the skill score, SS, which is defined as [37]

$$SS = 100 * \frac{\gamma^{ref} - \gamma}{\gamma^{ref}}, \tag{2.3}$$

where γ^{ref} denotes the reference forecast with which the forecast under evaluation, γ, is compared.

2.6 The Mean-Variance Portfolio Theorem

The MVPT represents a mathematical framework to devise an optimal portfolio of assets for a maximised return with a given level of risk [38]. The MPVT leverages the diversity of uncorrelated assets to construct an optimal portfolio arrangement. Figure 6 shows the volatility, or risk, and expected return of a portfolio as a function of the risk-return relationship for negative, uncorrelated, and positive correlation between two assets A, and B. The relationship locus is determined by the correlation between assets.

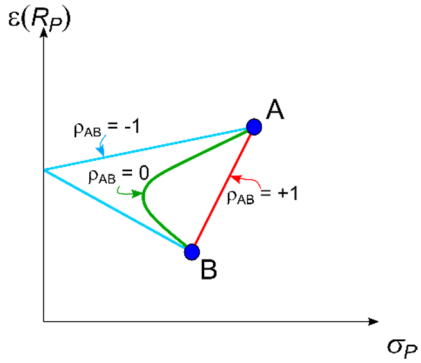

Figure 6. Risk and expected return of a portfolio as a function of the risk-return relationship for negative, uncorrelated and positive correlation between two assets A, and B [39].

From Figure 6, the relative risk, σ, and expected return, ε(R), of the two assets are related as follows:

$$\sigma_A > \sigma_B, \tag{2.4}$$

$$\varepsilon(R_A) > \varepsilon(R_B). \tag{2.5}$$

where σ_A, σ_B, $\varepsilon(R_A)$, and $\varepsilon(R_B)$ denote the standard deviation, or risk, of assets A and B, and the expected return of assets A and B respectively. The portfolio risk, σ_P, is determined from the statistical properties of the individual assets as follows [38]:

$$\sigma_P = \sqrt{w_A{}^2\sigma_A{}^2 + w_B{}^2\sigma_B{}^2 + 2w_A w_B \mathrm{cov}_{A,B}}, \tag{2.6}$$

with

$$\mathrm{cov}_{A,B} = \sigma_A \sigma_A \rho_{A,B}, \tag{2.7}$$

where $\mathrm{cov}_{A,B}$ represents the covariance between assets A and B, $\rho_{A,B}$ denotes the correlation between assets A and B, and w_A and w_B are the proportion of assets A and B in the portfolio respectively. For a perfect positive correlation, ie. $\rho_{AB} = +1$, the portfolio risk reduces to the weighted sum of risk of each asset in the portfolio. This locus is represented by the straight, red line segment between asset A and B. For assets with no linear relation, i.e. $\rho_{AB} = 0$, the risk-return locus is designated by the curved green line adjoining the assets. For a perfect negative correlation, the portfolio risk reduces to the triangular blue line segment. For a scenario where the two assets are uncorrelated, the portfolio risk is defined as

$$\sigma_P = \sqrt{w_A{}^2\sigma_A{}^2 + w_B{}^2\sigma_B{}^2} < w_A\sigma_A + w_B\sigma_B. \tag{2.8}$$

This shows that introducing assets which are uncorrelated, or negatively correlated, will lower the portfolio risk beyond what is achievable with correlated assets.

Figure 7 shows the expected return versus the risk for a portfolio with greater than two assets. The mean-variance boundary is the locus which contains the set of all feasible assets. A portfolio cannot be constructed to return a risk-return point outside this boundary. For a given level of risk, any point on the efficient frontier yields a larger expected return than any point inside the feasible set.

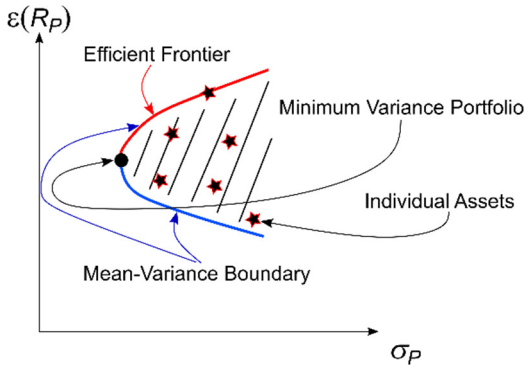

Figure 7. Risk versus expected return for a portfolio with greater than two assets [39].

Figure 8 displays the effect of diversification with an increasing number of assets in the portfolio [40]. It is evident from the figure that portfolio risk is reduced through increased portfolio diversification [39]. Non-diversifiable risk is the risk inherent in the market which is unpredictable and cannot be avoided.

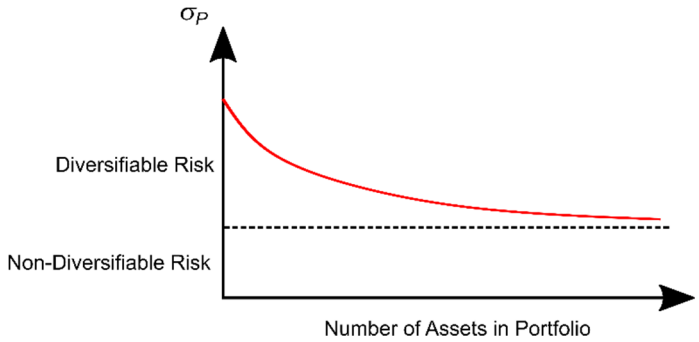

Figure 8. Portfolio risk versus number of assets in the portfolio [40].

To design a portfolio from multiple assets, a relation between the performance of the constituent assets and the portfolio's expected mean and variance must be determined. The expected portfolio return, $\varepsilon(R_P)$, is determined from the proportionate weighting of the individual assets' expected returns. The portfolio variance is determined from a simplification of (2.6) as follows [38]:

$$\sigma_P^2 = \sum_{k=1}^{N} \sum_{j=1}^{N} w_j w_k cov_{j,k}, \tag{2.9}$$

where N denotes the number of assets in the portfolio.

2.7 Performance Evaluation Metrics

Common error metrics are used to evaluate the efficacy of the various forecasts in this investigation, i.e. the individual ensemble forecasts, as well as the forecasts obtained from application of the ANN and MVPT combination models. The measured wind profile data obtained from a meteorological mast is selected as the point of reference.

The forecast error, e_i, is defined by the relationship

$$e_i = v_i^m - v_i^f, \tag{2.10}$$

where v_i^m denotes the measured wind speed, and v_i^f denotes the wind speed forecast for the i^{th} sampling interval. The forecast error is interpreted using the following standard metrics: Mean Absolute Error (MAE); Root Mean Squared Error (RMSE); Mean Absolute Percentage Error (MAPE); Bias; and coefficient of determination (R^2). These metrics are defined as follows [41] - [43]:

$$\text{MAE} = \frac{1}{n}\sum_{i=1}^{n}|e_i|, \tag{2.11}$$

$$\text{RMSE} = \sqrt{\frac{1}{n}\sum_{i=1}^{n}(e_i)^2}, \tag{2.12}$$

$$\text{Bias} = \frac{1}{n}\sum_{i=1}^{n} e_i, \tag{2.13}$$

and

$$R^2 = 1 - \left(\frac{\sum_{i=1}^{n} {e_i}^2}{\sum_{i=1}^{n}(v_i^m - \overline{v^m})^2}\right), \tag{2.14}$$

where n denotes the number of sampling intervals, and $\overline{v^m}$ denotes the mean of the set of measured wind speeds for all n samples. A good forecast has the following properties: the return of high accuracy (small MAE), a small number of large forecast errors (small RMSE), no bias, and a correlation coefficient close to 1 (good trending) [44].

2.8 Implementation and Performance Evaluation of the WRF Ensemble Models

2.8.1 Overview

The implementation and performance evaluation of a multi-model WRF ensemble approach is described in the following section. A nine-member ensemble is generated using three model runs, each of which generates forecasts for three domains, with variations in the physics parameterisation options.

2.8.2 Implementation of the WRF Ensemble Model

Figure 9 shows a flow diagram of a multi-model WRF ensemble with different physics parameterisation options. Each of the three implemented models is ascribed a model reference, namely MYJ1, MYJ2, and ACM2. The selected physics options for each of the WRF models is described in detail later in this

section. Three nested grid domains denoted domain 1 (D1), domain 2 (D2) and domain 3 (D3), are utilised for each model. The macro-scale GFS forecast data and static terrestrial data are used as inputs into each of the separate WRF model simulations, which in turn generates a forecast for each of its domains. A nine-member ensemble of wind speed forecasts is produced by the collection of models.

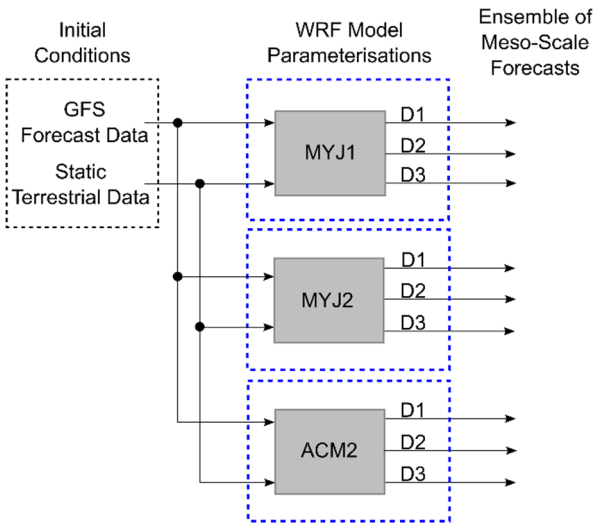

Figure 9. WRF ensemble generation using three physics parameterisation sets, each with three nested grid domains.

The GFS forecasting model is maintained by the National Centres for Environmental Prediction (NCEP). Forecasts are provided four times daily, at 00H00, 06H00, 12H00 and 18H00 UTC in a 3 hourly time step to a forecast horizon of 192 hours for the 0.5° domain [45]. The GFS forecasts are used as the initial and boundary condition inputs for the WRF model. Cold-start forecasts for a 24 hour forecast horizon are initialised at 00H00 daily for each domain from 01 January 2017 until 31 July 2017 with a 10 minute sampling interval. Observational and grid nudging are not utilised due to the short integration period which renders model drift insignificant.

Three one-way nested domains are considered, each of which is centred on the wind farm under test, with grid lengths of 27 km, 9 km, and 3 km for D1, D2, and D3 respectively. All domains are created with 100 x 100 horizontal grid points.

Forty one vertical levels are specified, with the uppermost level atmospheric pressure of 50 hPa. To improve the boundary layer representation, the lower four vertical levels are situated within 100 m above ground level, i.e. at 15 m, 40 m, 70 m and 100 m approximately. These selections are based on the meso-scale modelling for the Wind Atlas of South Africa (WASA) project [46].

Siuta *et al.* [44] demonstrated that the wind speed forecasting accuracy at a typical hub height of wind turbines is most sensitive to the specification of the PBL parameterisation and the selected grid length. Turbines, owing to their height, are situated within the PBL for the majority of the day. The PBL scheme is of importance as it controls the interaction of surface-layer wind speeds, as well as the exchange of

heat, momentum, and moisture between the modelled levels [32]. The PBL scheme is, consequently, varied for two of three WRF models, whilst the other physics parameterisations are altered for the third model. A set of diverse physics representations is thereby created for the targeted site.

The Rapid Radiative Transfer Model (RRTM) and the Community Atmospheric Model (CAM) are utilised as the long-wave radiation parameterisations, while the Duhia and CAM models are selected for the short-wave radiation representation. The Pleim-Xiu and Monin-Obukhov surface-layer physics options are selected. The CAM V5.1.2-moment 5-class and WRF Single Moment (WSM) 5-class microphysics parameterisation options are utilised. The Kain-Fritsch cumulus scheme is selected for domain 1 and 2 for all models. The Mellor-Yamada-Janjic (MYJ) and Asymmetric Convective Model version 2 (ACM2) models are selected for the PBL parameterisations as they represent two of the most popular parameterisation schemes from different turbulent mixing solution approaches. These models should, therefore, yield contrasting results as found by Siuta *et al.* [44].

Table 4 summarises the physics parameterisations and grid domains selected for the nine ensemble members, where MYJ1, MYJ2, and ACM2 represent the model reference for the three sets of physics parameterisation options selected for the generation of the WRF model ensemble set.

Table 4. Parameterisation options used in the WRF multi-model ensemble for the targeted site.

Ensemble Member	Model Reference	PBL Scheme	Domain	Microphysics	Surface Layer	Long-Wave Radiation	Short-Wave Radiation	Cumulus Scheme
1	MYJ1	MYJ	1	WSM Single-moment 5-class	Monin-Obukhov	RRTM	Duhia	Kain-Fritsch
2			2	WSM Single-moment 5-class	Monin-Obukhov	RRTM	Duhia	Kain-Fritsch
3			3	WSM Single-moment 5-class	Monin-Obukhov	RRTM	Duhia	None
4	MYJ2	MYJ	1	CAM V5.1 2-moment 5-class	Monin-Obukhov	CAM	CAM	Kain-Fritsch
5			2	CAM V5.1 2-moment 5-class	Monin-Obukhov	CAM	CAM	Kain-Fritsch
6			3	CAM V5.1 2-moment 5-class	Monin-Obukhov	CAM	CAM	None
7	ACM2	ACM2	1	WSM Single-moment 5-class	Pleim-Xiu	RRTM	Duhia	Kain-Fritsch
8			2	WSM Single-moment 5-class	Pleim-Xiu	RRTM	Duhia	Kain-Fritsch
9			3	WSM Single-moment 5-class	Pleim-Xiu	RRTM	Duhia	None

2.8.3 Performance Evaluation of the WRF Ensemble Model

2.8.3.1 Overview

The accuracy of the wind speed and wind direction forecasts obtained for the individual ensemble members is assessed in terms of the error metrics defined in section 2.7. This performance evaluation exercise is conducted with the view to confirm that the WRF models perform adequately for the site, and to ascertain a baseline metric with which to compare the results from the ensemble combination

models. The proposed forecasting methodology is implemented for a utility-size wind farm containing 2 MW turbines with a hub height in excess of 100 m, as well as an on-site meteorological mast. The wind farm is located in simple to semi-complex terrain. As such, NWP models are capable of creating a usable forecast. The available dataset includes 10 minute averaged values for nacelle wind speeds, wind direction, temperature and pressure readings for all turbines, wind speed and direction from a meteorological mast, and aggregated power exported to the grid. The wind speed and wind direction data from the meteorological mast are used as a reference for comparison with the nearest forecast grid point, i.e. no interpolation is performed. Missing or corrupt data is removed from all datasets as part of the data sanitising procedure.

2.8.3.2 Analysing Individual Ensemble Member Forecasts

In order to compare WRF wind speed forecasts to the measurements from the meteorological mast, the WRF relative wind components must first be rotated from the utilised map projection to the earth-relative, cardinal coordinate system. The wind speed components generated by the WRF models, u and v are combined into a vector component, $v^f \angle \delta°$, as follows [47]:

$$v^f = \sqrt{{u_{earth}}^2 + {v_{earth}}^2}, \tag{2.15}$$

where

$$u_{earth} = u \cdot \cos\alpha - v \cdot \sin\alpha, \tag{2.16}$$

$$v_{earth} = v \cdot \cos\alpha + u \cdot \sin\alpha, \tag{2.17}$$

and α denotes the rotation of the WRF grid projection relative to the cardinal coordinate system. Given the relative horizontal wind speed components, u_{earth} and v_{earth}, the wind direction is obtained by [48]

$$\delta = A - \tan^{-1}\left(\frac{v_{earth}}{u_{earth}}\right) \cdot \frac{180}{\pi}, \tag{2.18}$$

where A denotes the angle to rotate the inverse tangent from its quadrant to a reference direction corresponding to true north.

Table 5, Table 6 and Table 7 summarises the monthly MAE, RMSE and R^2 metrics respectively for the wind speed forecasts for the multi-model WRF ensemble with reference to the on-site meteorological mast over the defined study period. The results show that all ensemble members perform well, with a total MAE = 1.625 ms^{-1}. The best performing scheme has an average MAE = 1.562 ms^{-1}. As expected, the forecasting skill varies from month to month. The best forecast is obtained for May, with an average MAE = 1.489 ms^{-1}. The forecast with the lowest accuracy is obtained for April, with an average MAE = 1.941 ms^{-1}. Similarly, the RMSE results show substantial variation amongst ensemble members. The coefficient of determination shows good performance for a raw, uncorrected forecast. The most notable change in R^2 values is prevalent from June to July, where the performance degrades by a factor of approximately two, despite the better than average MAE in July. This demonstrates the need to evaluate

forecasts with a combination of the above metrics.

Table 5. MAE (ms^{-1}) for the WRF multi-model ensemble with reference to the on-site meteorological mast.

Month	MYJ1 D1	MYJ1 D2	MYJ1 D3	MYJ2 D1	MYJ2 D2	MYJ2 D3	ACM2 D1	ACM2 D2	ACM2 D3	Average
January	1.657	1.531	1.537	1.760	1.670	1.517	1.651	1.667	1.605	1.622
February	1.747	1.595	1.661	1.696	1.577	1.591	1.666	1.743	1.656	1.659
March	1.449	1.402	1.413	1.571	1.566	1.474	1.335	1.483	1.381	1.453
April	1.987	2.033	1.734	2.093	2.129	1.795	1.920	1.975	1.807	1.941
May	1.444	1.420	1.474	1.509	1.443	1.485	1.573	1.550	1.507	1.489
June	1.669	1.565	1.606	1.685	1.615	1.593	1.664	1.590	1.551	1.615
July	1.730	1.601	1.615	1.709	1.559	1.478	1.594	1.543	1.507	1.593
Average	**1.669**	**1.592**	**1.577**	**1.718**	**1.651**	**1.562**	**1.629**	**1.651**	**1.574**	**1.625**

Table 6. RMSE (ms^{-1}) for the WRF multi-model ensemble with reference to the on-site meteorological mast.

Month	MYJ1 D1	MYJ1 D2	MYJ1 D3	MYJ2 D1	MYJ2 D2	MYJ2 D3	ACM2 D1	ACM2 D2	ACM2 D3	Average
January	2.096	1.970	1.986	2.219	2.104	1.978	2.090	2.135	2.054	2.070
February	1.974	1.720	1.791	1.802	1.592	1.629	1.850	1.851	1.780	1.777
March	1.778	1.698	1.747	1.940	1.891	1.814	1.640	1.819	1.694	1.780
April	2.384	2.531	2.154	2.544	2.697	2.254	2.306	2.516	2.232	2.402
May	1.781	1.764	1.896	1.843	1.798	1.918	1.899	1.879	1.845	1.847
June	2.050	1.948	1.994	2.065	2.003	1.971	2.040	1.959	1.912	1.994
July	1.970	1.846	1.897	2.049	1.881	1.861	1.799	1.748	1.743	1.866
Average	**2.005**	**1.925**	**1.924**	**2.066**	**1.995**	**1.918**	**1.947**	**1.987**	**1.894**	**1.962**

Table 7. Coefficient of determination (R^2) for the WRF multi-model ensemble with reference to the on-site meteorological mast.

Month	MYJ1 D1	MYJ1 D2	MYJ1 D3	MYJ2 D1	MYJ2 D2	MYJ2 D3	ACM2 D1	ACM2 D2	ACM2 D3	Average
January	0.656	0.687	0.672	0.620	0.652	0.674	0.662	0.672	0.671	0.663
February	0.647	0.641	0.642	0.660	0.645	0.665	0.649	0.627	0.644	0.647
March	0.673	0.674	0.654	0.654	0.655	0.656	0.727	0.705	0.710	0.679
April	0.559	0.534	0.610	0.533	0.519	0.592	0.576	0.543	0.590	0.562
May	0.740	0.751	0.673	0.736	0.762	0.682	0.709	0.723	0.691	0.719
June	0.717	0.739	0.720	0.707	0.718	0.723	0.717	0.742	0.749	0.726
July	0.378	0.408	0.351	0.415	0.469	0.491	0.411	0.431	0.404	0.418
Average	**0.624**	**0.634**	**0.618**	**0.618**	**0.632**	**0.640**	**0.636**	**0.635**	**0.637**	**0.630**

The bias for each ensemble member is determined using (2.13) for each hourly average of the 24 hour forecasting horizon. Figure 10 to Figure 12 shows boxplots used to visualise the spread of biases for the forecasting horizon in hourly intervals for each ensemble member. The dominant positive bias indicates a propensity to under-predict the wind speeds in the afternoon for D2 of all schemes and all domains for the ACM2 model. The models using the MYJ PBL scheme show similar biases, which indicates that the PBL selection plays the largest role in model sensitivity, as reported in literature. As the ACM2 model has the largest bias, it has the greatest potential for improvement in wind speed forecasting skill through post-processing rectification.

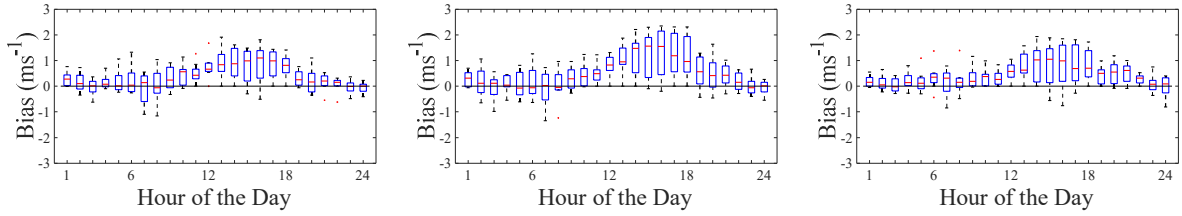

Figure 10. Bias versus forecast horizon: (a) ACM2 D1 (b) D2 and (c) D3.

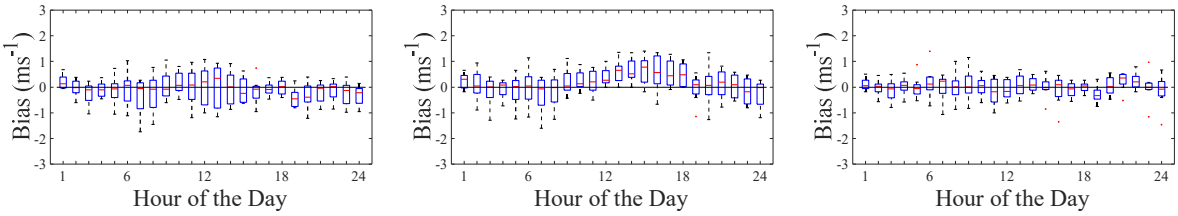

Figure 11. Bias versus forecast horizon: (a) MYJ1 D1 (b) D2 and (c) D3.

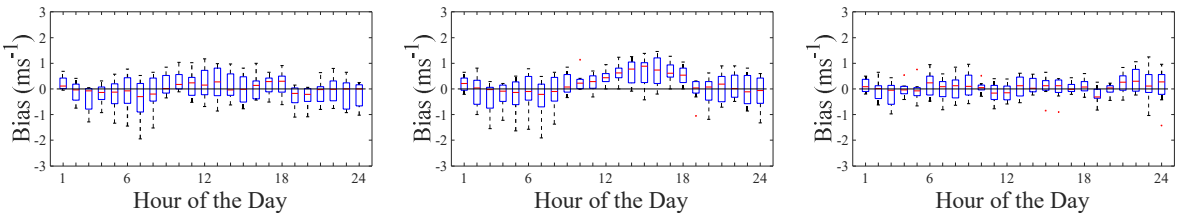

Figure 12. Bias versus forecast horizon: (a) MYJ2 D1, (b) D2 and (c) D3.

2.8.3.3 Accuracy of the Wind Direction Forecasts

Accurate forecasting of wind direction is fundamental to effective forecasting at the wind turbine level. Changes in wind direction exposes the turbines to different micro-spatial wind speeds through terrain differences, surface roughness changes, wind farm layout changes, variations in the wake effect, etc. [49], [50].

Figure 13 shows the wind direction probability density of D3 for each model formulation, as well as for the measured wind direction from the meteorological mast. The predominant wind direction at the site is south-south westerly. The results show close overall agreement between the modelled and measured wind direction.

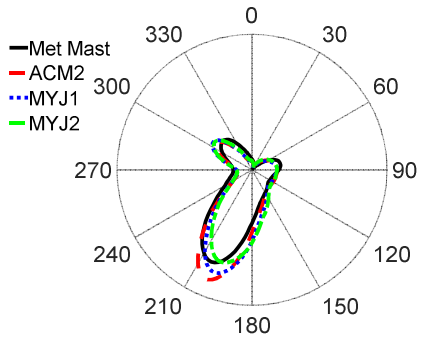

Figure 13. Wind direction probability density of measured and WRF simulations for D3 of the three PBL schemes.

2.8.3.4 Analysing the Ensemble Wind Speed Forecasts Collectively

Two figures of merit are used in the assessment of the variation of the multi-model ensemble wind speed forecasts. These are defined as follows:

$$\mathrm{IQR} = \mathrm{Q}_3 - \mathrm{Q}_1, \tag{2.19}$$

$$\text{Range} = \text{Max}(X) - \text{Min}(X), \tag{2.20}$$

where Q_1 and Q_3 denote the lower and upper quartiles, and X denotes the set of ensemble member wind speed forecasts. Figure 14 shows the range and IQR of the multi-model ensemble wind speed forecasts. The results show that the ensemble model variation is significant. The mean and maximum of the range is approximately 2.1 ms^{-1} and 6 ms^{-1} respectively.

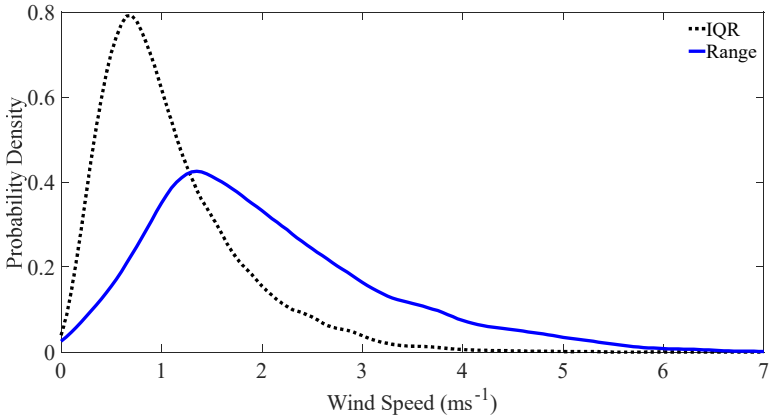

Figure 14. Range and IQR of the multi-model ensemble wind speed forecasts.

Figure 15 shows a graphical representation of the ensemble forecasts compared to measured wind speed for four typical days in the dataset. The IQR is represented by the blue portion of the box plot for each sampling interval and denotes the 50 % confidence around the mean. It is shown that the uncertainty varies over the forecast horizon. The displayed figures demonstrate that a small uncertainty does not indicate that the forecast will be accurate as there are times when the measured wind speed lies outside the range of the ensemble forecast despite the small uncertainty.

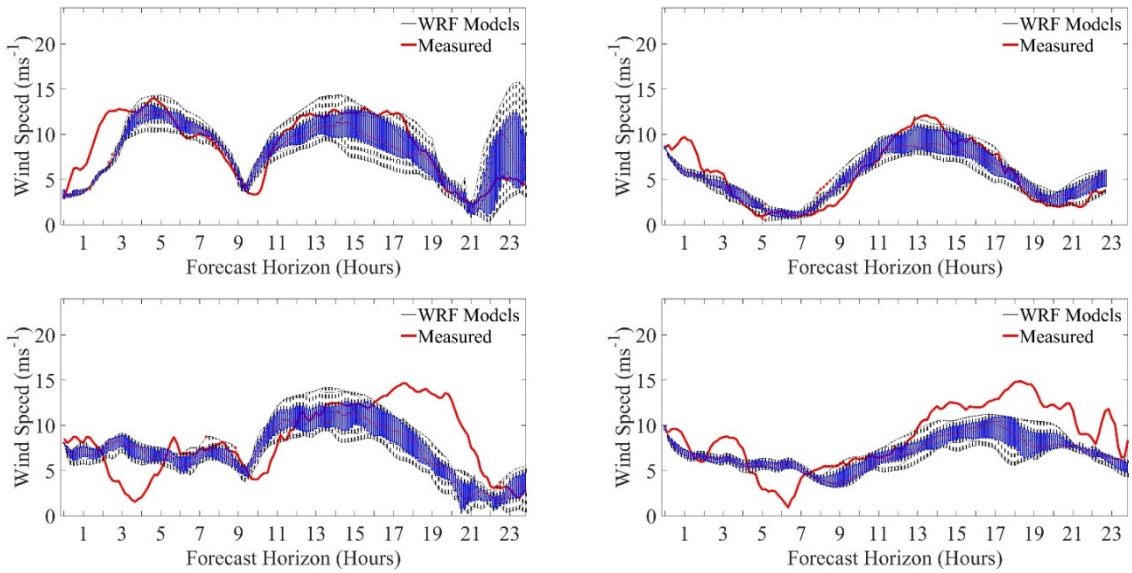

Figure 15. Ensemble forecasts compared to measured wind speed for four typical days in the dataset.

Figure 16 shows the MAEs of the wind speed forecasts with all members of the multi-model WRF

ensemble as a function of the mean wind speed at the wind farm. The results indicate that the MAE increases with increasing wind speeds. This has implications for the forecasting of events that occur at higher wind speeds, such as the HWSS events targeted in this investigation. It is evident that a methodology is required to lower the MAE in the high wind speed range to improve the forecast accuracy for this application.

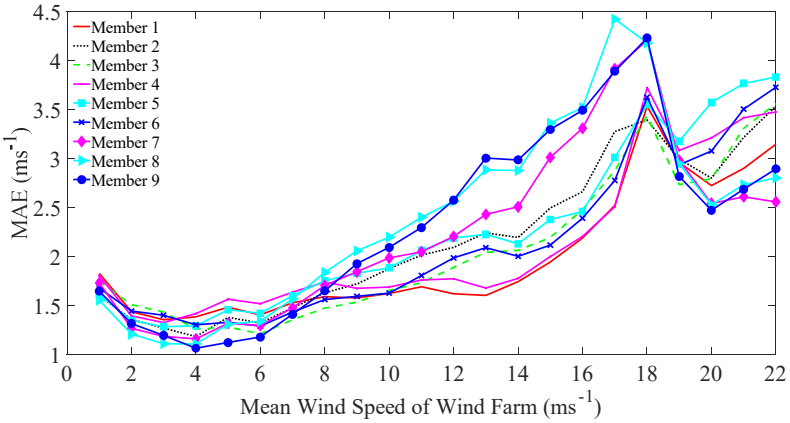

Figure 16. MAE for all WRF ensemble members versus the mean wind farm wind speed.

2.9 Combination of Ensemble Model Forecasts

2.9.1 Overview

This investigation explores two models, namely an ANN model and an MPVT model, for the translation of multiple forecasts from a WRF ensemble into a deterministic meso-scale forecast.

Cali *et al.* [51] demonstrated the use of ANN models, using multi-model and multi-scheme NWP forecasts as an input, for the forecasting of wind farm power. The results show significant improvement over a single NWP forecast. The ANN model, therefore, serves as a comparative technique with which to assess the performance of the MVPT model for the synthesis of the WRF model ensemble into a more accurate wind speed forecast.

The proposed MPVT model represents a novel approach. It is considered in view of the parallels between the temporal behaviour of portfolio assets such as stocks, bonds, currencies etc., and that of renewable power fluctuations from wind and solar energy. The MVPT has been applied for siting optimisation to reduce aggregated variability, as well as for wind farm repowering studies [52] - [56].

2.9.2 Implementation of the Mean-Variance Portfolio Model

Portfolio optimisation entails the selection of a weighted asset distribution out of a set of available assets to achieve a specified objective [38]. In the financial stock market, this objective may be to minimise risk, a proxy for variance, for a specified return, or to maximise return for a specified risk level. This is analogous to ensemble selection in that the optimal weighting of ensemble member forecasts may be

trained, which when compared the measured wind speed, V^{m}, returns an error, V^{error}, with a mean of zero and a minimised standard deviation. This is mathematically formulated as

$$V^{error} = V^{m} - V^{MVPT}, \tag{2.21}$$

with

$$V^{MVPT} = V^{f} \cdot W, \tag{2.22}$$

$$W = [w_1\ w_2\ w_3\ \cdots\ w_M]^{T}, \tag{2.23}$$

$$V^{f} = [V^{f_1}\ V^{f_2}\ V^{f_3}\ \cdots\ V^{f_M}], \tag{2.24}$$

where V^{MVPT} denotes the optimised wind speed forecast using the MVPT, W denotes the set of weightings of the individual ensemble member forecasts, V^{f} denotes the set of wind speed forecasts containing all ensemble members, and M denotes the number of forecasts in the ensemble. To determine the optimal portfolio of ensemble wind speeds, (2.9) is utilised in order to minimise the error variance as follows [38], [57]:

$$\min_{W} \text{var}(V^{error}) = \sum_{k=1}^{M} \sum_{j=1}^{M} w_j\, w_k \text{cov}_{j,k}. \tag{2.25}$$

The optimal weights for all considered ensemble members are returned for the minimum variance. The following optimisation constraints are imposed:

$$\sum_{k=1}^{M} w_k \mu_k = \mu_{v^m}, \tag{2.26}$$

and

$$\sum_{k=1}^{M} w_k = 1. \tag{2.27}$$

The weighted sum of the means for each ensemble forecast, μ_k, is set to the mean of the measured wind speed at the site under consideration, μ_{v^m}. The sum of the weights is set equal to 1 to ensure a portfolio selection of 100 %. The MVPT is trained on the preceding 33 days to determine the optimal weights for the ensemble synthesis for the day ahead forecast. This training period is determined through a sensitivity study which minimises the MAE of the synthesized forecast for the first two months of data.

2.9.3 Implementation of Artificial Neural Network Model

An two-layer feed-forward ANN model is employed to generate a deterministic output from the wind speed ensemble set, V^{f}. Figure 17 shows a simplified diagram of the two-layered architecture. Hyper-parameters are determined through a sensitivity study for the best model fit. Linear activation functions are selected for the input and output layers, with a rectified linear unit selected as the activation function of the hidden layer. The number of neurons in the input layer varies as combinations of environmental covariates are incorporated into the model. This is further described in the following section. The hidden layer and output layers comprise twenty, and one, neurons respectively. Similar to the MVPT, the ANN is trained with a dataset of measured and forecast wind speeds using a number of days within the training set preceding the forecast initialisation, 30 % of which is randomly selection for model validation. The

trained model is subsequently applied to a short-term 24 hour forecast. The optimal length of the training window is determined to be 30 days from a sensitivity study which minimises the MAE of the synthesized forecast for the first two months of data. A gradient-descent algorithm, Adam, is utilised for the optimisation, with a mean-squared error loss function.

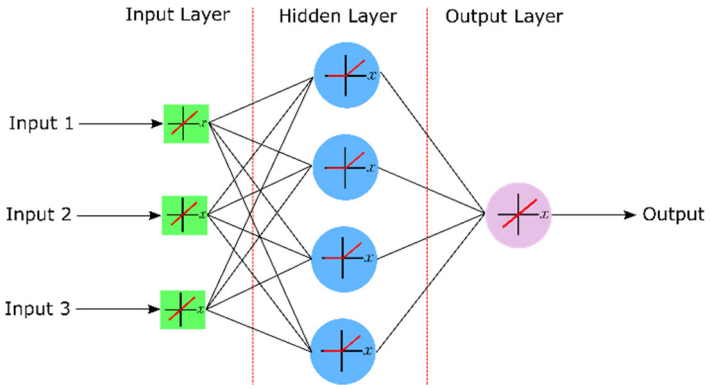

Figure 17. Architecture of the two-layered feed-forward artificial neural network [58].

2.9.4 Performance Evaluation of the Ensemble Combination Models

Further to the analysis of ensemble selection performance of the MVPT and ANN, the benefit gained through multi-model ensemble generation is scrutinised. In the interest of minimising computational run-time by streamlining the ensemble formulation, the benefit derived by increasing the spatial resolution and the creation of additional ensemble models is assessed through the use of 5 cases [58].

Table 8 summarises the ensemble model members selected for each of the optimisation cases. The improvement obtained by increasing the dynamical downscaling of the WRF model with additional nested domains is evaluated by comparing the accuracy of the ensemble synthesis in cases 1, 2, and 3. Similarly, cases 4 and 5 target the improvement achieved by multi-model ensemble models for an optimal deterministic forecast when juxtaposed with case 3.

Table 8: Ensemble member selection for various optimisation cases.

Model Reference	Domain	Case 1	Case 2	Case 3	Case 4	Case 5
ACM2	D1	✓	✓	✓		✓
	D2		✓	✓		✓
	D3			✓		✓
MYJ1	D1	✓	✓	✓	✓	
	D2		✓	✓	✓	
	D3			✓	✓	
MYJ2	D1	✓	✓	✓		
	D2		✓	✓		
	D3			✓		

Table 9 and Table 10 list the results for the synthesised WRF wind speed ensembles for all defined cases. The skill score given in (2.3) is utilised to compare the efficacy of the optimal ensemble

combinations for all cases. The reference, γ^{ref}, is taken from the best performing ensemble member for each case to return a comparative improvement in forecasting skill for all considered techniques and defined ensemble formulations. The ensemble average, MVPT and the ANN model are applied to the defined cases. The significance of various environmental covariates, namely: wind direction, WD, and temperature, T, are tested with the ANN model.

Table 9. MAE (ms^{-1}) of the optimal forecast for the cases studies using the MVPT and ANN models.

Model	Case 1 $\gamma^{ref} = 1.629$ ms^{-1}		Case 2 $\gamma^{ref} = 1.592$ ms^{-1}		Case 3 $\gamma^{ref} = 1.562$ ms^{-1}		Case 4 $\gamma^{ref} = 1.577$ ms^{-1}		Case 5 $\gamma^{ref} = 1.574$ ms^{-1}	
	MAE	**SS**	**MAE**	**SS**	**MAE**	**SS**	**MAE**	**SS**	**MAE**	**SS**
Ensemble Average	1.616	0.798	1.576	1.005	1.521	2.625	1.545	2.029	1.580	-0.381
MVPT	1.605	1.473	1.563	1.822	1.481	5.186	1.529	3.044	1.523	3.240
ANN	1.521	6.630	1.475	7.349	1.438	7.939	1.480	6.151	1.487	5.527
ANN + WD	1.529	6.139	1.481	6.972	1.446	7.426	1.470	6.785	1.491	5.273
ANN + T	1.496	8.165	1.457	8.480	1.433	8.259	1.460	7.419	1.471	6.544

Table 10. Coefficient of Determination (R^2) of the optimal forecast for the cases studies using the MVPT and ANN models.

Model	Case 1 $\gamma^{ref} = 0.636$		Case 2 $\gamma^{ref} = 0.636$		Case 3 $\gamma^{ref} = 0.640$		Case 4 $\gamma^{ref} = 0.634$		Case 5 $\gamma^{ref} = 0.637$	
	R^2	**SS**	**R^2**	**SS**	**R^2**	**SS**	**R^2**	**SS**	**R^2**	**SS**
Ensemble Average	0.670	5.346	0.682	7.233	0.698	9.063	0.691	8.991	0.684	7.378
MVPT	0.670	5.346	0.681	7.076	0.702	9.688	0.691	8.991	0.691	8.477
ANN	0.697	9.591	0.714	12.264	0.729	14.623	0.714	12.618	0.711	11.617
ANN + WD	0.698	9.748	0.713	12.107	0.728	14.465	0.714	12.618	0.709	11.303
ANN + T	0.706	11.006	0.719	13.050	0.730	14.780	0.719	13.407	0.717	12.559

The optimisation of case 3 results in the lowest MAE, and largest R^2, and is, therefore, the most accurate deterministic forecast for all ensemble synthesis techniques. The ensemble average and MVPT improve the synthesised forecast from a MAE SS of 0.798 % to 2.625 % and from 1.473 % to 5.186 % respectively from case 1 to case 3. The larger ensemble with a finer horizontal resolution, therefore, results in a more accurate deterministic forecast, the merits of which may be determined through a cost-benefit analysis of required accuracy versus increased computational expense. The value of the probabilistic range generated by the ensembles should also be considered. Case 3 is selected as the point of departure in the interests of determining the most accurate meso-scale forecast.

The largest skill score is achieved by the ANN+T model, which returns an 8.259 % improvement in MAE over the best individual ensemble member forecast. The inclusion of wind direction as a covariate with the ANN model results in a degradation in forecasting skill for case 3, but an improvement in forecasting skill for case 4. This is potentially due to the training window of 33 days no longer being optimal with the additional covariate.

Figure 18 shows a comparison of the individual deterministic forecast's MAEs for all of the explored techniques for case 3. Although the MVPT exhibits a lower forecasting skill score than the ANN, its computational expense is a factor of approximately 24-30 times lower for the analysed dataset. The MVPT, furthermore, is cast in its simplest form and does not have the complex, non-linear capability of the ANN, and does not consider additional environmental variables.

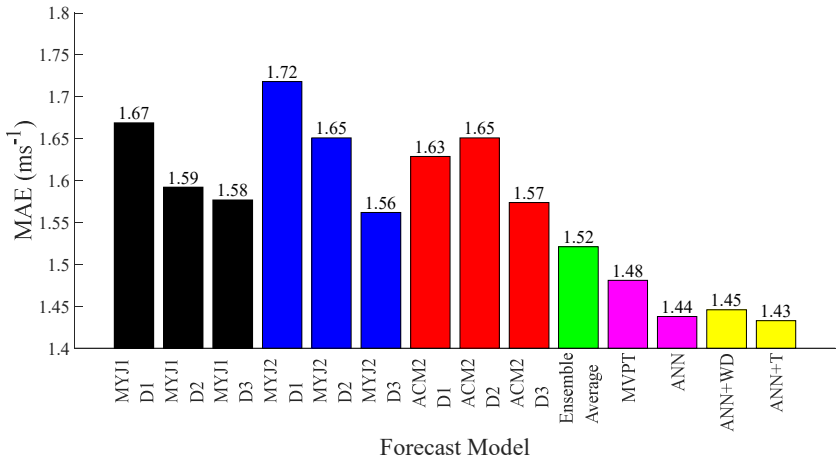

Figure 18. Summary of the MAE for synthesised WRF ensemble members for Case 3.

Figure 19 shows the historical weights of the ensemble members which were selected in the MVPT optimisation using the training window of 33 days prior to the forecast initialisation. The MYJ2 D1 and MYJ2 D2 schemes are not influential in the MVPT synthesis of the ensemble members.

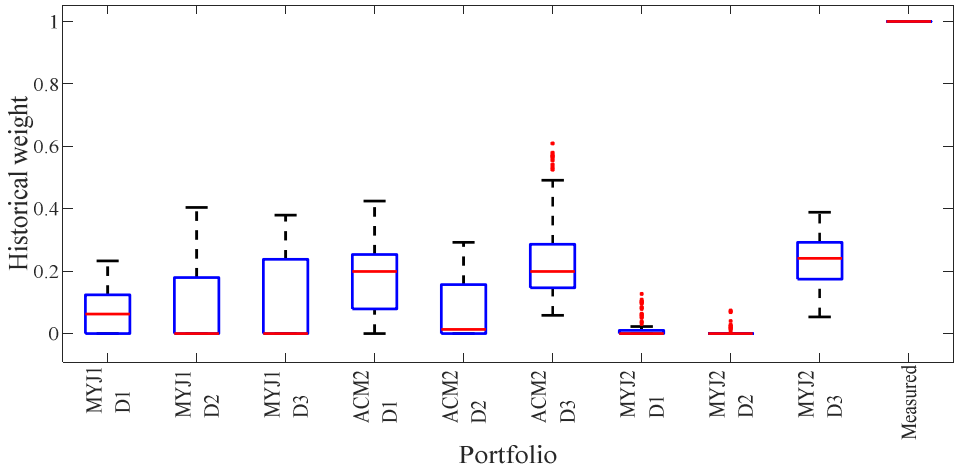

Figure 19. Historical weights of the ensemble members for the duration of the study period.

2.10 Discussion and Conclusions

The derivation of an event-based forecasting tool for the prediction of HWSS events requires an accurate short-term forecasting model as a basis. A physical forecasting model is proposed and implemented using NWP ensemble forecasts, and an optimisation technique to synthesise the WRF-generated ensemble members into an improved meso-scale wind speed forecast. Two optimisation techniques are explored for the wind farm under consideration, namely the MVPT, and a two-layered, feed-forward ANN. The application of the MVPT to the synthesis of a WRF ensemble set for the derivation of a deterministic wind speed is novel. It is shown that the MVPT improves upon the ensemble average with a MAE skill score improvement of 5.186 %, and a R^2 improvement of 9.688 % over the best individual forecast. Although the ANN outperforms the MVPT, with a MAE skill score

improvement of 8.259 % over the best individual ensemble member forecast, the computational runtime of the ANN is a factor of approximately 24-30 times longer than that of the MVPT. The MVPT thus has application in cases where computation time is a practical consideration. The MVPT analysis is similar to a principal component analysis and has potential usability as a pre-processing step for the input parameter selection of ANNs, as well as in the initialisation of the perceptron weights of the ANN model. The MVPT optimisation technique, furthermore, has potential application in the synthesis of large ensemble sets which could potentially cause over-fitting in ANNs.

Chapter 3

Micro-Spatial Wind Speed Modelling for Short-Term Forecasting Applications

3.1 Overview

Spatial modelling of wind farms typically falls within the purview of short-term forecasting or long-term geospatial studies. For long-term geospatial studies, the conversion of wind speed to power generally requires an estimation of the spatial variance of the wind resource in the area of study, the omission of which could result in substantial errors [59]. Studies such as capacity factor potential analyses and optimal renewable portfolio allocation for minimised variance require historical geospatial wind resource datasets [60], such as wind atlases with high spatial resolution and extended historical timelines [61].

It is recognized that sub-hourly temporal scales should be observed for power system studies related to dispatch, unit commitment, cycling, and ramping [62]. Moreover, short-term forecasting conducted in the context of renewable power variability predicates assessment on a sub-hourly temporal resolution [18], [63]. Applications such as performance monitoring, a wind park management approach to power forecasting [64], and the modelling and forecasting of High Wind Speed Shutdown (HWSS) require wind speed data defined at individual turbine level.

Various downscaling methodologies, aimed at estimating wind speeds at multiple highly localised areas of interest from meso-scale data, have been proposed in literature. The spatial interpolation models of the atmospheric state pertaining to the wind resource reported in literature adopts either a physical, statistical, or hybrid approach, where the hybrid models are composed of physical and statistical models.

Physical models typically include dynamical downscaling by Numerical Weather Prediction (NWP) models and Computational Fluid Dynamics (CFD) models. The CFD models are computationally intensive as they require initial states, boundary conditions, as well as accurate, high-resolution implementations of the applicable topography, wake models, etc. [65]. The application of detailed CFD models is, therefore, to some extent, precluded for short-term forecasting applications, due to the associated computational expense. Expeditious solutions have been proposed, such as the implementation of idealised CFD models and the usage of transfer coefficients for simulation scaling, or through the determination of pre-calculated flow fields [66].

Statistical models encode the complex non-linear relationships between covariates and the meso and micro-scale wind speeds to derive a transfer function for downscaling. The statistical downscaling models reported in literature include Artificial Neural Networks (ANN) [67], support vector regression, random forests [68], Bayesian models [69], etc.

Li *et al.* [67] used ANNs to estimate the power output of individual turbines using measurements from an on-site meteorological mast in the input layer. Individual ANN models were trained for four turbines over the course of a month, and validated on the measured power generation profile for the following month. The largest percentage difference reported between measured and predicted power was approximately 4 %. Although no forecasts were generated, this work demonstrates the ability of ANNs to estimate wind speeds at point locations in a wind farm. The methodology is, however, cumbersome for large wind farms, as the individual ANNs require extensive modelling and time-consuming performance evaluation. A single model with multiple output neurons representing the individual turbines is, furthermore, expected to require extensive computational power.

Salcedo-Sanz *et al.* [64] proposed a hybridised model for short-term wind speed prediction. The methodology produced a mean hourly wind speed forecast using the fifth-generation meso-scale model (MM5), coupled with an ANN model for statistical downscaling. A forecast was derived for each of the 33 turbines in the wind farm with a reported MAE ranging from approximately 1.45 ms^{-1} to 2.2 ms^{-1} for a 48 hour forecast horizon over a period of 6 months.

Castellani *et al.* [62] compared two forecasting techniques for a wind farm comprising 12 turbines in complex terrain. The first methodology involves the application of ANN models to predict the power at each turbine from an NWP input. The second approach uses a hybrid ANN-CFD model, where the ANN model is utilised to forecast the wind speed for a meteorological mast based on historical measurements, while the CFD model is subsequently used to estimate the power output of individual turbines. The ANN downscaling models show good performance, with a coefficient of determination of approximately 0.75 to 0.83 for an hourly mean wind speed forecast, with a 24 hour forecast horizon for one month. The CFD model, however, returned a comparatively poor forecast, the cause of which is cited as the terrain complexity. Castellani *et al.* improved upon the previous methodology, by comparing a pure ANN approach with a hybrid ANN-CFD model with an NWP input [65]. The study involved 24 turbines over the course of 7 months, with weekly interleaved training and testing sets to instantiate homogeneity in order to avoid bias. Results show that both approaches demonstrate similar skill. It is expected, however, that the performance of the ANN model would improve with larger training sets. It is noteworthy, furthermore, that the authors concluded that terrain complexity impacts negatively on the ability of the CFD model to resolve the local dynamics.

Micro-scale spatial wind speed dispersion has been modelled primarily with the view to derive an equivalent wind farm power curve for the conversion of a single-point wind speed profile to an aggregated wind farm power profile. Various models, including spectral models, multi-turbine power curves and Markov models, have been proposed to describe this spatial variance across various time scales [70] - [78].

Spectral methods, such as the cross-spectral model theorised by Sorensen *et al.* [74] for grid compliance

regulation of power fluctuation, are useful for the modelling of the dynamic interaction between wind turbines on a time scale of the order of seconds. This model was demonstrated on a temporal scale of 0.2 seconds to 1 minute. Subsequent improvements in the coherence and power spectral density functions extended the capability of the model to incorporate variability in the time range between minutes to a few hours [75]. Good correlation was obtained between simulated and measured wind speeds for small and large wind farms.

The multi-turbine power curve proposed by Norgaard and Holttinen [77] represents one of the most commonly used models aimed at characterising the effects of micro-scale wind speed dispersion. A Gaussian spatial wind speed distribution is adopted for the area of interest. The associated normalised spatial standard deviation is determined from an estimation of the local turbulence intensity and the dimension of the wind farm. In the initial study, the parameterised relation of these quantities is determined for the Nordic regions. This technique has since been widely applied in other parts of the globe with varying topographies and climates [79], [80].

In a similar approach, Gibescu *et al.* [73] proposed a Gaussian distribution of spatial wind speeds, called a Gaussian filter. In this work, the spatial standard deviation is determined by the wind farm area, the number of wind turbines, and a decay parameter. The decay parameter is commonly used in trans-locational wind studies, and encapsulates the covariance between location pairs as a function of the distance between them. The decay parameter, however, varies with time scale and terrain complexity, as is evidenced by the contrasting values reported in literature [81] - [83].

He *et al.* [78] proposed a model for very short-term forecasting horizons by incorporating spatial dynamics using graph theory into a Markovian forecast. Spatial statistics are learnt by the model for a large 300 MW wind farm over the course of a year. A finite-state Markov model is subsequently derived and utilised in the testing for the same month and 3-hourly epoch of the following year. The derived Markov chain, coupled with the present generation level and short-term complementary information, such as ramp trending, is utilised to generate an online forecast for wind farm power. The results show consistent improvement over the persistence model is achieved for each month of the testing period.

The primary research objective targeted in this study involves the short-term forecasting of HWSS events in an operational context. The modelling of HWSS has to be conducted at micro-scale level using turbine-specific wind speed profiles, power curves, and HWSS control protocols. This requires site-specific downscaling of meso-scale wind speed and wind direction forecasts to wind speeds at individual turbines. In the context of short-term forecasting, the computational costs associated with the meso-scale forecasting model and the associated downscaling model is of major importance. The physical micro-scale modelling approach, which typically involves computational-intensive CFD models, is not regarded as an optimum methodology. The statistical approach offers the advantage that multiple site-specific models can be pre-trained using measured historical data, and employed for the

site-specific translation of meso-scale forecasts to a forecast at turbine level for a given operational wind farm.

A novel statistical methodology is proposed in this dissertation to translate a meso-scale wind speed profile into multiple archetypal profiles which are statistically representative of the wind speeds at individual wind turbines at a large wind farm. The methodology employs a Monte Carlo approach for the optimisation of site-specific spatial wind speed distributions which are derived using historical data. The model employs random sampling of the spatial wind speed distribution, and optimised seeding to determine statistical samples of wind speeds at the micro-scale level. An optimisation procedure is implemented for different spatial wind speed distributions which are partitioned by the wind flow conditions as well as along seasonal timelines. The optimisation loop employed in the training process ensures that the optimal deterministic transfer function is determined for each of the dataset partitions. The derived micro-scale wind speeds are subsequently mapped to wind speeds experienced by individual turbines using the proposed turbine ranking and mapping model. Results are presented for a utility-scale wind farm.

3.2 Model Topology and Implementation

3.2.1 Overview

Figure 20 shows a block diagram of the downscaling model proposed in this investigation. The model uses a site-specific spatial wind speed distribution that is derived from historical data using a training process. The statistical wind speed distribution is scaled using the meso-scale wind speed at the site, and the scaled distribution is randomly sampled. The resulting wind speeds are mapped to individual turbine locations using a pre-trained ANN turbine ranking model.

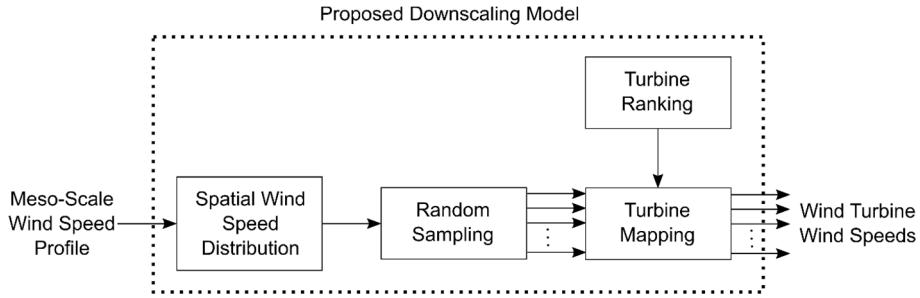

Figure 20. Block diagram of the proposed downscaling model which translates a meso-scale wind speed profile into micro-scale wind speed estimates at physical turbine locations.

3.2.2 Training Methodology

3.2.2.1 Overview

Figure 21 shows a block diagram of the training methodology implemented to derive the site-specific spatial wind speed distributions used in the statistical downscaling model. Based on the work of

Norgaard and Holttinen [14], a Gaussian spatial wind speed distribution is assumed. The measured nacelle wind speeds for a given sampling interval are aggregated to obtain the mean of the wind speed distribution used for the sampling interval. A set of spatial wind speeds is derived from the wind speed distribution using a random sampling process. These wind speeds are mapped to individual turbines using a turbine ranking model. An objective function is derived using the residuals found between the measured and simulated turbine wind speeds. This objective function is used to optimise the statistical parameters of the spatial wind speed distribution. The individual functions are described in the following subsections.

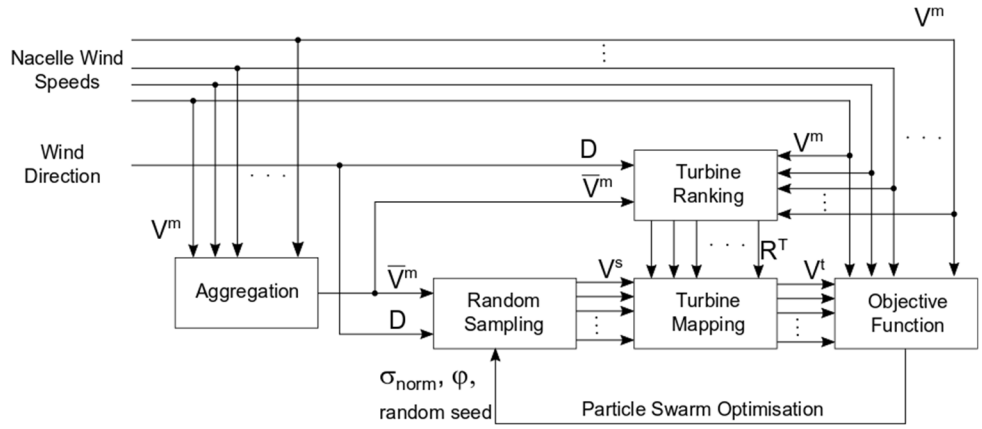

Figure 21. Block diagram of the training implementation for the proposed statistical downscaling model.

3.2.2.2 Wind Speed Dataset

The optimised spatial wind speed distributions are derived using a historical tempo-spatial wind speed dataset for the targeted site, which consists of measured nacelle wind speeds averaged over a given sampling interval, as well as a wind direction measurement from the on-site meteorological mast. The set of sampling times associated with the dataset can be represented mathematically by T^m, given by

$$T^m = \{ t_i, \quad i = 1, 2, 3, \dots, N_i \}, \tag{3.1}$$

where t_i denotes the time for the i^{th} sampling interval, and N_i denotes the number of sampling intervals in the dataset. The set of measured nacelle wind speeds, V^m, is then denoted by

$$V^m = \{ V_i^m, \quad i = 1,2,3, \dots, N_i \}, \tag{3.2}$$

with

$$V_i^m = \{ v_j^m(t_i) | \quad t_i \in T^m, \quad j = 1,2,3 , \dots, N_j \}, \tag{3.3}$$

where $v_j^m(t_i)$ denotes the measured wind speed for the j^{th} wind turbine, and N_j denotes the number of wind turbines at the wind farm. The wind direction, D, measured by the on-site meteorological mast is given by

$$D = \{ d(t_i), \quad t_i \in T^m \}, \tag{3.4}$$

where $d(t_i)$ denotes the measured wind direction for the i^{th} sampling interval at time t_i.

3.2.2.3 Aggregation of Measured Nacelle Wind Speeds

The site-specific spatial wind speed distributions used in the proposed approach uses the mean wind speed of the site for the sampling interval of interest as an input parameter. During training and model testing, this mean wind speed is derived from measured nacelle wind speeds. The set of mean wind speeds, $\overline{V}^m$, is defined as

$$\overline{V}^m = \{\bar{v}_i^m, \quad i = 1, 2, 3, \dots, N_i\}, \tag{3.5}$$

with

$$\bar{v}_i^m = \frac{1}{N_j}\sum_{j=1}^{N_j} v_j^m(t_i), \tag{3.6}$$

where $\bar{v}_i^m$ denotes the mean value of the spatial wind speeds associated with the i^{th} sampling interval. The aggregated set, $\overline{V}^m$, is used as an input into the random sampling model.

3.2.2.4 Random Sampling of the Spatial Wind Speed Distribution

A Monte Carlo approach is utilised to determine the optimal transfer function representing the relation between the meso-scale wind speed and the turbine wind speeds at the wind farm under investigation. In this process, the repeated random sampling of a statistical distribution is undertaken to determine the statistical parameters of the distribution which results in the minimised residual wind speed errors when compared with the supervised target dataset, i.e. the measured nacelle wind speeds. The seed of the pseudorandom number generator is furthermore varied to optimise the location of the samples drawn from the distribution. The resulting process is consequently deterministic in nature.

A Gaussian spatial wind speed distribution is implemented, based on previous studies reported in literature [73], [77] - [80], [84], and due to the fact that it only has one parameter. This promotes computational expedience, particularly for population-based optimisers. It is understood that the spatial distribution of wind speeds is prone to variation, and that no single distribution will adequately model the underlying wind farm dynamics. Tempro-spatial partitioning and optimised seeding are therefore utilised to acquire an average estimation of the best deterministic fit of the data with the Gaussian functioning primarily as the umbrella distribution within which the variation may occur. The Gaussian distribution is defined by the following equation:

$$g(x + \varphi) = \frac{1}{\sqrt{2\pi\sigma^2}} e^{-\frac{((x+\varphi)-\mu)^2}{2\sigma^2}}, \tag{3.7}$$

where μ, σ and φ denote the mean, standard deviation, and the mean offset respectively. During optimisation of the spatial wind speed distribution, the mean of the distribution for the i^{th} sampling interval is derived from the mean of the measured spatial wind speeds for the interval, such that

$$\mu = \bar{v}_i^m. \tag{3.8}$$

The mean offset is incorporated into the model, in conjunction with the optimised random generator seed, to account for any meso-scale forecasting biases, as well as for skewed distributions. The set of simulated wind speeds, V^s, obtained by random sampling of the Gaussian distribution is defined as

$$V^s = \{ V_i^s, \quad i = 1,2,3, \dots, N_i\}, \tag{3.9}$$

with

$$V_i^s = \left\{v_j^s(t_i) \middle| \ i = 1,2,3, \dots, N_i, \quad j = 1, 2, 3, \dots, N_j\right\}, \tag{3.10}$$

where $v_j^s(t_i)$ denotes the j^{th} simulated spatial wind speed for the i^{th} sampling interval. The set of micro-scale wind speeds for the i^{th} sampling interval is generated by

$$V_i^s = \mu \cdot \sigma_{norm} \cdot h(N_j) + \bar{v}_i^m + \varphi, \tag{3.11}$$

where the normalised spatial standard deviation, σ_{norm}, is

$$\sigma_{norm} = {}^{\sigma}/_{\mu}. \tag{3.12}$$

The Marsenne twister pseudo-random number generator [85], denoted by h in (3.11), is utilised to create a set, V_i^s, of N_j numbers with a standard deviation of σ, and a mean of $\bar{v}_i^m + \varphi$. The derived set of spatial wind speeds is returned as a random sampling of the applicable normal distribution. These wind speeds are, consequently, statistically representative of the micro-scale wind speeds at the site. Figure 22 shows a graphical example of the random sampling procedure for ten turbines for a single sampling interval.

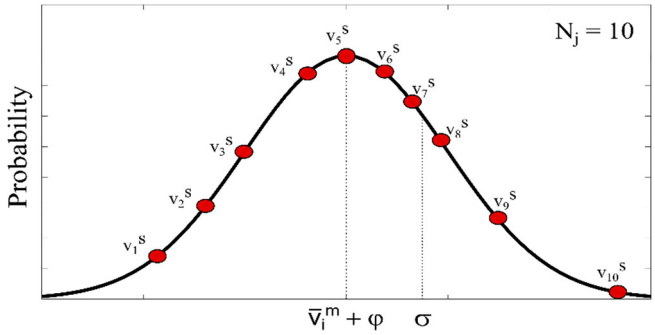

Figure 22. Example of the random sampling process for 10 turbines using a Gaussian distribution.

The randomly sampled wind speeds derived for each sampling interval are ranked by order of magnitude in order to facilitate bijective mapping of the wind speeds to individual turbines in the next step. The wind speeds associated with the i^{th} sampling interval are thus arranged such that

$$v_j^s(t_i) \leq v_{j+1}^s(t_i). \tag{3.13}$$

With the simulated wind speeds in this format, the turbine mapping procedure can relate the lowest wind speed to the lowest ranked turbine based on prevailing conditions, the second lowest wind speed

to the second lowest ranking turbine, and so on.

3.2.2.5 Turbine Ranking and Spatial Wind Speed Mapping

The nacelle wind speeds at individual turbines are highly dependent on wind flow conditions, turbine layout, and terrain topography. For simple, flat terrain with the average inflow direction illustrated in Figure 23, for example, it is expected that turbines 1, 2, and 3 will be exposed to the highest average wind speeds. As the front row of turbines acts as momentum sinks due to the wake effect, the turbines down the line will be exposed to lower average wind speeds. It is postulated that, for a given scenario of meso-scale meteorological conditions, a turbine ranking order characterised in terms of the magnitude of wind speeds to which the individual turbines are exposed, can be derived. It is expected that the turbine ranking will remain relatively consistent for similar conditions. Non-linear statistical models can be used to estimate the turbine ranking for each sampling interval. Additional covariates such as wind speed, wind direction, time of day, season, temperature, pressure, and wind shear could potentially be incorporated into the model for an improved prediction.

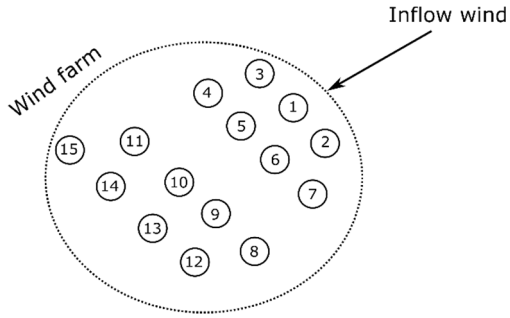

Figure 23. Turbine ranking is directly dependent on the inflow wind angle and exposed layout of the wind farm.

In this investigation, an ANN model is utilised to derive turbine ranking through the supervised learning of the relation between tempro-spatial meteorological information and nacelle wind speeds. Figure 24 shows the training architecture of the proposed model. A four-layered, feed-forward ANN model takes the mean wind farm wind speed, wind direction, and hour of the day as inputs. The set of measured nacelle wind speeds, V^m, is used as the supervised target. This model comprises four layers of 20, 60, 240, and N_j neurons respectively, where N_j represents the number of turbines. The hyper-parameters of the ANN model are tuned through a sensitivity analysis to produce the lowest residual error for the training period. Linear activation functions are specified for the input and output layers, and rectified linear unit activation functions for the hidden layers. A quarter of the dataset is randomly sampled without replacement for the training data, with 30 % for validation, and another quarter of the dataset for the testing of the model.

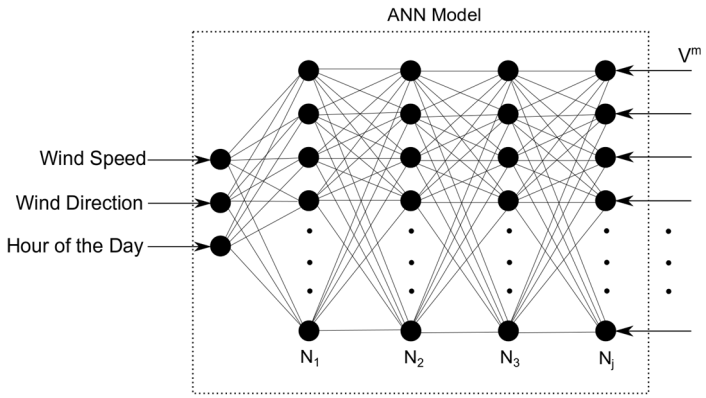

Figure 24. Training architecture for the proposed turbine ranking model.

Figure 25 shows the proposed model architecture used to determine the turbine ranking set for given wind flow conditions, and hour of the day. The trained ANN model estimates turbine wind speeds for the given input conditions which are subsequently ranked in ascending order. A ranking is ascribed to each turbine, from 1 to N_j, with a 1 indicating the turbine with the lowest wind speed, and N_j indicating the turbine with the highest wind speed for the given input conditions.

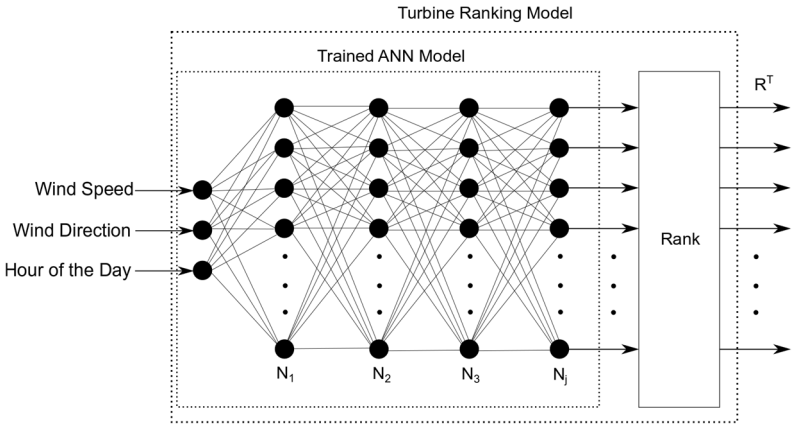

Figure 25. Proposed model architecture to determine the ranking of wind turbines for given wind flow conditions.

Turbine ranking is used in the bijective mapping of ordered, simulated wind speeds to physical turbines for the given wind flow conditions. Figure 26 illustrates an example of the bijective mapping for a set of five ordered spatial wind speeds, V^s. This process is defined as

$$f: V^s \rightarrow V^t, \tag{3.14}$$

where V^s is mapped by a function, f, to the turbine wind speeds, V^t, according to the turbine ranking set, R^T, where

$$R^T = \{ R_i^T, \quad i = 1,2,3, \dots, N_i \}, \tag{3.15}$$

with

$$R_i^T = \{ r_j^T(t_i) | \quad i = 1,2,3, \dots, N_i, \quad j = 1,2,3, \dots, N_j \}. \tag{3.16}$$

For this example, the second lowest wind speed, $v_2^s(t_i)$, is mapped by $r_1^T(t_i)$ to turbine one, $v_1^t(t_i)$. The highest wind speed, $v_5^s(t_i)$, is mapped by $r_2^T(t_i)$ to turbine two, $v_2^t(t_i)$, and so on.

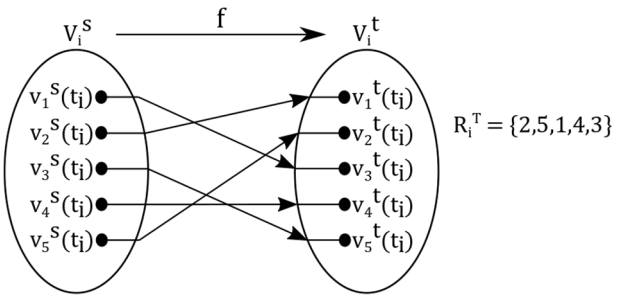

Figure 26. Bijective mapping of spatial wind speeds to physical turbine locations using the turbine ranking set.

The resulting turbine wind speed set, V^t is defined by

$$V^t = \{ V_i^t, \quad i = 1,2,3, \dots, N_i \}, \tag{3.17}$$

with

$$V_i^t = \{ v_j^t(t_i) \mid \ i = 1,2,3, \dots, N_i, \quad j = 1,2,3, \dots, N_j \}. \tag{3.18}$$

3.2.2.6 Objective Function and Optimisation Process

An optimisation algorithm is implemented to minimise an objective function, C, which is defined by the relationship

$$C = \sum_{i=1}^{N_i} \sum_{j=1}^{N_j} v_j^r(t_i)^2, \tag{3.19}$$

where

$$v_j^r(t_i) = v_j^t(t_i) - v_j^m(t_i), \tag{3.20}$$

with

$$V_i^r = \{ v_j^r(t_i), \ j = 1,2,3, \dots, N_j \}, \tag{3.21}$$

and

$$V^r = \{ V_i^r, \quad i = 1,2,3, \dots, N_i \}. \tag{3.22}$$

The objective function is defined as the sum of the squared set of residual wind speeds, V^r, which is determined from the difference between the measured and predicted turbine wind speeds. In terms of the above definitions, a positive residual wind speed indicates an over-prediction of wind speed, whereas a negative residual indicates an under-prediction. The squared residuals accentuate the large errors in the dataset, and further remove the influence of the sign. This aids in the reduction of large over and under-predictive errors.

The objective function is minimised using a Particle Swarm Optimisation (PSO) algorithm [86]. PSO

is selected based on a proven capability for determining global optima [87]. To minimise the predictive error, the properties of the statistical spatial distribution are adjusted by the optimisation loop. By iteration, the optimal values for the normalised spatial standard deviation, σ_{norm}, the mean offset, φ, and the seed of the random generator function are determined.

3.3 Performance Evaluation

The proposed methodology is implemented and evaluated for the measured wind resource dataset of an operational utility-size windfarm with a rating of the order of 100 MW situated in semi-complex terrain. The wind speed and wind direction data is acquired with a temporal resolution of 10 minute sampling intervals for 1 year, i.e. 01 December to 31 November. The dataset is partitioned along temporal and spatial dimensions with the view to derive different models based on wind flow conditions. The resulting partitions are subsequently divided further into training and testing sets.

3.3.1 Data Partitioning

The spatial distribution of wind speed at a site is predicated upon many factors. A change in meteorological conditions will alter the spatial distribution of wind speeds at a site. Data partitioning attempts to encapsulate these variations by dividing the dataset according to wind direction and wind speed ranges. To accommodate the variation caused by the fluctuating meso-scale wind conditions, the data is partitioned into 32 sections, i.e. 4 wind speed ranges and 8 wind direction ranges, as illustrated in Figure 27.

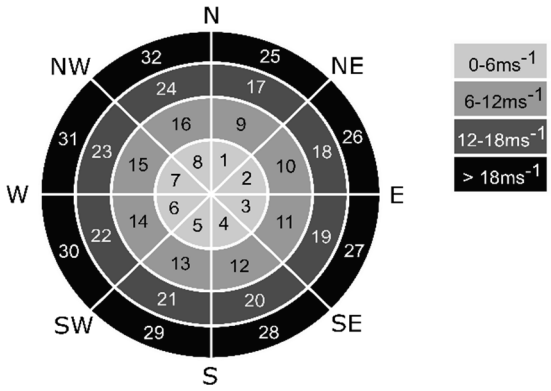

Figure 27. Wind speed and wind direction dataset partitions.

Each sector may be represented as a subset of the wind speed dataset, for example:

$$V_{17}^{m} = \left\{ \begin{matrix} V_i^m \mid V_i^m \in V^m,\ 12 \le \bar{v}_i^m < 18, \\ 0 \le d(t_i) < 45,\ d(t_i) \in D,\ t_i \in T^m \end{matrix} \right\}. \tag{3.23}$$

The seasonal characteristics suggest a further division of the dataset into the subsets displayed in Figure 28.

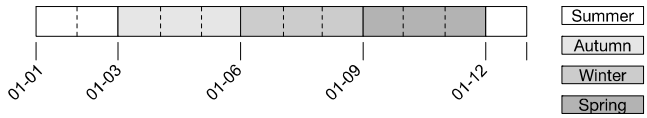

Figure 28. Temporal partitioning of the dataset into seasonal data sets.

Training and testing subsets are segregated using interleaved sampling without replacement. The training and test sets are therefore of an equivalent size for each seasonal partition. It is recognised that this sequence is not representative of a scenario which could be implemented in practice, and is undertaken with the sole purpose of evaluating the model without the bias inherent in the dataset. It is furthermore necessary to adopt this approach due to the small dataset available for this study to ensure that each partition contains samples for training and testing.

3.3.2 Optimised Statistical Parameters

Figure 29 shows the seasonal optimisation parameter values for each of the defined partitions, which result in the minimisation of the objective function defined in (3.19). The results show the importance of partitioning by wind speed and wind direction, and give rise to the following observations:

- Seasonal discrepancies in the normalised standard deviation indicates that a singular spatial partition for the site is not adequate. Temporal partitioning is required to account for these variations which arise due to changes in meteorological processes.
- A change in the wind direction results in a shift in the normalised standard deviation. This is most evident in summer, for partitions 19, 20, and 21, where the standard deviation is 0.083, 0.254, and 0.093 respectively.
- Similarly, an increase in wind speed causes an increase in the normalised standard deviation. An example is seen in spring, where the partitions 5, 13, 21, and 29 are 0.043, 0.109, 0.144, and 0.212 respectively.
- The translation parameter is predominantly near 0 ms^{-1} as the mean wind farm wind speed is utilised as an input. Optimisation of the mean offset of the training data extends the flexibility of the model as it allows for bias correction of the input. This could potentially be useful when utilising a reference point such as a meteorological mast for nowcasting applications, and a meso-scale forecast which has inherent tempro-spatial biases.

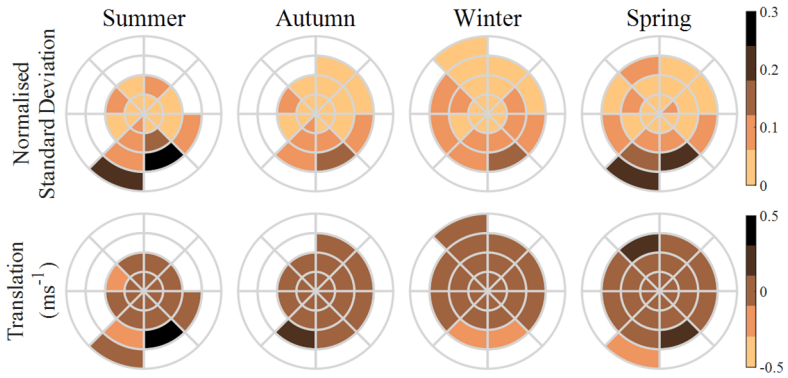

Figure 29. Seasonal optimisation parameter values for each of the defined partitions, which result in the minimisation of the objective function defined in (3.19).

3.3.3 Performance Evaluation

For each sampling time, t_i, the optimal statistical parameters are selected from the relevant partition in Figure 27. Similarly, the turbine ranking is also determined from the pre-trained ANN as described in section 3.2.2.5. The resulting spatial distribution is sampled and subsequently mapped to individual turbines using the bijective mapping function. Residual wind speeds are determined, and the errors are computed using the MAE and MAPE metrics. The MAE for each turbine is formulated as follows:

$$\mathrm{MAE(j)} = \frac{\sum_{i=1}^{N_i} \left| v_j^r(t_i) \right|}{N_i}. \tag{3.24}$$

Figure 30 displays the boxplot showing the seasonal MAE for each turbine in the wind farm. The Inter-Quartile Range (IQR) spans from approximately 0.65 ms^{-1} to 0.95 ms^{-1} with a seasonal median ranging from approximately 0.73 ms^{-1} to 0.8 ms^{-1}. Similar downscaling skill is achieved for all seasons, with summer yielding the best performance, and autumn conceding the largest MAE.

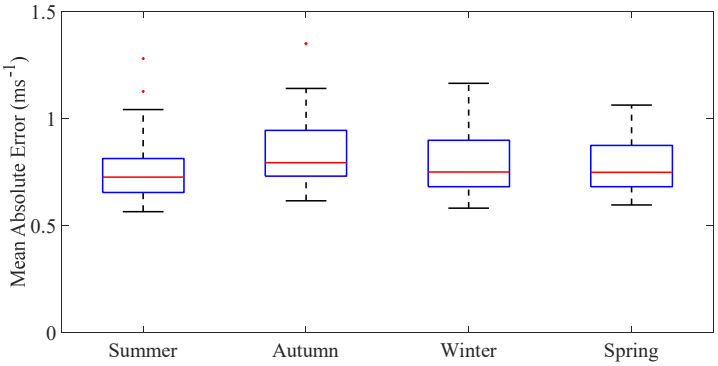

Figure 30. Boxplot showing the seasonal MAE for each turbine in the wind farm from (3.24).

The models' MAE is analysed for each partition by adapting (3.24) as follows:

$$\mathrm{MAE} = \frac{\sum_{j=1}^{N_j} \left(\sum_{i=1}^{N_i} \left| v_j^r(t_i) \right| \right)}{N_j \cdot N_i}. \tag{3.25}$$

With the individual turbine residuals ingested into the MAE formulation, a single MAE figure is acquired for each partition. Figure 31 shows the graphical plot of the seasonal MAE for each the data partitions associated with the 4 wind speed and 8 wind direction ranges. The results show that the most accurate downscaling is achieved in spring with a MAE of 0.7 ms^{-1}, whilst the worst performance is obtained in autumn with a MAE of 0.8 ms^{-1}. The partition errors are relatively consistent, with only one partition in excess of 1.5 ms^{-1}, i.e. partition 21 in winter.

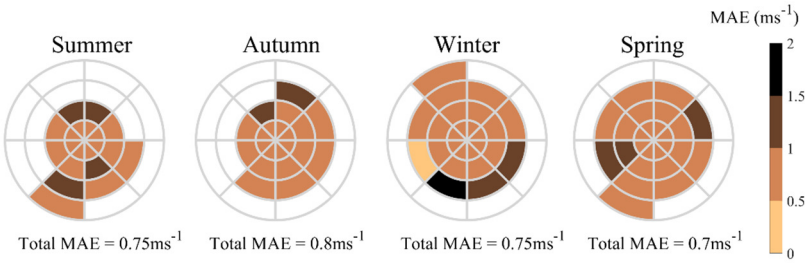

Figure 31. Seasonal MAE for the data partitions associated with the 4 wind speed and 8 wind direction ranges.

The MAPE for each wind turbine is defined by the relationship [88]

$$\mathrm{MAPE(j)} = \frac{100\left(\sum_{i=1}^{N_i}\left|v_j^r(t_i)/v_j^m(t_i)\right|\right)}{N_i}. \tag{3.26}$$

MAPE is utilised to determine the error as a percentage of the measured wind speed for a relative estimation of the forecasting error. Large errors are excluded from the analysis by neglecting the time intervals with measured wind speeds below the cut-in wind speed of 3 ms^{-1}. This action has a negligible impact on the analysis as these wind speeds have no relevance for wind turbine applications [89].

Figure 32 shows a boxplot of the seasonal MAPE of all turbines at the wind farm. The MAPE ranges from 5.6 % to 12.3 %, with an IQR extending from 6.2 % to 9.2 %, while the medians for all seasons are situated at approximately 8 %. The MAPE is relatively consistent across all seasons. The larger MAE for autumn is attributed to the fact that larger errors occurred for the higher prevailing wind speeds during this season.

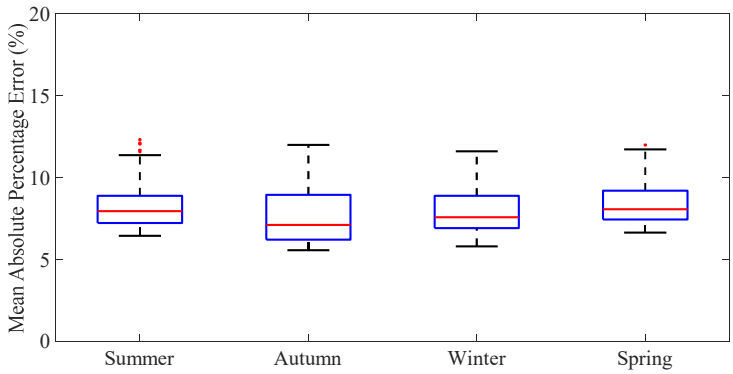

Figure 32. Seasonal MAPE of all turbines at the wind farm.

3.4 Discussion and Conclusions

A novel statistical downscaling methodology is presented in pursuit of a computationally expedient model for the estimation of wind speeds within a wind farm. It is further required that this tool demonstrate skill with small training datasets. Data-driven techniques traditionally require large datasets in order to sufficiently train models to capture the complex non-linear relationships in the data.

A Monte Carlo optimisation approach is proposed to derive optimal statistical parameters for tempro-spatial partitions of the distributions describing the average instantaneous wind speeds. The spatial profiles are sampled randomly to generate probabilistic wind speeds which are subsequently ordered according to a pre-trained ANN turbine ranking and mapping system. The seed of the sampling generator is optimised to determine the optimal deterministic solution for the partition based on the training dataset.

The trained model is tested on a seasonal, interleaved dataset with the mean wind farm wind speed as an input to determine the efficacy of the model. Error metrics show that the method produces accurate estimations of the individual turbine wind speeds, with the largest errors being 1.3 ms^{-1} and 12.3 % for the MAE and MAPE respectively. The median error is approximately 0.8 ms^{-1} or 8 % for the same metrics respectively.

This method has application in the arena of site-specific downscaling for forecasting applications, as well as for the statistical modelling of events such HWSS events, which have to be modelled at the turbine level using a given turbine power curve and operational parameters. The latter application includes the modelling and forecasting of high wind speed shutdown for wind turbines, identification of optimal outage periods for scheduled maintenance, etc.

The proposed methodology can be readily adjusted for objectives such as short-term forecasting of wind farm power generation profiles, through modification of the objective function. In this case, the approach has the advantage of bypassing multi-turbine power curve errors and production losses, as the model is trained on measured historical data for individual turbines. The proposed model is furthermore computationally expedient, and the statistical parameters are easy to update.

No assumptions or additional models are required in the process. Once optimised, the influence of the wake effect, the local terrain and surface roughness, are all contained in the model. Additional work is required to evaluate the performance of the methodology for more expansive wind farm sites, different training and testing sequences and various temporal scales and partition schemes.

Chapter 4
Wind Speed Event Forecasting using a Wind Speed Threshold Model

4.1 Overview

In the context of wind power ramping phenomena, High Wind Speed Shutdown (HWSS), potentially, represents the most severe risk to power system stability [6] - [8]. Accurate probabilistic forecasting of ramping events has been shown to offer clear benefits [14]. A dedicated event-based forecasting tool has the potential to assist the System Operator in initiating pre-emptive actions such as efficient dispatch and scheduling, as well as with the optimal allocation of ancillary services. The forecasting of ramping events has recently gained traction due to the ubiquitous expansion of renewable energy. Many ramp-rate event forecasting models have been proposed in literature, examples of which can be seen in the works of Bossavy *et al.* [90], and Taylor [91]. No such models have been presented for the forecasting of HWSS events.

Traditional forecasting techniques are geared towards minimisation of bulk error metrics in an effort to minimise forecast errors across a wide range of wind speeds. Consequently, these techniques do not forecast event conditions such as rapid-rate ramp events adequately. HWSS event forecasting requires a technique that is capable of accurately predicting the number of turbines exceeding high wind speed thresholds. The forecasting and quantification of the impacts of HWSS events is complicated in practice because the driving mechanisms are complex, infrequent and fast-forming. Site-specific wind dynamics, furthermore, plays an important role at the micro-scale level due to local wind speed dispersion behaviour and wake effects, both of which are affected by mean wind speed and wind direction.

Two novel methodologies for the forecasting of HWSS events are proposed and evaluated, namely an Artificial Neural Network (ANN) model and an alternative methodology based on the statistical downscaling technique proposed in Chapter 3. Both methodologies employ a novel event model defined in terms of the number of turbines in HWSS mode.

4.2 High Wind Speed Shutdown Event Model

4.2.1 Overview

The proposed models are evaluated for a wind speed threshold which is applied to the measured turbine nacelle data. Exceedance of the threshold results in an event analogous to an HWSS event.

4.2.2 Model Topology

Figure 33 illustrates the concept implemented by the HWSS event model. An HWSS event is characterised by a start time, end time, and the number of turbines that exceed a predetermined wind speed threshold for each of the successive sampling intervals that comprises the event lifespan.

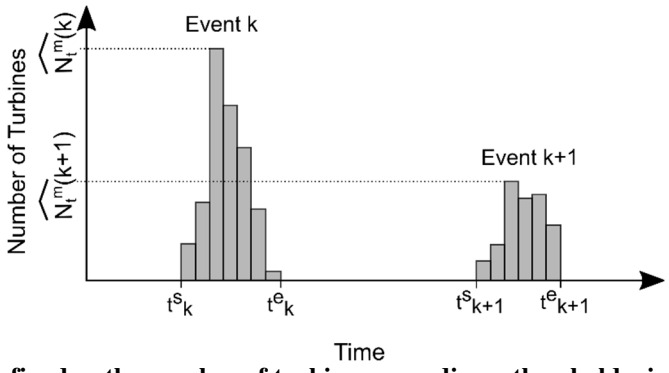

Figure 33. Events are defined as the number of turbines exceeding a threshold wind speed versus time.

The sets of start and end times, denoted by T^s and T^e respectively, are given by

$$T^s = \{t_k^s \mid t_k^s \in T, k = 1,2,3, \dots, N_k\}, \tag{4.1}$$

and

$$T^e = \{t_k^e \mid t_k^e \in T, k = 1,2,3, \dots, N_k\}, \tag{4.2}$$

where k and N_k represent the event index and number of events respectively. Parameter $\widehat{N_t^m}$ denotes the maximum number of turbines exceeding the wind speed threshold for each event.

The number of turbines exceeding the wind speed threshold for the i^{th} sample can be represented by the following relation:

$$N_t(t_i) = \sum_{j=1}^{N_j} v_j^m(t_i) > v^{th}, \tag{4.3}$$

where $N_t(t_i)$ denotes the number of wind turbines in exceedance of a wind speed threshold for the i^{th} sampling interval, and v^{th} denotes the wind speed threshold.

Two wind speed thresholds are defined for the case studies with the view to represent both frequent and infrequent events. Frequent events are represented by a mid-range threshold of 12 ms^{-1}, while infrequent events are represented by a high range threshold of 18 ms^{-1}. The wind speed threshold of 18 ms^{-1} is selected as this represents a relatively rare high wind speed condition for the target site, in the sense that only 0.5 % of the sampled wind speeds at all turbines exceed this wind speed. This is less than that reported by Kay *et al.* [92] for the frequency of HWSS event occurrences at multiple wind farm sites.

4.2.3 Event-Based Metrics for the Assessment of the Forecasting Skill

Forecasting models are generally assessed using contingency tables which showcase the number of hits,

misses, false alarms, and correct negatives predicted by the model [93]. This is primarily of use for binary event sequences. The assessment of event-based forecasting models, however, requires an assessment of the predictive skill of the model for non-binary events over a continuous timeline.

The following metrics are defined for this application:

- The percentage forecasting error, F_1, for the maximum number of turbines exceeding the threshold wind speed for an event, given by $\widehat{N_t^m}$.
- The percentage forecasting error, F_2, for the cumulative number of turbines exceeding the threshold wind speed for an event.

The percentage forecasting error $F_1(k)$, for the k^{th} event is determined according to the relationship

$$F_1(k) = 100 * \left[\frac{\widehat{N_t^m}(k) - \widehat{N_t^f}(k)}{\widehat{N_t^m}(k)}\right], \tag{4.4}$$

where $\widehat{N_t^f}$ represents the maximum number of predicted turbines for event k.

It is possible that a model accurately predicts the maximum number of turbines exceeding a threshold wind speed for an event from (4.4), yet fails to provide an accurate estimation of the remainder of the event profile. Consequently, measured and predicted event profiles are further compared by summing the number of turbines exceeding the threshold for each event. This is mathematically described as

$$F_2(k) = 100 * \left[\frac{\sum_{t_k^s}^{t_k^e}\left(N_t^m(t_i) - N_t^f(t_i)\right)}{\sum_{t_k^s}^{t_k^e}\left(N_t^m(t_i)\right)}\right], \tag{4.5}$$

where $N_t^m(t_i)$ and $N_t^f(t_i)$ denote the measured and predicted number of turbines exceeding the wind speed threshold for the i^{th} sampling interval.

Both of the metrics defined in (4.4) and (4.5) represent forecasting errors for individual events. The forecasting errors for the individual events must subsequently be translated into a measure of forecasting skill for all events over the entire study period. Figure 34 displays an example of the typical forecasting error spread for all events at a wind farm over time. The forecasting error ranges from $-\infty$ for over-predicted forecasts and small measured events, to a 0 % error for a forecast with a 100 % accuracy, to a 100 % error where no event is forecast, yet one is measured. The results demonstrate the problematic nature of a simple error metric for this application, namely that a very large percentage forecasting error can be recorded, but may apply for a very low number of turbines, which is representative of a relatively unimportant case in practice.

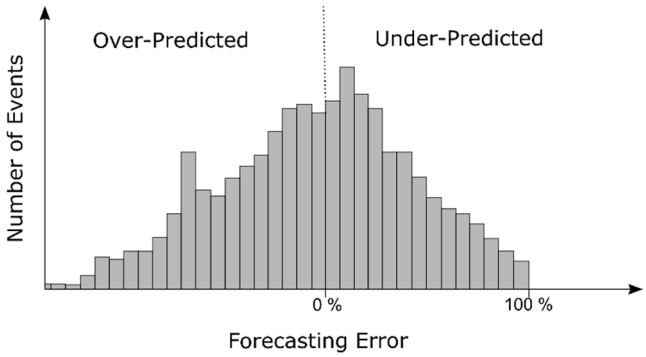

Figure 34. Number of events versus forecasting errors for events range from –∞ for over-predicted forecasts with small measured values, to 0 % for a forecast with an accuracy of 100 %, to 100 % for a missed event.

Apart from the forecasting errors for detected events, false alarms and missed events are defined as

$$N^{FA}(k) = \begin{cases} 0, & \widehat{N_t^m}(k) = 0 \text{ and } \widehat{N_t^f}(k) = 0 \\ 1, & \widehat{N_t^m}(k) = 0 \text{ and } \widehat{N_t^f}(k) > 0 \end{cases}, \tag{4.6}$$

and

$$N^{ME}(k) = \begin{cases} 0, & \widehat{N_t^f}(k) = 0 \text{ and } \widehat{N_t^m}(k) = 0 \\ 1, & \widehat{N_t^f}(k) = 0 \text{ and } \widehat{N_t^m}(k) > 0 \end{cases}, \tag{4.7}$$

where N^{FA} and N^{ME} denotes the number of false alarms, and the number of missed events respectively. From the relations above, a false alarm is declared when an event is forecast, yet none is measured for the k^{th} event. Missed events are, by contrast, declared where events are measured and not forecast for the k^{th} event. The maximum number of turbines exceeding the wind speed threshold for each event is used in the definitions.

4.3 Artificial Neural Network Model

4.3.1 Overview

ANNs have been utilised extensively in wind power forecasting owing to their ability to detect complex, non-linear relationships between the predictor and predictand. The use of ANN models reported in literature, however, focuses predominantly on the estimation of aggregated wind farm power [94], [95]. The use of ANNs in modelling wind speeds at multiple locations for wind farm applications has received limited attention.

Castellani *et al.* [65] compared the use of an ANN and an ANN-Computational Fluid Dynamics (CFD) model for wind farm power forecasting. For the ANN-CFD application, the ANN model is utilised to transfer a meso-scale forecast to a reference point. A CFD model is subsequently used to estimate the wind speed at every turbine location from the forecast at the reference location. Turbine power curves are used to convert wind speed to power at every turbine, and the wind farm power is calculated. Statistics are reported for the total wind farm power, but not the individual turbine forecasts. The study

highlights challenges in resembling the local wind flow conditions at the complex site under test using CFD modelling. It is concluded, nevertheless, that the ANN-CFD model is superior at the higher energy levels, while the ANN model performs better at the mid-energy levels.

Mana *et al.* [96] compared an ANN and ANN-CFD approach for short-term forecasting of wind farm power for a wind farm in complex terrain, using a Numerical Weather Prediction (NWP) model to provide the input forecast. Although the two methods result in a different performance from hour to hour, the average performance over the study period of seven months is found to be similar. The ANN-CFD method is shown to perform better for the variable oscillations in wind power due to the ability of the CFD to model the wind flow acceleration at the site. The study found that the ANN model is superior at the mid-energy levels and that the ANN-CFD performs better at the low and high energy levels. The investigation, furthermore, showed that the ANN method is able to detect cut-out events, whereas the ANN-CFD approach does not. This observation is inferred from the decreasing wind farm power for high wind speeds.

The findings reported for the above investigations suggest that the CFD model performs better than the ANN model for high wind speeds. It is noted, however, that the ANN model is capable of detecting HWSS events. The CFD model, furthermore, presents challenges in the modelling of local wind flow conditions for complex sites.

4.3.2 Model Topology

Figure 35 shows a simplified flow diagram of the ANN model proposed for the forecasting of HWSS events. The model is trained with an input parameter set to forecast the number of turbines in HWSS mode directly. This method essentially represents a transfer function between a meso-scale forecast and the number of turbines in HWSS mode. The HWSS event model is utilised to transform the measured nacelle wind speeds, V^{m}, into a number of turbines, N_t, exceeding the threshold wind speed, v^{th}. The number of turbines exceeding the threshold wind speed is used as a supervised target in the training of the ANN model. The ANN model is trained on all of the preceding months of the supervised target dataset, 30 % of which was randomly selected for validation data. The input parameter set is subsequently passed into the optimised ANN model to produce a number of turbines in HWSS mode.

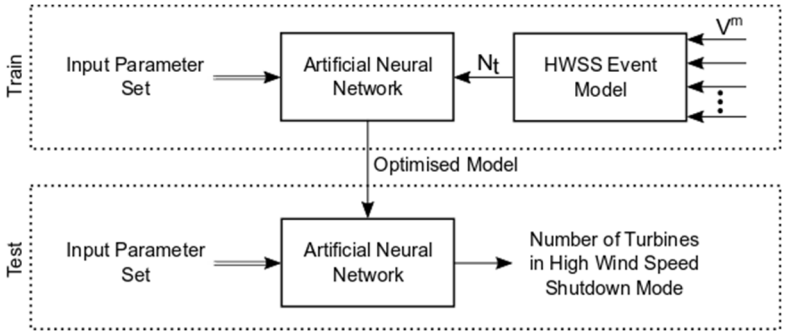

Figure 35. Flow diagram of the proposed artificial neural network model for HWSS event forecasting.

Various combinations of input parameters are applied to the ANN model with the view to determine the most suitable input for the forecasting of wind speed events. Table 11 lists the input parameters which are considered for selection as an input parameter set. Results are, however, only presented for the cases that offer the best performance.

Table 11. Permutations considered for the ANN model input parameter sets.

		Input Parameter Set								
	Case 1	**Case 2**	**Case 3**	**Case 4**	**Case 5**	**Case 6**	**Case 7**	**Case 8**	**Case 9**	**Case 10**
Wind farm mean wind speed $\bar{V}^m$	✓									
WRF ensemble wind speed forecasts, V^f		✓					✓	✓	✓	✓
A synthesised forecast derived from the WRF ensemble using MVPT			✓							
A synthesised forecast derived from the WRF ensemble using an ANN model				✓	✓	✓				
Temperature, T						✓	✓			✓
Pressure, P								✓		✓
Wind Direction, WD					✓				✓	✓

An ANN model is trained to translate a meso-scale wind speed forecast to the number of turbines exceeding the wind speed threshold at the i^{th} sampling interval in time, t_i. This model essentially represents a site-specific spatial wind speed distribution model, as the translation is dependent on spatial wind farm dynamics. Figure 36 shows the architecture of the ANN model proposed for the forecasting of the number of turbines exceeding the threshold wind speed. The hyper-parameters for the ANN model are derived using a sensitivity analysis to determine the model configuration which achieves the best forecasting results. The input layer receives the input parameter set, and applies a linear activation function. The number of neurons for this layer is dependent on the input parameter set. Three hidden layers are utilised with 20, 80, and 150 neurons respectively. Rectified linear unit activation functions are selected for the hidden layers. The output layer consists of a singular neuron, with a linear activation function, to represent the forecast of the number of turbines in the event condition, $N_t^f(t_i)$, for the i^{th} sampling interval. Adam, an extension of the stochastic gradient descent algorithm, with a mean square error loss function, is used for the model optimisation.

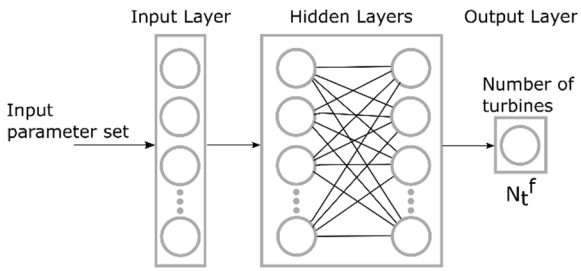

Figure 36. Artificial neural network model architecture proposed for the forecasting of the number of turbines exceeding the threshold wind speed.

4.3.3 Performance Evaluation and Case Study Results

4.3.3.1 Overview

A performance evaluation is undertaken to demonstrate the ANN model's ability to translate a meso-scale wind speed into a number of turbines in HWSS mode. Following this, two case studies are shown using the input parameter sets which yield the best results for the forecasting of frequent and infrequent events.

4.3.3.2 Performance Evaluation of the Artificial Neural Network Model for Event Prediction

In order to assess the ability of the proposed ANN model to predict the number of turbines exceeding a wind speed threshold at any given sampling interval, the ANN model is trained and tested using the input parameter set defined as case 1 in Table 11. This study investigates the ability of the ANN model to encode the transfer function between an accurate site-specific mean wind speed and the number of turbines exceeding a threshold.

The forecasting errors acquired from the defined metrics in (4.4) and (4.5) are analysed through the visual inspection of heat maps. Figure 37 displays the heat map of the forecasting error versus the measured percentage of turbines exceeding the threshold wind speed for frequent and infrequent events. The percentage of turbines exceeding the threshold wind speed is a measure of the maximum percentage of turbines in the wind farm exceeding the threshold wind speed for the event. This is effectively a measure of the event size in relation to the wind farm capacity. The forecasting error for each of the events measured over the duration of the study period is denoted with an x, and is overlaid on a heat map which expresses the density of events.

The forecasting error heat maps, for both frequent and infrequent events, demonstrate that the model improves in forecasting accuracy with an increasing percentage of turbines exceeding the threshold value. The results show that the model accuracy for small events, when fewer than 20 % of the turbines exceed the threshold wind speed, is predominantly between 50 to 100 % under-predicted. The results, furthermore, demonstrate that the model is more suited to the forecasting of the maximum number of turbines exceeding the threshold wind speed for frequent and infrequent events.

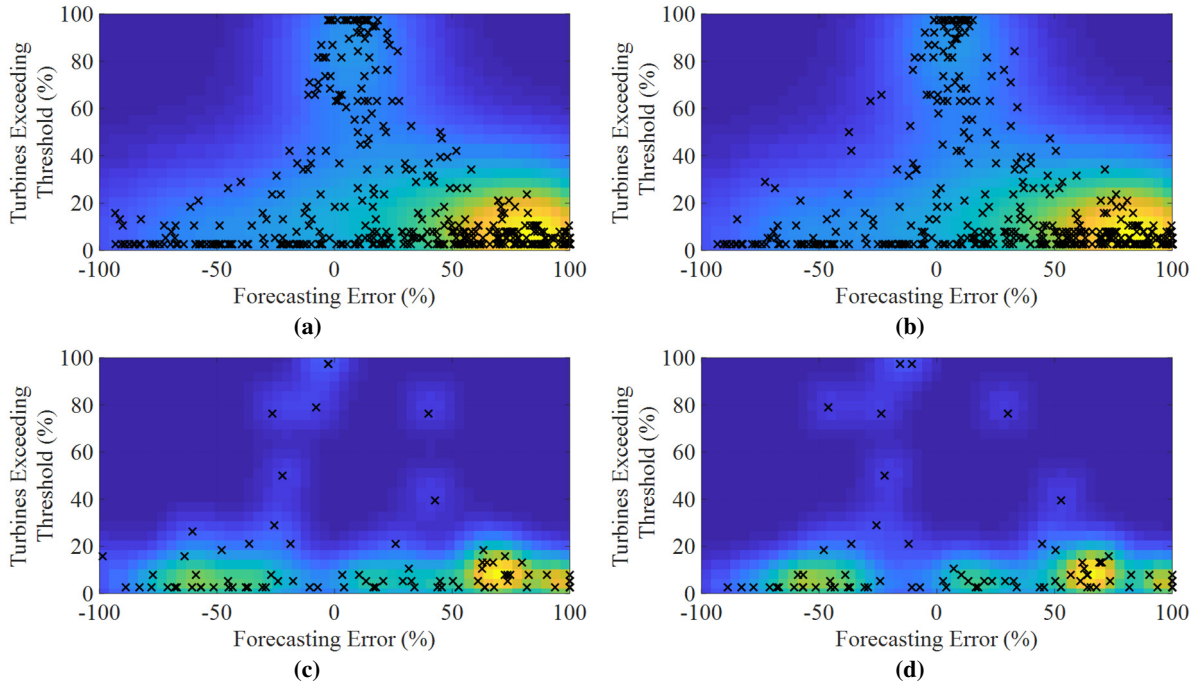

Figure 37. Event forecasting error versus the percentage of turbines exceeding the threshold wind speed: (a) Maximum number of turbines exceeding the threshold wind speed for frequent events and (c) infrequent events and (b) cumulative number of turbines exceeding the threshold wind speed for an event for frequent events and (d) infrequent events.

Figure 38 shows the number of false alarms raised by the model as a function of the percentage of turbines exceeding the threshold wind speed. Although a large number of false alarms are raised, they are only prevalent when less than 10 % of the turbines exceed the threshold wind speed.

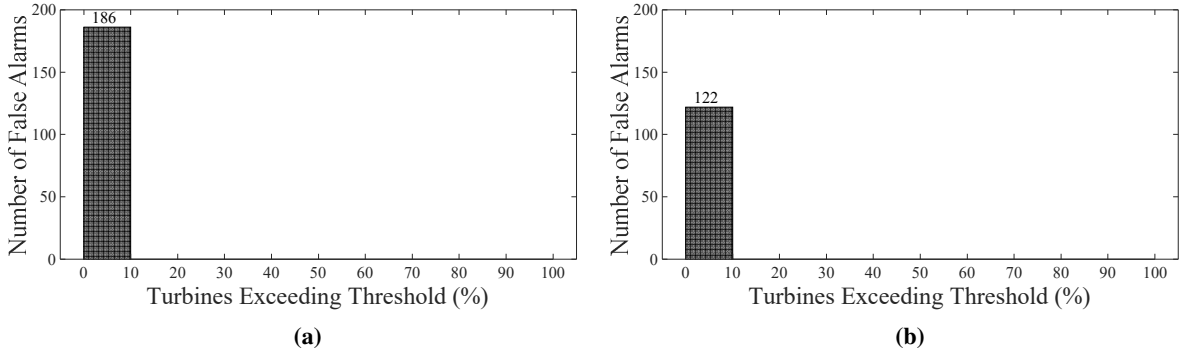

Figure 38. Number of false alarms versus the percentage of turbines exceeding the wind speed threshold: (a) frequent events and (b) infrequent events.

Figure 39 shows the numbers of missed and the total number of events as a function of the percentage of turbines exceeding the wind speed threshold. The only events that are not detected by the forecast model are associated with small events, where less than 10 % of the turbines were measured exceeding the threshold wind speed.

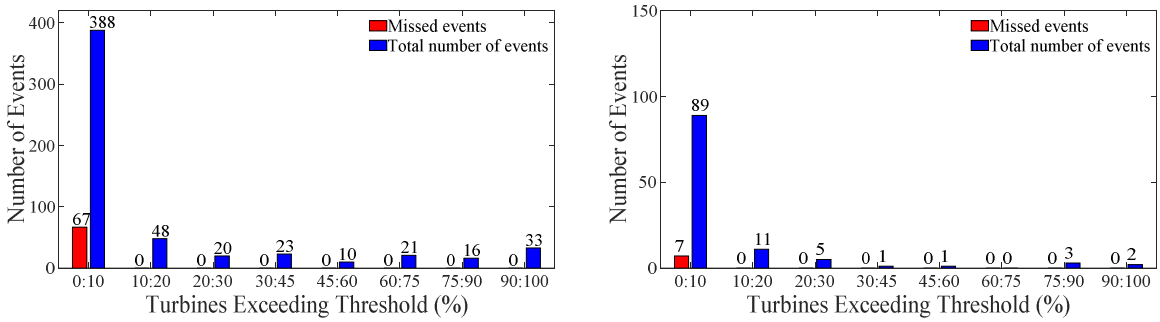

Figure 39. Numbers of missed events and the total number of events versus the percentage of turbines exceeding the wind speed threshold: (a) frequent events and (b) infrequent events.

The results demonstrate that the model is adept at translating a meso-scale wind speed to a number of turbines exceeding a wind speed threshold. The ANN model is employed as a wind speed event forecasting model in the following section by selecting an input parameter set containing forecast data.

4.3.3.3 Case Study Results for the Forecasting of Frequent and Infrequent Events

The ANN model is evaluated for its ability to forecast frequent events with a threshold wind speed of 12 ms^{-1}. Results are presented only for the input parameter set which yields the best performance, which in this instance is defined by case 9 in Table 11, i.e. the cold-start WRF ensemble with wind direction included as an additional environmental variable.

Figure 40 shows the forecasting error for frequent events using the metrics defined in (4.4) and (4.5) versus the measured percentage of turbines exceeding the threshold wind speed. The presented results leads to the following observations:

- The forecasting skill of the model increases with an increasing percentage of turbines exceeding the threshold wind speed.
- The model tends to under-predict events for both metrics.
- The model is more adept at detecting the maximum number of turbines exceeding the threshold wind speed of frequent events with a larger percentage of events within the 0 to 50 % forecasting error range.
- The forecasting error for both metrics shows that the model accuracy is lower for small events with forecasting errors predominantly ranging from 30 to 100 % for less than 20 % of the turbines exceeding the wind speed threshold.

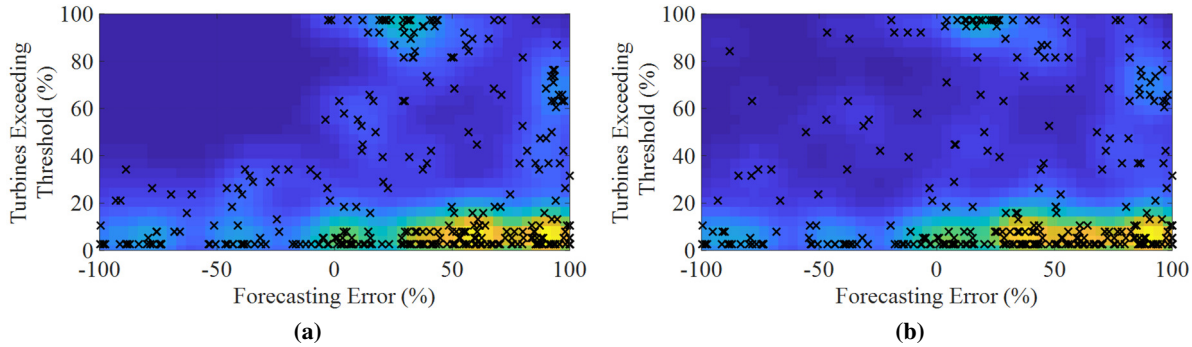

Figure 40. Event forecasting error versus the percentage of turbines exceeding the threshold wind speed for frequent events: (a) Maximum number of turbines exceeding the threshold wind speed and (b) the cumulative number of turbines exceeding the threshold wind speed for an event.

Figure 41 shows the number of false alarms, as well as the total number and number of missed events for the forecast of frequent events at the wind farm as a function of the percentage of turbines exceeding the threshold wind speed of 12 ms^{-1}. A large number of false alarms are raised for small events with less than 10 % of the turbines exceeding the threshold wind speed. This is to be expected due to the variable nature of the wind and complexity of the forecast. The model has, however, detected most of the events, with only 11 missed events out of a total of 659 measured events. The results demonstrate that the formulated ANN model is capable of utilising a meso-scale wind speed forecast as an input parameter to forecast frequent events at a wind farm.

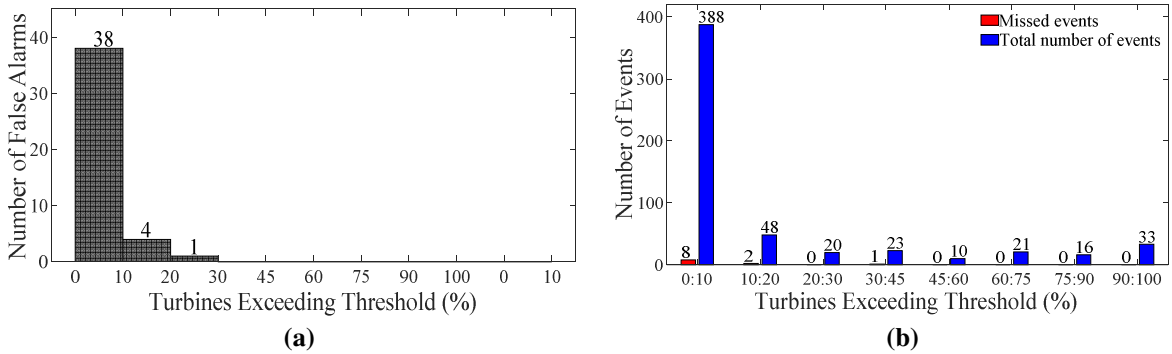

Figure 41. Frequent event forecast: (a) Number of false alarms and (b) total number and number of missed events versus the percentage of turbines exceeding the threshold wind speed.

The forecasting of infrequent events, i.e. 18 ms^{-1} threshold, is complicated by the degrading accuracy of the WRF ensemble forecast for increasing wind speeds, as well as by the sparseness of events with which to train the ANN model. The relatively poor accuracy of the WRF model at higher wind speeds is therefore improved using an intermediary ANN model. The WRF ensemble is synthesised into a singular, more accurate, forecast using an ANN model comprising nine neurons in the input layer, two hidden layers consisting of 20 and 80 neurons respectively, and one neuron in the output layer. A sigmoid compression function is used to normalise the wind speeds, and to focus on the wind speed range of interest. In doing so, low wind speeds are omitted, and do not contribute to the training of the model, resulting in an ANN model geared towards the estimation of wind speeds in a selected band.

The two-parameter sigmoid function is mathematically described as follows:

$$S(x) = \frac{1}{1+ e^{-k(x- x_0)}}, \tag{4.8}$$

where k and x_0 denote the slope and position parameters respectively. Figure 42 shows the sigmoid compression function utilised in the model. Slope and position values of 0.7 and 12 respectively were determined through a sensitivity analysis to return the lowest error for the high wind speed range of the validation set.

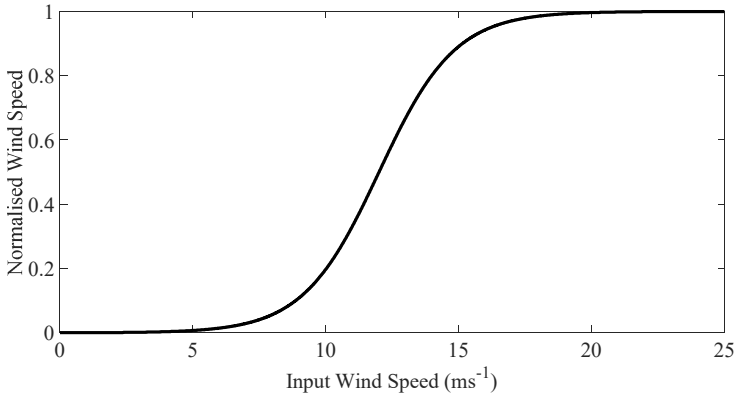

Figure 42. Sigmoid compression function used to optimise the high wind speed range.

The utilisation of the WRF model ensemble forecasts for the input parameter set for training biases the model with prior forecasting errors due to the low number of events for this threshold wind speed. The ANN model is, consequently, trained with the input parameter set denoted case 1 in Table 11, i.e. the mean wind farm wind speed, $\overline{V}^m$, and tested with the input parameter set described by case 4, i.e. the synthesised meso-scale forecast derived from the WRF ensemble model using an intermediary ANN model.

Figure 43 shows the error for infrequent event forecasts using the metrics defined in (4.4) and (4.5) versus the measured percentage of turbines exceeding the threshold wind speed. The presented results lead to the following observations regarding the forecasting skill of the ANN model:

- The model skill increases with an increasing percentage of turbines exceeding the threshold wind speed.
- The model's estimation of the maximum number of turbines exceeding the threshold wind speed for an event is more accurate than its prediction of the cumulative number of turbines exceeding the threshold wind speed for an event.
- The majority of events exhibit large under-predictive forecasting errors when fewer than 20 % of the turbines are exceeding the threshold wind speed.

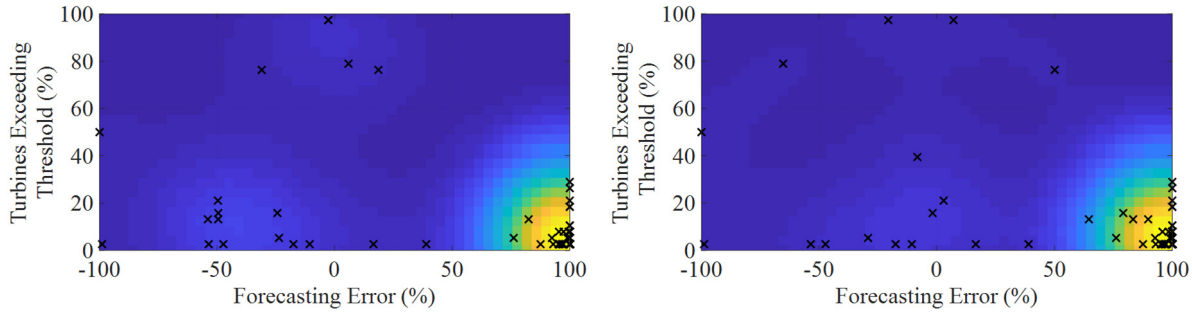

Figure 43. Event forecasting error versus the percentage of turbines exceeding the threshold wind speed for infrequent events: (a) Maximum number of turbines exceeding the threshold wind speed for an event and (b) the cumulative number of turbines exceeding the threshold wind speed for an event.

Figure 44 displays the number of false alarms, as well as the total number and number of missed events for the forecast of infrequent events at the wind farm as a function of the percentage of turbines exceeding the threshold wind speed of 18 ms^{-1}. The results show a relative increase in missed events when compared to the results for the forecast of frequent events. The model has detected all events when more than 30 % of the turbines are exceeding the threshold wind speed. A large number of false alarms are produced by the ANN model. False Alarms are raised 17 times for events where between 90 % and 100 % of turbines are forecast to be exceeding the threshold wind speed of 18 ms^{-1}. The increase in false alarms is potentially due to the under-forecasting errors in the training set which has resulted in an over-correction by the ANN model.

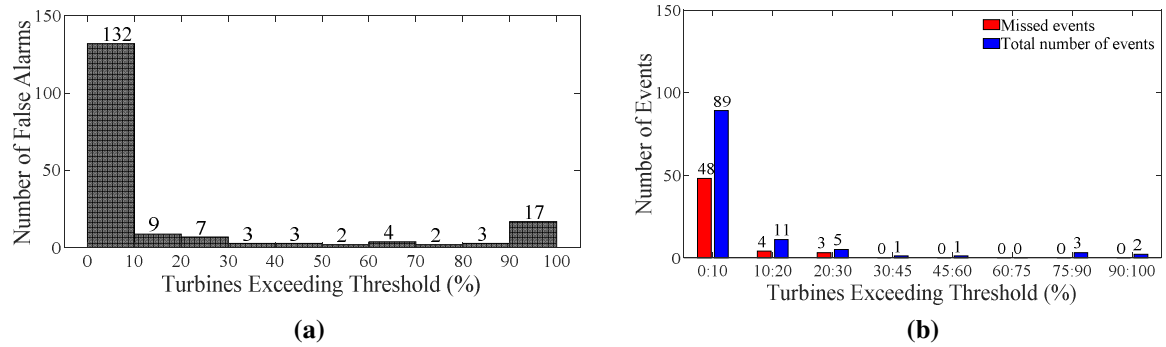

Figure 44. Infrequent event forecast: (a) Number of false alarms and (b) total number and number of missed events versus the percentage of turbines exceeding the threshold wind speed.

4.4 Statistical Downscaling Model

4.4.1 Overview

A novel statistical downscaling model is proposed as an alternative approach to the ANN model. Figure 45 shows a flow diagram proposed for HWSS event forecasting using the statistical downscaling model developed in Chapter 3. In this technique, an input parameter set, consisting of a meso-scale wind speed and a wind direction forecast, is translated into individual turbine wind speeds. The turbine wind speeds are subsequently converted into a number of turbines in HWSS mode using the HWSS event model.

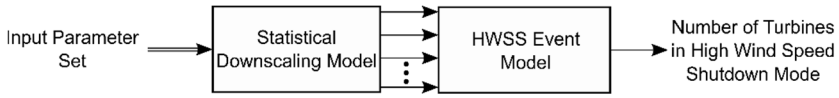

Figure 45. Flow diagram of the proposed HWSS event forecasting model using the statistical downscaling model.

Various model topologies are tested in order to determine the input parameter set and training sequence which yields the most accurate forecast of wind speed events. Only the best-performing models are reported in the following sections.

4.4.2 Model Topology

The statistical downscaling model requires a meso-scale wind speed, as well as a wind direction forecast, as an input. Table 12 lists the input parameter sets considered in this investigation, however, results are only presented for the cases that offer the best performance.

Table 12. Permutations considered for the statistical downscaling model input parameter sets.

	Input Parameter Set		
	Case 1	**Case 2**	**Case 3**
Measured mean wind farm wind speed, $\bar{V}^m$	✓		
A synthesised WRF ensemble using MVPT		✓	
A synthesised WRF ensemble using an ANN model			✓
A wind direction forecast, D	✓	✓	✓

Various loss functions are tested for the synthesised WRF ensemble forecast using an ANN model. The WRF ensemble is synthesised into a single meso-scale forecast in Chapter 2 using a mean-squared error loss function. This is mathematically described as

$$\text{Loss} = \frac{1}{N_i}\sum_{i=1}^{N_i}(e_i{}^2)\,. \tag{4.9}$$

This loss function penalises the large errors irrespective of the magnitude of the wind speed which results in a forecast with a minimised error for the entire operating range of wind speeds.

Figure 16 displays the MAE of the wind speed forecast error versus mean wind speed of the wind farm. It is evident that the degrading forecasting accuracy will impact on the quality of high wind speed event forecasts. In order to improve the forecast for high wind speeds, alternative loss functions are derived for the ANN model which are designed to penalise errors at high wind speeds more than errors at low wind speeds.

A linearly-weighted and an exponential loss function are defined by

$$\text{Loss} = \sum_{i=1}^{N_i}\left(|e_i| \cdot \bar{v}_i^m\right), \tag{4.10}$$

and

$$\text{Loss} = \sum_{i=1}^{N_i}\left(|e_i| \cdot \exp^{(\propto \cdot \bar{v}_i^m)}\right), \tag{4.11}$$

where $\propto$ denotes a weighting factor which controls the rate of exponential increase affecting the magnitude of the penalty for high wind speeds. Minimisation of the custom loss functions in (4.10) and (4.11) will ensure that the higher wind speed errors are reduced in the training of the ANN model.

4.4.3 Performance Evaluation and Case Study Results

4.4.3.1 Overview

A performance evaluation is undertaken to demonstrate the statistical downscaling model's ability to translate a meso-scale wind speed into a number of turbines in HWSS mode. Following this, case studies are shown with the input parameter sets which yield the best results for the forecasting of frequent and infrequent events.

4.4.3.2 Evaluation of the Downscaling Model for the Prediction of Turbine Events

The statistical downscaling model's ability to predict the number of turbines exceeding the threshold wind speed is evaluated in this section. Figure 46 displays a simplified flow diagram of the model topology. Case 1 from Table 12 is utilised as the input parameter set, which is interleaved without replacement for the training and testing sets. This results in half of the data selected for training, 30 % of which is used for model validation, and half for testing of the model. It is recognised that this sequence is not representative of a scenario which could be implemented in practice, and is undertaken with the sole purpose of evaluating the model without the bias inherent in the dataset. It is furthermore necessary to adopt this approach due to the small dataset available. The downscaling model is trained with the measured nacelle turbine wind speeds, V^m, as the supervised target, and the training parameters are preserved for the testing of the model. Turbine wind speeds, V^t, are generated by the optimised statistical downscaling model. An event model converts the predicted turbine wind speeds into a forecast for the number of turbine events, given by N_t^f.

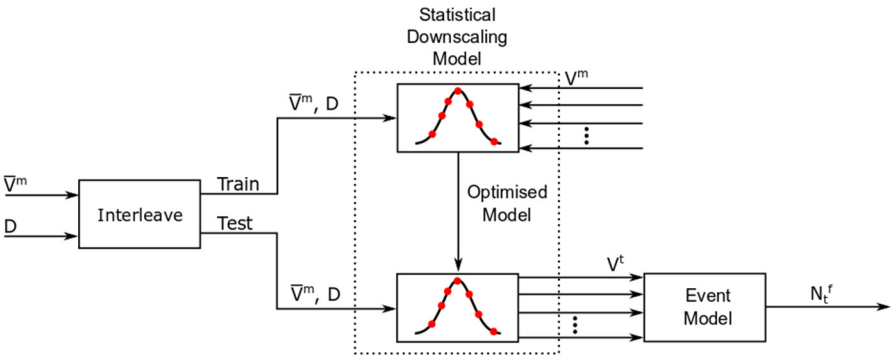

Figure 46. Simplified flow diagram of the procedure used to test the statistical downscaling model's ability to forecast wind speed events.

The MAE is calculated for the error in the test dataset between the set of predicted wind speeds, V^t, and the set of measured wind speeds, V^m, for each turbine in the wind farm. Figure 47 shows a boxplot

which represents the MAE for all of the individual turbines as a function of the mean wind speed of the wind farm. It is shown that the while the range of the MAE increases with increasing wind speed, the median of the turbine MAE does not increase consistently with increasing wind speed. The results demonstrate that the model is capable of downscaling the meso-scale wind speed to individual turbine wind speeds with good accuracy.

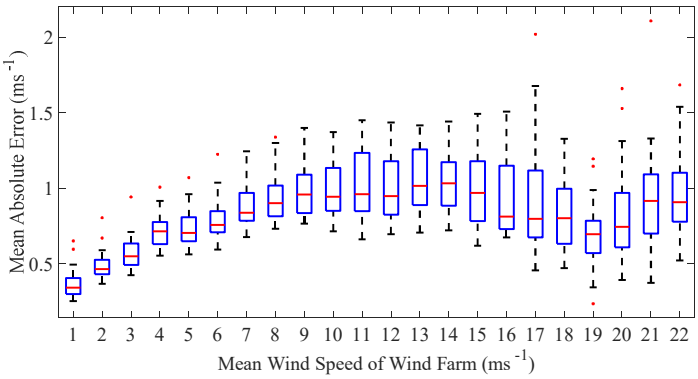

Figure 47. Boxplot representing the MAE for all of the individual turbines as a function of the mean wind speed of the wind farm.

Figure 48 displays the estimation errors returned by (4.4) and (4.5) for all events versus the measured percentage of turbines exceeding the threshold wind speed for frequent and infrequent event predictions.

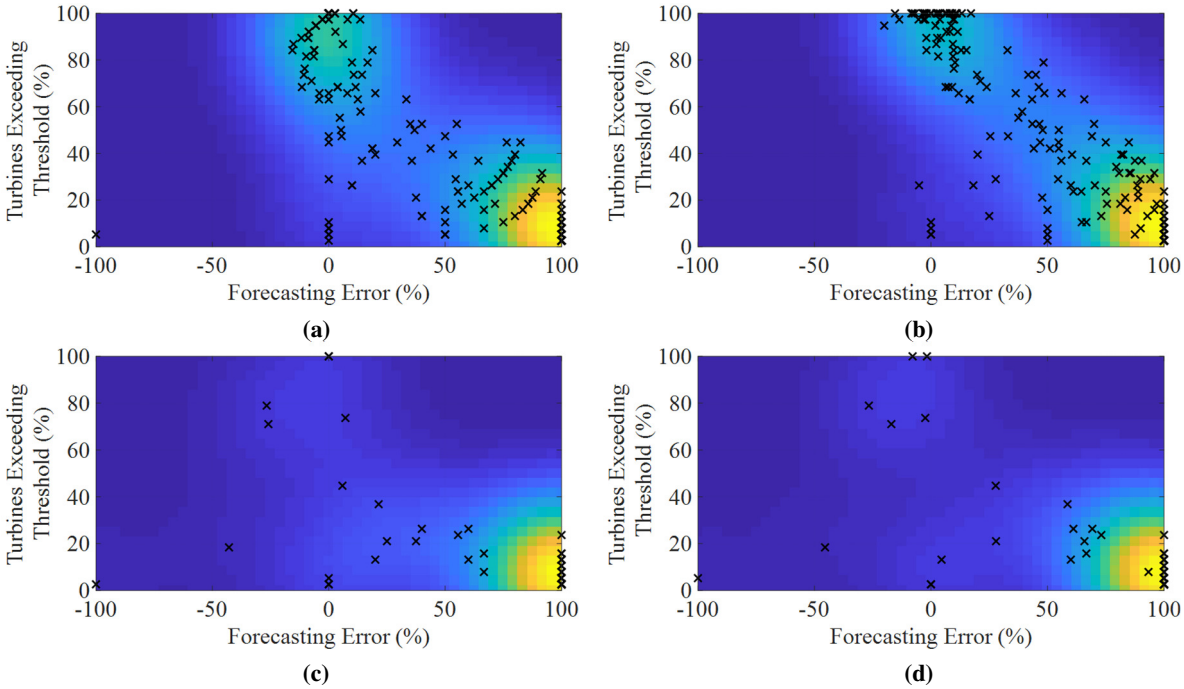

Figure 48. Event estimation error versus the percentage of turbines exceeding the threshold wind speed: (a) Maximum number of turbines exceeding the threshold wind speed for frequent events and (c) infrequent events and (b) the cumulative number of turbines exceeding the threshold for an event for frequent events and (d) infrequent events.

The results show that the estimation error for the statistical downscaling model improves for an increasing percentage of turbines exceeding the threshold wind speed. The estimation for the maximum

number of turbines exceeding the threshold wind speed is marginally superior to that of the cumulative number of turbines exceeding the threshold wind speed. Both forecasting metrics return a positive error, which indicates a tendency of the model to under-predict the defined events. The majority of events exhibit large under-predictive errors when fewer than 20 % of the turbines are exceeding the threshold wind speed.

Figure 49 displays the number of false alarms for frequent and infrequent events, as a function of the percentage of turbines exceeding the threshold wind speed. Only 1 and 2 false alarms have been raised by the statistical downscaling model, whereas the ANN model predicted 186 and 122, for the 12 ms^{-1} and 18 ms^{-1} thresholds respectively. This large reduction in false alarms is highly desirable as events forecast by the model are by corollary more certain to occur.

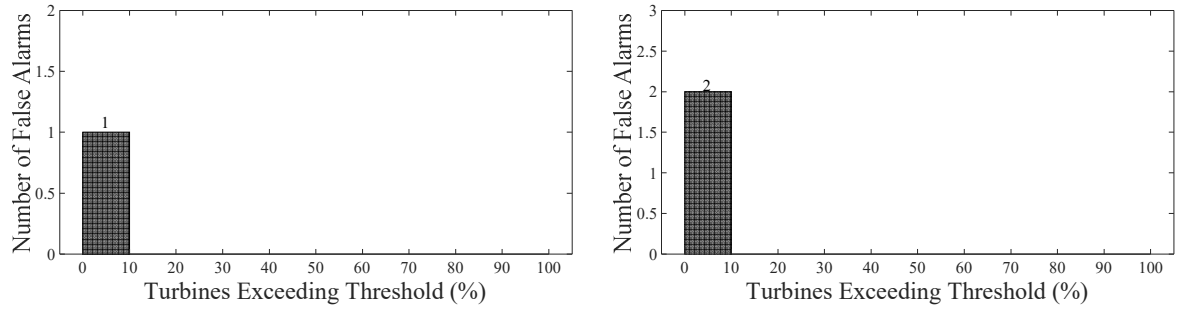

Figure 49. Number of false alarms versus the percentage of turbines exceeding the threshold wind speed: (a) Frequent events and (b) infrequent events.

Figure 50 shows the total number and number of missed events for frequent and infrequent events as a function of the percentage of turbines exceeding the threshold wind speed. There is a proportionate increase in missed events when compared to the ANN model. This is, however, only for small events where fewer than 30 % of the turbines are in exceedance of the wind speed threshold.

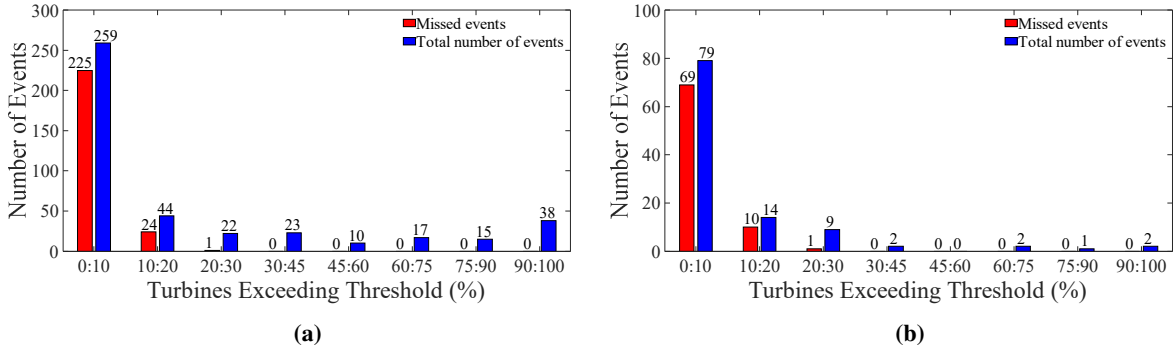

Figure 50. Number of missed events versus the percentage of turbines exceeding the threshold wind speed for (a) 12 ms^{-1} and (b) 18 ms^{-1}.

The results demonstrate that the proposed model is capable of meso to micro-scale downscaling for event prediction of turbine level events associated with mid-range and high wind speeds. Although the ANN model provides a superior prediction for mid-range wind speeds, the statistical downscaling

model produces a marginally superior prediction for high wind speeds with the benefit of producing fewer false alarms.

4.4.3.3 Case Study Results for the Forecasting of Frequent and Infrequent Events

Figure 51 shows a flow diagram of the procedure used to forecast wind speed events using the proposed statistical downscaling model. The model is trained using the same model topology as for the model evaluation in Figure 46. The statistical downscaling model's input parameter for the testing set is amended to the input parameter set listed as case 3 in Table 12. The wind speed forecast, V^f, is derived using an ANN model which is optimised for the synthesis of ensemble wind speeds using the methodology described in Chapter 2. The proposed model is further evaluated with the loss functions defined in (4.9) to (4.11) in order to tune the synthesised meso-scale forecast, V^{fs}, for improved performance at high wind speeds.

The downscaling model outputs a set of wind speeds which is statistically representative of the turbine wind speeds, V^t. An event model converts the turbine wind speeds into a forecast for the number of wind turbines in exceedance of a threshold wind speed, N_t^f.

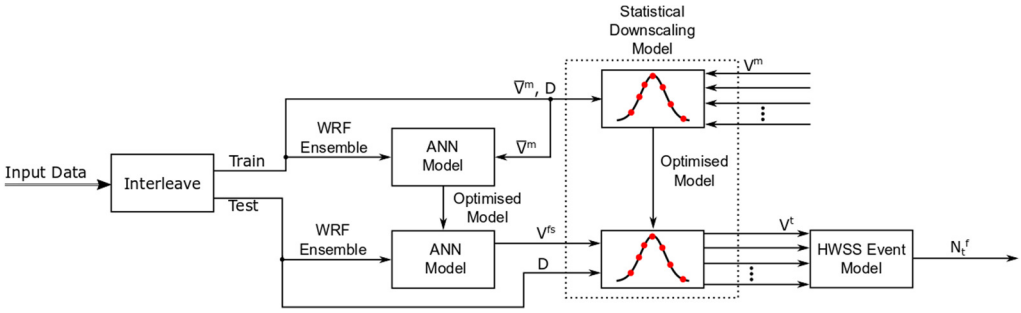

Figure 51. Flow diagram of the procedure used to forecast wind speed events using the proposed statistical downscaling model.

A synthesised wind speed forecast, V^{fs}, is derived using an ANN model with a mean-squared error loss function given by (4.9). Figure 52 shows a boxplot which represents the MAE for all of the individual turbines as a function of the mean wind speed of the wind farm. As demonstrated in Chapter 2, the MAE of the forecast increases with increasing wind speed. The MAE is at the maximum value for the high range wind speed of interest, i.e. 18 ms^{-1}.

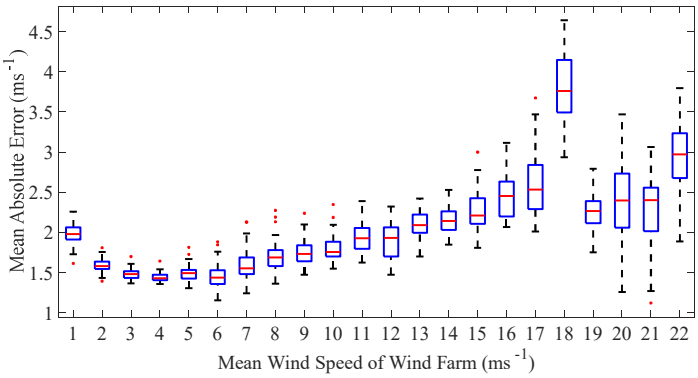

Figure 52. Boxplot representing the MAE for all of the individual turbines as a function of the mean wind speed of the wind farm. The ensemble forecast is synthesised using an ANN model with a mean-squared error loss function.

Figure 53 displays the total number, as well as the number of missed events versus the percentage of turbines exceeding the wind speed threshold for frequent and infrequent events. The model has missed a large number of events due to the inaccurate input forecast. The results demonstrate that the synthesised ensemble forecast using an ANN model with a mean-squared error loss function is not suitable for the forecasting of mid-range or high-range wind speed events.

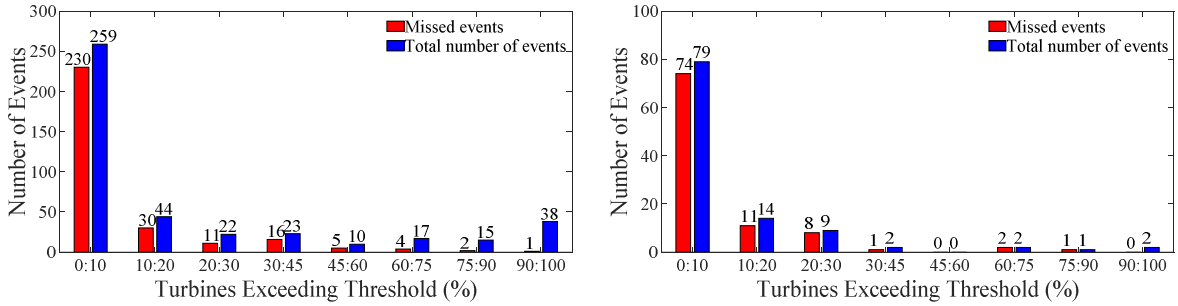

(a) **(b)**

Figure 53. Number of total and missed events versus the percentage of turbines exceeding the threshold wind speed of (a) 12 ms^{-1} and (b) 18 ms^{-1}.

Improved accuracy is targeted in the high wind speed range by amending the ANN model loss function to a linearly-weighted loss function described in (4.10). Figure 54 shows a boxplot which represents the MAE for all of the individual turbines as a function of the mean wind speed of the wind farm. The use of a linearly-weighted loss function has reduced the MAE of the predicted turbine wind speeds for the high wind speed range and has increased the MAE of low wind speeds.

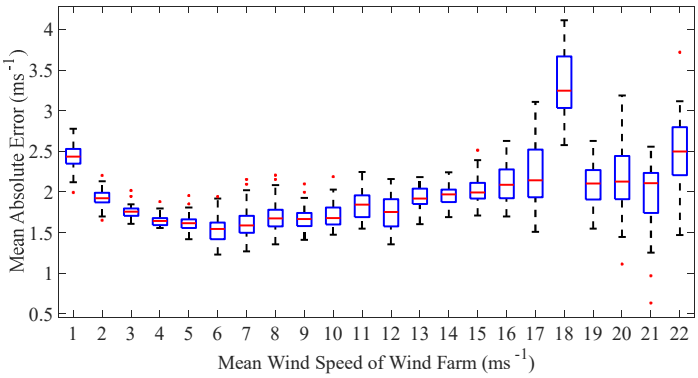

Figure 54. Boxplot representing the MAE for all of the individual turbines as a function of the mean wind speed of the wind farm. The ensemble forecast is synthesised using an ANN model with a linearly-weighted loss function.

Figure 55 shows the total number, as well as the number of missed events versus the percentage of turbines exceeding the wind speed threshold for the forecast of frequent and infrequent wind speed events. The number of missed events has reduced for the 12 ms^{-1} threshold. The number of missed events for the 18 ms^{-1} threshold, however, is similar to the results obtained using the mean-squared error loss function.

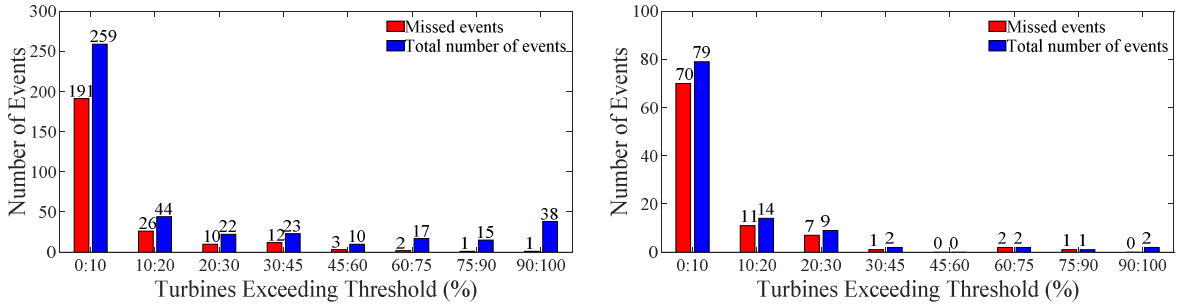

(a) **(b)**

Figure 55. Number of total and missed events versus the percentage of turbines exceeding the threshold wind speed for (a) 12 ms^{-1} and (b) 18 ms^{-1}.

An exponential loss function described in (4.11) is utilised to further reduce the forecasting error at high wind speeds. Various weighting factors are assessed through inspection of the resulting number of false alarms and missed events. It is determined through a sensitivity analysis that a weighting factor of approximately 1.5 yields the best forecasting performance for this dataset.

Figure 56 displays a boxplot which represents the MAE for all of the individual turbines as a function of the mean wind speed of the wind farm. The results show that the accuracy of the high-range wind speeds has improved when compared with the other loss functions which were assessed. The results show that the exponential weighting has prioritised the minimisation of the higher wind speed errors, as is evident by the degrading MAE with increasing wind speed.

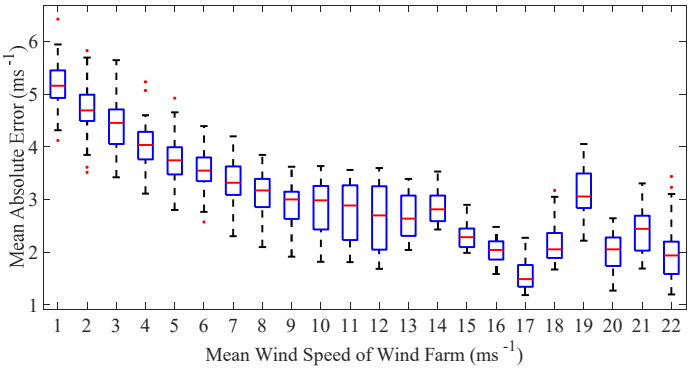

Figure 56. Boxplot representing the MAE for all of the individual turbines as a function of the mean wind speed of the wind farm. The ensemble forecast is synthesised using an exponential loss function.

Figure 57 shows the forecasting errors returned by (4.4) and (4.5) for all events versus the measured percentage of turbines exceeding the threshold wind speed for frequent and infrequent event forecasts. The results show that the forecasting error for the statistical downscaling model improves for an increasing percentage of turbines exceeding the threshold wind speed. The majority of events exhibit large under-predictive forecasting errors when fewer than 20 % of the turbines are exceeding the threshold wind speed. The forecast of the maximum number of turbines exceeding the threshold wind speed is superior to that of the cumulative number of turbines exceeding the threshold wind speed for an event. For events where greater than 70 % of the turbines exceed the threshold wind speed, the forecast error is within approximately -30 % to 30 % for the forecast of the maximum number of turbines exceeding the threshold wind speed. The use of an exponentially-weighted loss function in the intermediary ANN model for the ensemble synthesis has resulted in an under-prediction for small events, and an over-prediction for the larger events.

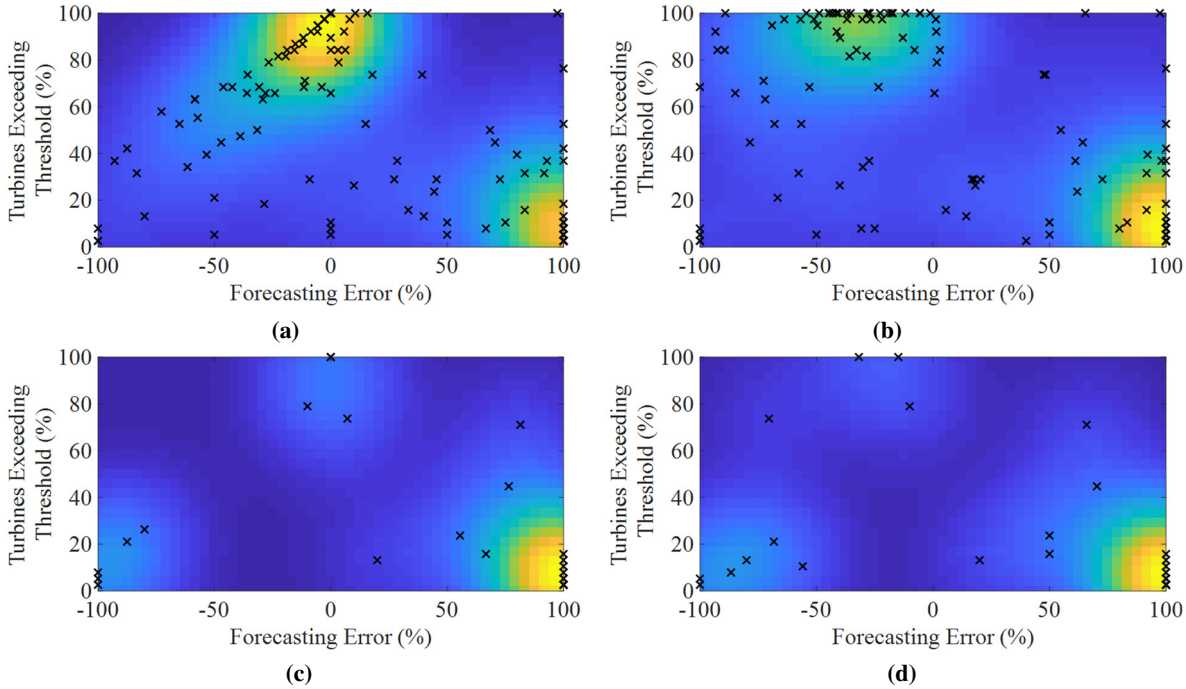

Figure 57. Event forecasting error versus the percentage of turbines exceeding the threshold wind speed:

(a) Maximum number of turbines exceeding the threshold wind speed for frequent events and (c) infrequent events and (b) the cumulative number of turbines exceeding the threshold for an event for frequent events and (d) infrequent events.

Figure 58 displays the number false alarms as well as the total number and number of missed events for the forecasting of frequent events, i.e. using a 12 ms^{-1} wind speed threshold. The use of the exponential loss function has reduced the number of missed events considerably. A large number of false alarms is raised by the forecasting model for small events.

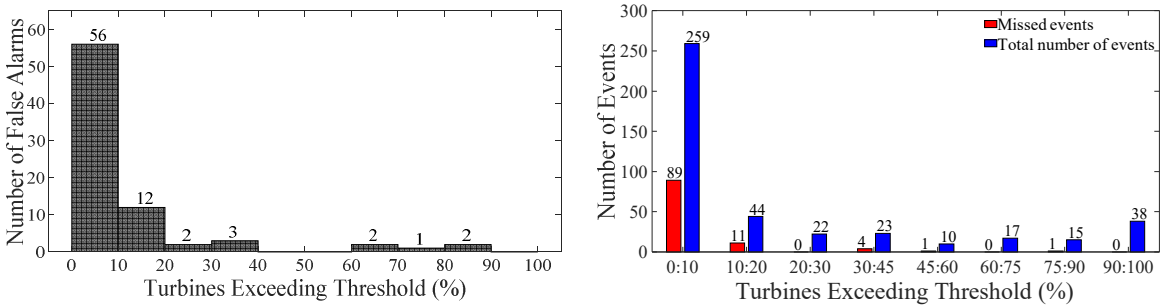

(a) **(b)**

Figure 58. Frequent event forecast: (a) Number of false alarms and (b) total number and number of missed events versus the percentage of turbines exceeding the threshold wind speed.

Figure 59 shows the number of false alarms, the total number and the number of missed events for the forecasting of infrequent events, i.e. an 18 ms^{-1} wind speed threshold. The results show a large reduction in the number of missed events when compared with the mean-squared error and linearly-weighted loss functions. The results furthermore demonstrate an improvement over the ANN model forecast for infrequent events as the number of missed events, and the number of false alarms has been reduced.

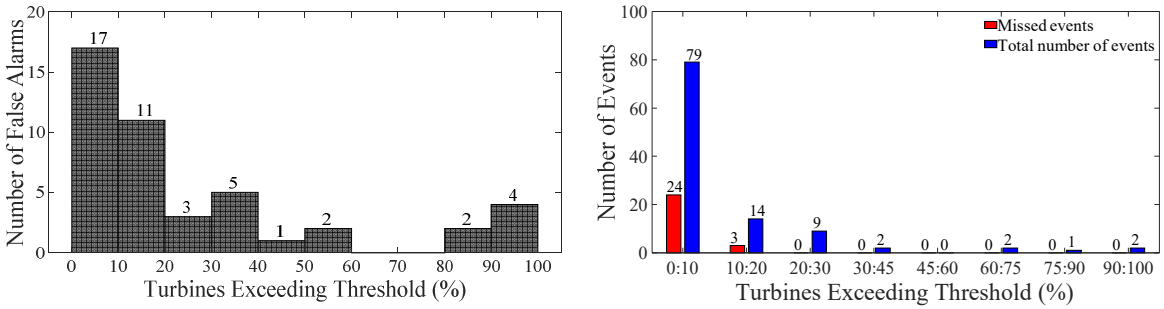

(a) **(b)**

Figure 59. Infrequent event forecast: (a) Number of false alarms and (b) total number and number of missed events versus the percentage of turbines exceeding the threshold wind speed.

4.5 Discussion and Conclusions

Two models are proposed to forecast the number of turbines exceeding a wind speed threshold for a large, utility-scale wind farm. This case is analogous to HWSS events in the sense that forecasting models must predict the number of turbines exceeding wind speed thresholds for every sampling interval. Two wind speed thresholds are defined with the view to represent both frequent and infrequent

events at the site under investigation. Frequent events are represented by a mid-range threshold of 12 ms^{-1}, while infrequent events are represented by a high range threshold of 18 ms^{-1}. The wind speed threshold of 18 ms^{-1} is selected as this represents a relatively rare high wind speed condition for the target site, in the sense that only 0.5 % of the sampled wind speeds at all turbines exceed this wind speed. Two novel approaches are demonstrated for the forecasting of wind speed events.

An ANN model is proposed which translates an input meso-scale forecast directly into a number of wind turbines exceeding the threshold wind speed. It is demonstrated that the formulated ANN model is adept at forecasting both frequent and infrequent events using an input parameter set comprising an ensemble wind speed forecast, and a wind direction forecast. The wind speed ensemble forecast is synthesised using a mean-squared error loss function. For the forecasting of infrequent events, a sigmoid compression function is utilised to limit the influence of low wind speeds in the training of the model in a bid to improve the forecasting skill at higher wind speeds. The results for this approach show that the formulated ANN model over-predicts the occurrence of events, and consequently raises a large number of false alarms. This is due to the tendency of the input forecast to under-predict the meso-scale wind speeds which further influences the ANN model in the training process.

A second approach adopts the use of the statistical downscaling technique proposed in Chapter 3 for the forecasting of wind speed events. This method requires an input meso-scale forecast which is accurate at high wind speeds. An intermediary ANN model is used to synthesise the meso-scale wind speed ensemble forecast using various loss functions. An exponentially-weighted loss function proves to be superior to the mean-squared error and the linearly-weighted loss function. This approach results in an event forecast for infrequent events which is marginally superior in skill to the ANN model, with a slight improvement in forecasting accuracy, and considerably fewer false alarms.

Chapter 5

Quantification and Comparison of Site-Specific Risk of High Wind Speed Shutdown using Meso-Scale Profiles and Survival Analysis

5.1 Overview

A considerable amount of research has been conducted into the siting of wind farms to maximise cumulative energy yield, or to minimise the aggregated variability of the generation profile, or variability of the residual load [52], [54], [60], [97], [98]. Limited research has, however, been conducted into the development of formal methodologies to quantify the frequency, severity and relative risk of the loss of generation events associated with High Wind Speed Shutdown (HWSS), especially in the context of informing wind farm siting decisions [99]. The case studies conducted to date on the impacts of HWSS generally reflect an observational rather than anticipatory approach [6], [8], [9], [15], [82]. The siting of wind farms can potentially be optimised such that the negative impacts associated with ramping and the HWSS phenomena are minimised providing that suitable, dedicated methodologies are available for site characterisation.

A novel methodology is proposed to empirically evaluate the risk of loss of generation due to HWSS events at a given site, based on its simulated, or measured, historicity. This proposed methodology aims to provide a framework with which to quantify the risk of HWSS events for individual sites, as well as for geographic regions to guide strategic and investment decisions. The model topology incorporates a spatial wind speed downscaling model, HWSS event model, and a risk assessment model based on the theory of survival analysis. The model is implemented and results are presented for two selected sites from a meso-scale reanalysis dataset. Site comparison is performed using survival models to determine the relative temporal risk of HWSS occurrence between two target sites for various HWSS event levels.

5.2 Theoretical Framework

5.2.1 Meso-Scale Wind Resource Modelling

Traditionally, the siting analyses for potential wind farms are done using historical wind resource data for the study area. Various techniques have been suggested to model the tempro-spatial wind energy resource for a given geographical area [73]- [77].

Adequate data coverage is required in order to perform an anemological-related analysis over a large region. Numerical Weather Prediction (NWP) tools have been developed for modelling wind profile data where there is a sparsity of available measurement sites. The Weather Research and Forecasting (WRF) tool developed by the Technical University of Denmark is currently the preferred method for deriving wind atlases [100].

Mathematically, the sampling times and wind speed data associated with the meso-scale wind speed profile can be represented by the sets T and V^m respectively, given by

$$T = \{ t_i, \quad i = 1, 2, 3, \dots, N_i \}, \tag{5.1}$$

$$V^m = \{ v^m(t_i) \}, \tag{5.2}$$

where t_i and $v^m(t_i)$ denote the sampling time and wind speed respectively of the i^{th} sample, and N_i denotes the number of wind speed samples.

The temporal resolution of the meso-scale wind resource dataset used in this investigation is 15 minutes. This is representative of the data contained in wind resource atlases and the forecast sampling intervals that are practical for WRF simulations. The definition of HWSS events is therefore based on the mean wind speed for a 15 minute sampling interval. High frequency dynamic phenomena, such as turbine responses to wind gusts, are thereby neglected.

5.2.2 Micro-Scale Wind Speed Modelling

For some applications, meso-scale models do not offer a satisfactory representation of the wind resource. Forecasting for wind farm applications, for instance, requires increased horizontal resolution for an adequate characterisation of terrain effects, unless the wind farm is situated in simple, flat terrain [83]. Micro-scale models are therefore utilised to downscale meso-scale models for improved wind speed estimation. The modelling and forecasting of turbine-specific behaviour such as HWSS phenomena, in particular, requires accurate micro-scale wind speed profiles defined at the turbine level.

A variety of techniques have been proposed for the downscaling process [73] - [77], and a novel methodology is presented in Chapter 3. The proposed downscaling model, however, is formulated as a supervised learning technique where measurements exist for the training of the model. For long term planning studies such as siting analyses, reanalysis data is typically used as measurement data is not available. An alternative from the proposed model is therefore required for the meso to micro-scale downscaling of wind speed data.

Spatial wind speed models have been used to empirically derive suitable estimates of statistical distributions describing the instantaneous micro-scale wind speeds based on certain assumptions. Gibescu *et al.* [73] demonstrated a technique to determine the spatial wind speed profile using a Gaussian filter. This method requires the estimation of the spatial standard deviation where only the area of the wind farm, the number of turbines, and a decay factor are known. The decay factor is derived empirically by estimating the parameters of an exponential fit for the relation describing the decreasing covariance with increasing distance between location pairs. The values for the decay factor vary by timescale, terrain complexity and climate, as is evident from the conflicting values reported in literature [82], [83].

Norgaard and Holttinen [77] proposed a multi-turbine power curve approach which models the spatial wind speed dispersion at a site using a Gaussian statistical distribution with a standard deviation related to the wind farm dimension and local turbulence intensity. Although the methodology relies on a number of assumptions, it performs well for modelling spatial wind speed distributions where no measurement data are available. This method offers the most generalised approach for modelling conceptual wind farms where none exist for comparative purposes.

5.2.3 Survival Analysis

Survival analysis is a branch of statistics that employs risk prediction modelling to determine the time to an event of interest. The term survival analysis stems from early application of the methodology in clinical trials to derive the probability of survival until a time t_i [101]. Survival analysis differs from other regression analyses in the sense that it incorporates information about the time to events. The model is not only used to evaluate the time to events, but also to examine the relation between the survival time and specified covariates.

The survival function, $S(t_i)$, describes the probability that a subject, or proportion of subjects, from the population under test will survive beyond time t_i, and is defined by the relationship [102]

$$S(t_i) = P(T^p > t_i), \quad 0 < t_i < \infty, \quad T^p > 0, \tag{5.3}$$

where T^p is a continuous random variable representing the time to the occurrence of an event, or survival time. Alternatively, $S(t_i)$ can be interpreted as the probability that an event of interest will not occur by time t_i. It follows that for a test population of a given size, the survival function output will decrease with time as events occur.

The event times, denoted by T^p, have a probability density function, $f(t_i)$, defined as [103]

$$f(t_i) = \lim_{\Delta t_i \to 0} \frac{P(t_i \leq T^p \leq t_i + \Delta t_i)}{\Delta t_i}. \tag{5.4}$$

Function $f(t_i)$ expresses an unconditional instantaneous failure rate that describes the probability of the frequency of events over time. The instantaneous probability of an event occurring is then described by the relation between the survival function, $S(t_i)$, and the probability density function, $f(t_i)$, as [103]

$$h(t_i) = \frac{f(t_i)}{S(t_i)} = \lim_{\Delta t_i \to 0^+} \frac{P(t_i \leq T^p \leq t_i + \Delta t_i \mid T^p \geq t_i)}{\Delta t_i}. \tag{5.5}$$

The instantaneous risk of an event at time t_i, given that there have been no prior events, is given by the hazard function, $h(t_i)$.

Many semi-parametric survival analysis models have been proposed in literature since the initial model proposed by Cox [104], [105]. The most popular of these, namely the Proportional Hazards (PH) model, is implemented in this investigation [106]. The standard form of the Cox regression model is given by

[104]

$$h(t_i, X) = h_0(t_i)e^{\beta X}, \tag{5.6}$$

where β denotes the parameter coefficient estimate for the effect of the covariate, X. The baseline hazard function, $h_0(t_i)$, is unspecified and describes the risk when the covariate X = 0. The $e^{\beta X}$ term incorporates the relative risk into the model, which adjusts the baseline risk proportionately at all durations as it does not include time. By way of example, (5.6) could be used to model the probabilistic, empirical estimation of instantaneous risk, $h(t_i)$, for HWSS events at a wind farm. The baseline hazard function, $h_0(t_i)$, is non-parametric and unspecified, meaning it is empirically fitted to the historical occurrences of HWSS without any assumptions as to the nature of the data. The seasonal occurrence may be included as a covariate, X, which may have one of four values, representing summer, autumn, winter, and spring. The relative risk term, $e^{\beta X}$, acts multiplicatively on the baseline hazard, meaning it adjusts the empirically derived baseline risk either up or down for each season, X. The formulated model requires validation before the results may be accepted. The proportionality criterion must be satisfied, and each of the seasons must be statistically significant.

In instances where more than one covariate is available, (5.6) is amended to

$$h(t_i, X) = h_0(t_i) \cdot e^{(\beta_1 X_1 + \beta_2 X_2 + \beta_3 X_3)}. \tag{5.7}$$

The proportionality assumption of the PH model necessitates that the hazard functions of two observational groups be constant over time. Consequently, the effect of explanatory variables may be determined independent of the unspecified baseline hazard function by means of the comparison of the two observational groups. This yields the hazard ratio HR, which is analogous to relative risk. The hazard ratio is formally defined from (5.6) as the ratio of two hazard functions [103]

$$HR = \frac{h_1}{h_2} = \frac{h_0(t_i)e^{\beta X_a}}{h_0(t_i)e^{\beta X_b}} = e^{\beta(X_a - X_b)}, \tag{5.8}$$

$$X = \{x \mid x = X_a \cup X_b\}, \tag{5.9}$$

where h_1 is the hazard function for group 1, and h_2 is the hazard function for group 2. The covariates X_a and X_b denote two groups of observational subsets for a covariate, X.

The HR may be used for a relative estimation of risk between sites. To accomplish this, the covariate, X, is selected as the group of wind farm sites, where the subset covariates, X_a and X_b, denote two separate wind farms with their own hazard functions. In (5.9), wind farm X_b is the referent site meaning that the hazard ratio is returned as a relative risk for wind farm X_a with respect to wind farm X_b. As the hazard ratio returns an odds ratio, the relative probability of an event occurring, HR_P, is therefore defined as [107]

$$HR_P = 100\left(\frac{HR}{1+HR}\right). \tag{5.10}$$

A hazard ratio of 3 therefore indicates that there is a 3:1 chance, or a 75 % probability, that an event with occur at wind farm X_a before an event will occur wind farm X_b.

The foundational PH assumption must be tested in order to determine the degree of the estimated coefficients validity. Violation of this assumption for a specified covariate will return an over-estimated relative risk for an increasing hazard ratio, and vice-versa. Multiple extensions to the model have been developed to cater for time-varying effects of covariates should they depart from the PH assumption.

- The covariate may be stratified by factors, or levels. This is primarily reserved for when the effect of the covariate is not of interest [103]. Stratification forces the model to fit a different baseline hazard function to each strata.
- A beta step function can be used to split the dataset at the juncture where proportionality is violated. The dataset may be spliced into multiple intervals to fit different coefficient estimates in each for a disjointed relative risk assessment [108].
- An interaction term can be introduced into the model to render the covariate time-dependent [108], [109].

5.3 Model Topology

5.3.1 Overview

Figure 60 shows a flow diagram of the proposed methodology for the characterisation of HWSS events for wind farm sites. The methodology can be summarised as follows:

- Meso-scale wind profiles are used to represent the site-specific wind resource. Each meso-scale wind speed sample is translated by a spatial wind speed model into a set of micro-scale wind speeds that is statistically representative of the wind speeds encountered by the wind turbines at a wind farm.
- An HWSS event model is implemented to translate the individual spatial wind speed profiles into HWSS events. The HWSS event model is a rule-based implementation of a typical power curve, which incorporates HWSS protection logic parameters such as cut-out and the re-cut-in hysteresis parameters. The application of this model yields a multi-turbine HWSS event profile that quantifies the number of wind turbines in HWSS mode for each sampling interval. The multi-turbine HWSS event profile is subsequently converted to a binary event profile by applying a threshold for the number, or percentage, of wind turbines in HWSS mode.
- Survival analysis, a branch of statistical models used to characterise a dataset in terms of the time to an event of interest, is applied to the HWSS event profile to determine the temporal risk for site characterisation, as well as for the comparison between sites.

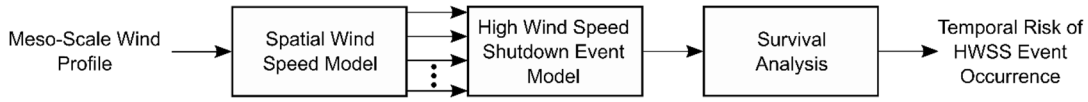

Figure 60. Flow diagram illustrating the proposed methodology for the characterisation of temporal risk of HWSS event occurrence for wind farm sites.

5.3.2 Spatial Wind Speed Model

Wind speed forecasts are typically at a meso-scale level. The wind speeds experienced at a given time by the individual wind turbines, however, varies from wind turbine to wind turbine due to the effects of site-specific parameters such as local topography, surface roughness, sheltering, and wake effects. The modelling of an HWSS event is conducted at the micro-scale level using the wind speed experienced by an individual wind turbine and a turbine power curve.

The method proposed in this study applies a representative Gaussian spatial distribution to translate a single meso-scale wind speed into a set of micro-scale wind speeds. The mean of the distribution for the i^{th} sample in time corresponds to the meso-scale wind speed, $v^m(t_i)$, while the standard deviation of the distribution, σ, is determined from the wind farm area and the local turbulence intensity [77]. In a survey of the land use statistics of 161 onshore wind farm projects in USA, Denholm et al. determined that, on average, 85 acres is required per MW of generation [110]. For the purposes of this investigation, a wind farm with an area of 100 km^2 is adopted, which equates to a total of 300 MW, or 100 3 MW wind turbines, using the aforementioned 85 acres/MW average.

The random sampling strategy proposed in Chapter 3, without turbine ranking and mapping, is utilised to derive micro-scale wind speeds for each sampling interval. The set of micro-scale wind speeds is sampled independently from the applied Gaussian spatial distribution at each t_i to derive a statistical representation of wind speeds at the site which are untied to physical locations.

5.3.3 High Wind Speed Shutdown Event Model

HWSS is a protection feature that safeguards a wind turbine against excessive mechanical forces on the blades, structure, and motor effectuated by high wind speeds. HWSS parameters are embodied in the power curve of the turbine, and vary depending on manufacturer and IEC class. A typical power curve with its associated HWSS protection logic is shown in Figure 1. A rule-based implementation of typical HWSS protection logic parameters such as cut-out and the re-cut-in hysteresis parameters is developed for the translation from micro-scale wind speeds to cut-out events. A wind speed threshold, as described in Chapter 4, is applied to the representative set of sampled micro-scale wind speeds to acquire a number of turbines in HWSS mode. The number of wind turbines in HWSS mode for the sampling timeline, T, is represented by the set N^{HWSS} given by

$$N^{HWSS} = \{n^{HWSS}(t_i)\}, \tag{5.11}$$

where $n^{HWSS}(t_i)$ denotes the number of wind turbines in HWSS mode at sampling time t_i.

An HWSS event is defined as a scenario where one or more wind turbines are in HWSS mode for one or more successive sampling intervals. An individual event is defined in terms of the start time and duration of the events, and the histogram of the number of turbines affected for each sampling time, t_i, which forms part of the event. The relationship between two successive events is represented by the time between the events. Figure 61 illustrates these parameters graphically. The start and end times are denoted by t_k^s and t_k^e respectively for the k^{th} event, t_k^d represents the duration of the k^{th} event and t_k^g denotes the gap time between the $(k-1)^{th}$ and k^{th} events.

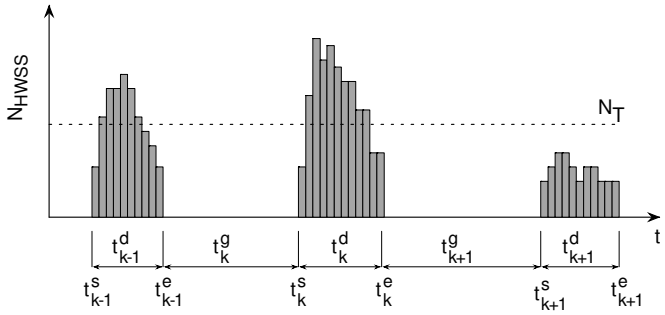

Figure 61. Graphical illustration of successive HWSS event profiles.

Variable N_T represents a threshold of a pre-determined number of wind turbines in HWSS mode, to be used for more advanced modelling of HWSS events in the sections to follow. The set of start times, T^s, is given by

$$T^s = \{t_k^s | t_k^s \in T, \quad k = 1, 2, 3, \dots, N_k\}, \tag{5.12}$$

where N_k denotes the number of events. The set of end times, T^e, is given by

$$T^e = \{t_k^e | t_k^e \in T, \ t_k^e > t_k^s, \ k = 1, 2, 3, \dots, N_k\}. \tag{5.13}$$

The set of durations, T^d, is given by

$$T^d = \{t_k^d, \ k = 1, 2, 3, \dots, N_k\}, \tag{5.14}$$

where

$$t_k^d = t_k^e - t_k^s. \tag{5.15}$$

The gap time between the $(k-1)^{th}$ and k^{th} events, $t^g(k-1, k)$ is defined by the relationship

$$t^g(k-1, k) = \begin{cases} t_k^s & \text{for} \quad k = 1 \\ t_k^s - t_{k-1}^e & \text{for} \quad k = 2, 3, \dots, N_k \end{cases}. \tag{5.16}$$

5.3.4 Survival Analysis Model

Classical survival analysis addresses the risk of occurrence of a discrete event across a temporal scale. The severity and duration of an individual event is not represented in the analysis. The event profile shown in Figure 61 must consequently be redefined to represent events of a binary nature in order to apply survival analysis for the modelling of HWSS events. This can be achieved by defining an HWSS event in terms of a threshold of a minimum number, or percentage, of wind turbines in HWSS mode. For example, redefining an HWSS event as a minimum number of N_T wind turbines in HWSS mode returns the binary event profile. Figure 62 shows the binary event profile with the start times, end times, durations and inter-event gap times are amended accordingly.

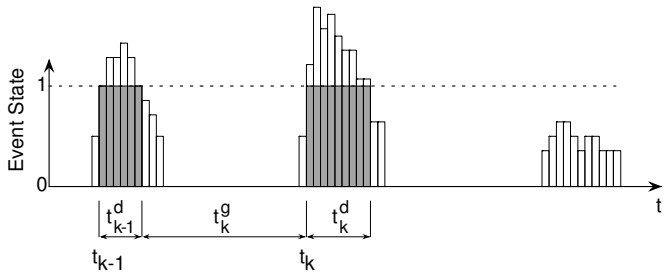

Figure 62. Graphical illustration of the binary profile of successive HWSS events derived for a pre-determined number of wind turbines in HWSS mode.

Survival analysis can be applied to an HWSS event profile to quantify the temporal characteristics of HWSS occurrences for a given location. This provides a means for comparing the risk of HWSS occurrences for different locations. The HWSS event survival profile for an individual site also has potential application in the short-term forecasting of HWSS events.

5.4 Model Implementation and Performance Assessment

5.4.1 Overview

The proposed HWSS risk assessment methodology is applied in the juxtaposition of two sites, designated as site A and B respectively, with the view to demonstrate practical application of the methodology for site characterisation and comparison. A total of 100 micro-scale spatial wind speeds, or potential wind turbine positions, are considered per site, so that the number of wind turbines in HWSS mode equals the percentage of wind turbines in HWSS mode. Single-turbine HWSS events are defined as occurrences where the micro-scale wind speed exceeds the wind turbine cut-out speed for the 15 minute sampling interval associated with the meso-scale dataset. Various HWSS levels are considered, namely 10 %, 20 %, 50 % and 100 % of the wind turbines at the site. The HWSS levels correspond to the proportionate loss of wind turbines within a wind farm due to the occurrence of HWSS.

The meso-scale wind speed profiles used in this investigation are extracted from the ‘Wind and Solar

PV Resource Aggregation Study for South Africa' numerical dataset [111]. This yields wind speed and direction profiles with a temporal resolution of 15 minutes, and a spatial resolution of 5 km by 5 km for the calendar years 2009 to 2013. The wind resource dataset was derived using the output of climate-type simulations of the WRF model [112]. The numerical dataset has been compared with measured wind speeds obtained from a number of weather masts located across the country [111]. Overall, the wind profile obtained through the WRF model shows good correlation with the corrected wind speeds measured at the masts.

5.4.2 Characterisation and Comparison of Two Sites using Survival Theory

Figure 63 shows the temporal wind speed distributions for the target sites. Site A has a mean wind speed of 7.7 ms^{-1}, while site B has a mean wind speed of 9.2 ms^{-1}. A class II wind turbine is therefore selected for site A, and a class I wind turbine is selected for site B. The cut-out and re-cut-in parameters of the individual wind turbines are determined by the turbine class. In the analysis, these parameters are taken from the selection of appropriate wind turbines from the range of available wind turbines in the Vestas 3 MW platform.

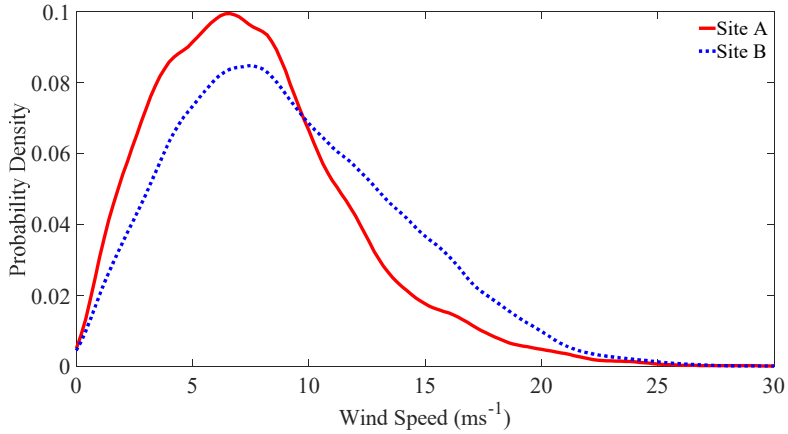

Figure 63. Wind speed probability distributions for site A and site B for the duration of the study period.

The spatial wind speed model is applied to derive micro-scale wind speed profiles that are representative of the wind speeds experienced by the wind turbines at the virtual wind farm. Two wind farms, both with an area of 100 km^2, and consisting of 100 turbines each are selected. The specification of the wind farm area allows the selection of the normalised spatial standard deviation from a range of possible values. These values range from approximately 0.09 to 0.165 depending on the local turbulence intensity [77]. A normalised spatial standard deviation of 0.15 is selected for both sites, which once multiplied by the relevant site's mean wind speed, translates to a spatial standard deviation of 1.15 ms^{-1} and 1.38 ms^{-1} for site A and site B respectively. The relevant turbine cut-out parameters are used to derive a temporal profile of HWSS events. It is assumed that all turbines at the simulated wind farm are identical in terms of class and the operational control system.

Figure 64 shows the average number of events per year for both sites versus the percentage of wind turbines in HWSS mode. Both target sites exhibit a large number of events. Site A, however, shows a higher propensity for total HWSS compared to site B. This is clear from the ratios of the occurrences of 100 % and 10 % HWSS levels for the sites. Site A transitions from 10 % HWSS to complete HWSS 25 % of the time, whereas site B makes the same transition 12 % of the time.

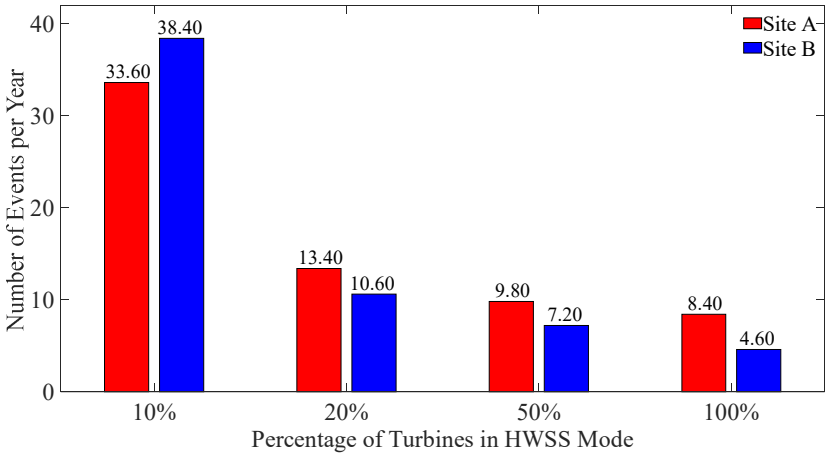

Figure 64. Average yearly number of HWSS events of 10 %, 20 %, 50 % and 100 % HWSS levels for site A and site B for the duration of the study period.

The non-parametric Kaplan-Meier estimator is employed to derive the survival function for HWSS events. This estimator is one of the most popular, simple, and robust techniques used to analyse time to event data [113]. The survival probability is determined by using the relationship [102]

$$S(t_k^s) = \prod_{k=1}^{N^k} \left\{1 - \frac{E_k(t_k^s)}{R_k(t_k^s)}\right\}, \tag{5.17}$$

where E_k denotes the number of events that have occurred up to event k from the start of the study period. The risk set, R_k, represents the cumulative number of events which have occurred over all observed time, less the number of events which have occurred until t_k^s [102]. The temporal survival probability is determined retrospectively at time t_k^s by relating the number of events which have occurred at time t_k^s to the total number of events which have occurred over the course of the study period.

Figure 65 and Figure 66 show the survival curves derived for site A and site B respectively. The spread of the curves for the two sites is noticeably different. This is consistent with the observation made from the results shown in Figure 64, which suggest a greater likelihood of transitioning to a higher HWSS level for site A compared to site B.

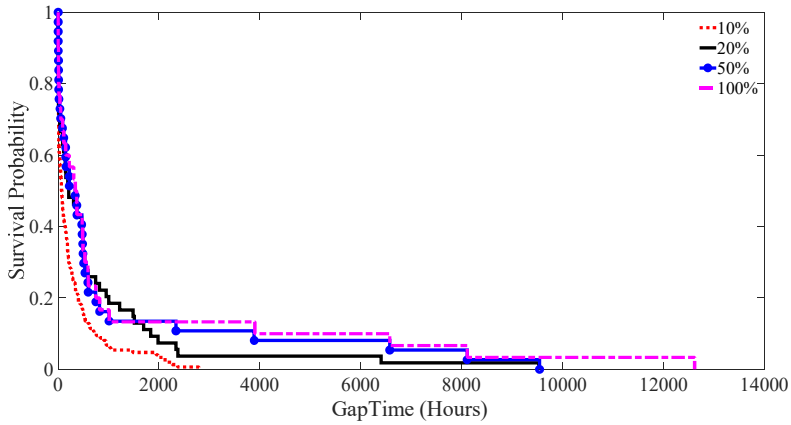

Figure 65. Survival curves for site A for 10 %, 20 %, 50 % and 100 % HWSS levels.

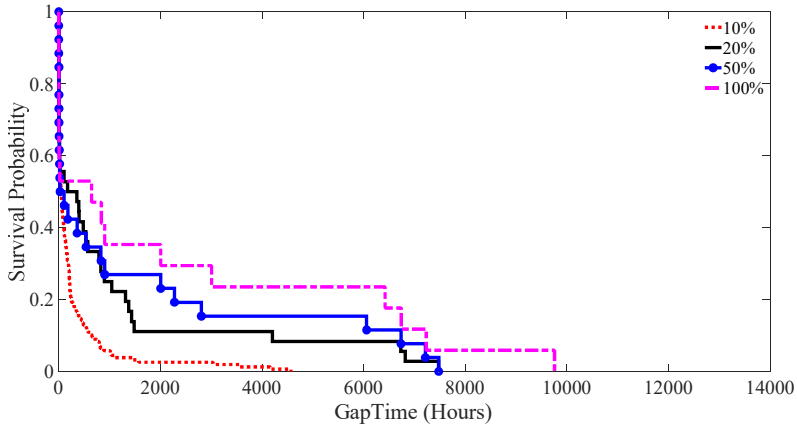

Figure 66. Survival curves for site B for 10 %, 20 %, 50 % and 100 % HWSS levels.

The variable nature of site A is apparent in the narrow spread of the survival curves, as well as the initial sharp decline of survival probability for all HWSS levels. By way of contrast, site B exhibits a comparatively gradual decline of survival probability.

Table 13 lists the median and mean survival times, which can be used to compare the survival curves. The results show that the median gap time, or the 50 % survival probability, for the HWSS levels of 20 % and 50 % is approximately equal for site A, with median total wind farm shutdown approximately 80 hours later, or 27 % of the 0 % survival probability later on the time scale. This further demonstrates the tendency of site A to proceed into high levels of HWSS. The loss of the entire wind farm for site B is less likely, with a median gap time that is approximately 80 % higher than the median gap time for a 20 % loss of the wind farm. The median for the 50 % HWSS level is unexpectedly lower than the medians for the 10 % and 20 % HWSS levels. This is as a result of the HWSS event profile being consistently situated near the 50 % threshold. Consequently, a frequent transitioning above and below the 50 % threshold occurs. Although the mean time between events for the 10 % HWSS level is approximately equivalent for both wind farms, the events at site B are more regularly spaced along a temporal scale. This is evident from the 20 %, 50 % and 100 % mean HWSS levels, as well as the shape of the survival curves.

Table 13. Mean and median gap times between events as well as the 0 % survival probability for the defined HWSS levels.

HWSS Level	Site A			Site B		
	Mean (Hours)	Median (Hours)	$S(t_i) = 0$ %	Mean (Hours)	Median (Hours)	$S(t_i) = 0$ %
10 %	320.7	104.0	2794.8	331.3	101.8	4570.8
20 %	791.9	261.4	9532.8	1136.6	397.0	7476.3
50 %	1039.7	279.9	9542.3	1445.3	64.9	7478.5
100 %	1302.6	355.3	12618.0	2349.4	741.5	9757.3

Table 13 indicates the 0 % probability gap time within which all observed events have occurred. There is, based on observation, almost 0 % probability of surviving beyond this point. Based on 5 years of data, it is highly probable that a 10 % of the wind farm will shut down within approximately 2795 hours (116 days) for site A, and 4671 hours (195 days) for site B.

Although useful for site characterisation, survival curves are not ideal for comparing risk. A relative risk comparison is therefore determined by applying the Cox PH model. Equation (5.6) is amended to yield the following:

$$h\left(t_i, X^{site}\right) = h_0(t_i)e^{\beta^{site}X^{site}}, \tag{5.18}$$

where X^{site} is a categorical variable containing site A and B, and β^{site} is an estimation of the coefficient of relative risk between sites. Site A is set as the referent, such that the parameter estimate will be returned for site B relative to site A.

A common approach is applied to assess the PH assumption through the determination of the Schoenfeld residuals, SR, which are obtained by subtracting the weighted average of the covariates in the risk set, $\overline{X_n}(t_k^s)$, from the observed values of the covariates at each failure time, t_k^s [114], as

$$SR_n(t_k^s) = X_n(t_k^s) - \overline{X_n}(t_k^s), \tag{5.19}$$

with

$$\overline{X_n}(t_k^s) = \frac{\sum_{n=1}^{N^n} X_n(t_k^s)Y_n(t_k^s)e^{\beta_n X_n}}{\sum_{n=1}^{N^n} Y_n(t_k^s)e^{\beta_n X_n}}, \tag{5.20}$$

where n denotes the number of the observation, and N^n denotes the total number of observations. The binary risk factor, Y_n, is set to one if the observation is at risk, and to zero otherwise [107].

Table 14 lists the results for the application of (5.18), as well as for the assessment of proportionality using the Schoenfeld residuals for the defined HWSS levels.

Table 14. Results for the Cox model application from (5.18) for all HWSS levels.

HWSS Level	β	HR	95% CI	p	z	SR^p
10 %	0.34	1.40	1.13 – 1.75	0.0026	3.01	3.1E-5
20 %	0.24	1.27	0.86 – 1.86	0.2300	1.20	8.2E-3
50 %	0.16	1.18	0.75 – 1.85	0.4800	0.70	0.123
100 %	-0.60	0.94	0.55 – 1.63	0.8300	-0.20	0.190

Of the HWSS levels considered, only the 10 % level is significant ($p < 0.05$). It is, furthermore, also apparent that the 10 % and 20 % HWSS levels violate the PH assumption. This is evident from the Schoenfeld residuals p-level, SR^p, which assesses deviation from the PH assumption. A significant SR^p indicates non-proportionality of the assessed covariate. Figure 67 shows the plot of the Schoenfeld residuals against transformed time for the covariate, X^{site}, at each HWSS level. The standard Kaplan-Meier time transformation is utilised [115].

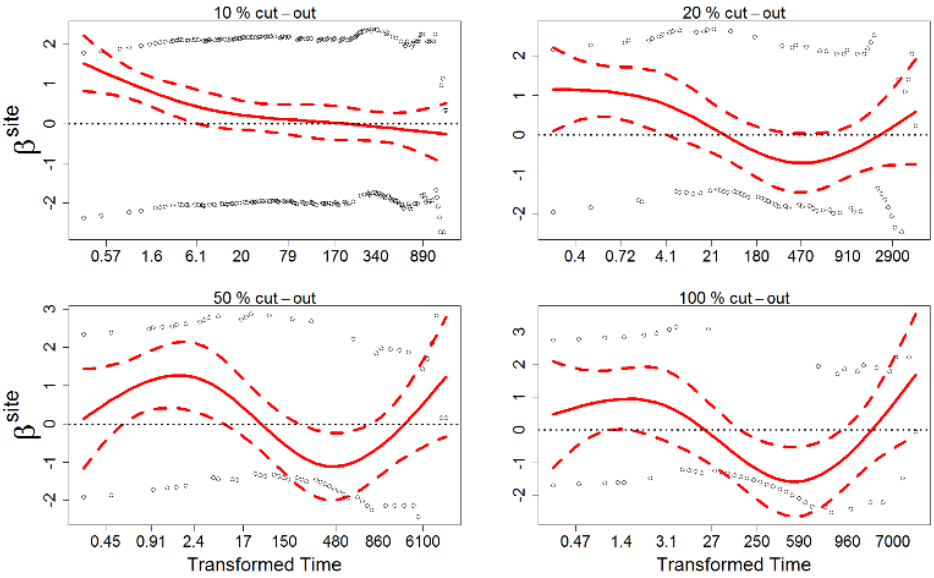

Figure 67. Schoenfeld residuals versus transformed time for all defined HWSS levels.

The dichotomous nature of X^{site} results in a band division in the β^{site} estimates. For each HWSS level, a smoothing spline fit is applied to the residuals, with dashed lines to indicate the 95 % Confidence Interval (CI). The 10 % HWSS level exhibits a linearly decreasing trend in the fit, implying that the covariate X^{site} is time-dependent. The 20 %, 50 % and 100 % HWSS levels do not exhibit a linear temporal trend. The substantial departure from the zero-slope requirement, however, gives rise to the conclusion that the PH assumption is violated for all cases.

Violation of the PH criterion necessitates application of one of the corrective actions described in section 5.2.3. As the residuals indicate a temporal trend for the 10 % HWSS level, a time interaction term is incorporated into the model as follows:

$$h_y(t_i, X^{site}) = h_{0_y}(t_i)e^{\beta^{site}X^{site}(t_i)}, \tag{5.21}$$

where y is a stratification variable representing the year. Stratification allows for the application of a different baseline hazard function for each year to negate temporal irregularities. This results in an improved individual and global model fit. Figure 68 shows the Schoenfeld residuals for the time-variant model in (5.21) applied for the 10 % HWSS level.

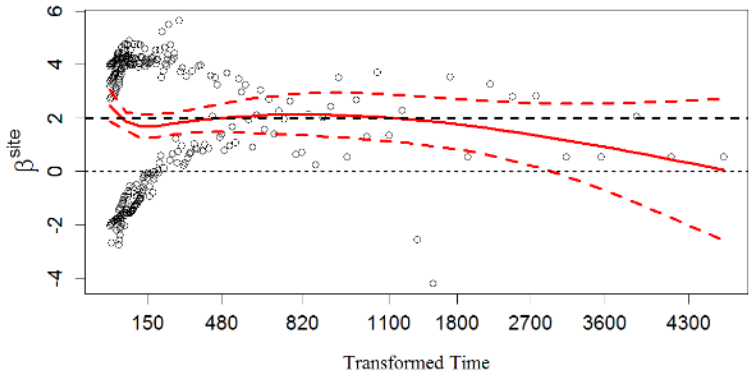

Figure 68. Schoenfeld residuals versus transformed time for the 10 % HWSS level from (5.21), which models X^{site} as time-variant.

The horizontal line at β = 2 falling within the 95 % confidence interval, coupled with a SR^p of 0.258, indicates that the new model adheres to the proportionality requirement. Additionally, X^{site} is found to be highly significant with a p-level of approximately 7.1×10^{-5}. The β^{site} and β^{tt} coefficients are 0.535 and -9.863×10^{-4} respectively, where β^{tt} signifies the effect of the linear time transform coefficient. The new hazard ratio for the 10 % HWSS level is obtained using the relationship [108], [109]

$$HR(t_k^s) = e^{(\beta^{site} + \beta^{tt} \cdot t_k^s)}. \quad (5.22)$$

Figure 69 depicts the temporal hazard ratio in (5.22) as a function of the time from the previous event. The result shows a declining exponential hazard ratio from approximately 1.7 for site B relative to site A. The break-even point is at approximately 540 hours, or 23 days, after which site A is at a higher hazard compared to site B. It follows that site B exhibits a larger short-term risk, whereas site A presents a higher longer-term risk. The time-transform technique proved ineffective for the other HWSS levels.

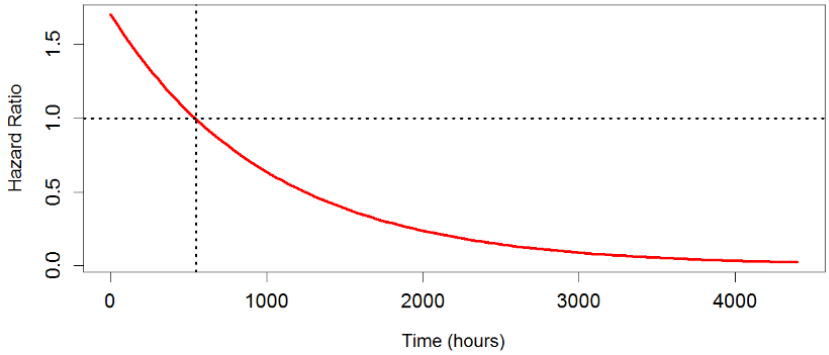

Figure 69. Hazard ratio versus time for the 10 % HWSS level for the time-variant model in (5.21).

The Cox model in (5.21) is reformulated with a beta step function for the 20 %, 50 % and 100 % HWSS levels. The dataset is split at 5 hours to produce two intervals, with interval 1 spanning from 0 to 5 hours and interval 2 covering 5 hours to the largest gap time. The 5 hour split was determined through a sensitivity analysis, with estimations selected near the gradient reversal of β^{site} in Figure 67 [116]. Each HWSS level is reassessed in terms of significance and validity. Table 15 lists the results using the beta

step function.

For all cases and their intervals, the covariate X^{site} is found to be significant ($p < 0.05$), and met the PH criterion ($SR^p >> 0.05$). The results obtained for the 20 %, 50 % and 100 % HWSS levels, similar to the 10% HWSS level, demonstrates the following:

- A high short-term risk for site B relative to site A, with an HR_P indicating a larger probability of an event occurring at site B first – in the range 72 % to 79 %.
- A low long-term risk for site B relative to site A, with an HR_P indicating a range of 15 % to 22 % probability of an event occurring at site B first.

Table 15. Cox model results with a beta step function utilised to split the data into two intervals.

HWSS Level	Interval	β^{site}	HR	HR_p	95 % CI	SR^p	p
20 %	1	1.33	3.79	79 %	1.8 - 8.1	0.81	0.0006
	2	-1.65	0.19	16 %	0.1 - 0.5	0.97	0.0003
50 %	1	0.92	2.51	72 %	1.2 - 5.5	0.70	0.0200
	2	-1.23	0.29	22 %	0.1 - 0.8	0.91	0.0140
100 %	1	0.98	2.66	73 %	1.1 - 6.5	0.75	0.0322
	2	-1.70	0.18	15 %	0.2 - 0.6	0.49	0.0042

The survival analysis methodology applied in the above case studies demonstrates an effective analysis technique for comparing the HWSS properties of two sites.

5.5 Discussion and Conclusions

A novel methodology is proposed for the characterisation and comparison of the risk of the occurrence of HWWS events, using survival analysis and the Cox PH model. It is shown that the temporal risk of HWSS events at a site can be quantified from historical data using survival analysis. This technique is subsequently extended to the quantification of the relative, empirical risk of HWSS events for two conceptual wind farms, using the Cox PH model. The model implementation and statistical validation is demonstrated for application to HWSS event analysis when the assumption of proportionality is violated. The proposed methodology has wide application. Although the methodology is demonstrated for HWSS events, it can be applied for any event of interest, including defined ramp-rate exceedances, drop below cut-in, events defined in terms of power generation thresholds, etc.

Chapter 6

Conclusions and Proposals for Further Research

6.1 Overview

The proliferation of wind energy has introduced variability and uncertainty into the power mix. The mitigation of residual ramp-rate requirements has recently gained attention due to potential consequences of frequency instability in grids with increasing penetration levels. Despite the recent attention on ramping phenomena, the case of High Wind Speed Shutdown (HWSS) has not been investigated sufficiently as motivated in Chapter 1.

Two distinct outcomes are targeted in this dissertation:

- The development of a short-term operational forecasting model which is capable of forecasting the number of turbines in HWSS mode.
- The modelling, quantification, and comparison of the relative risk of HWSS events.

6.2 Development of a Short-Term Operational Forecasting Model

6.2.1 Overview

A methodology is proposed for the forecasting of HWSS events using a hybrid forecasting model. Numerical Weather Prediction (NWP) models are utilised to generate meso-scale ensemble wind speed forecasts, which are synthesised using two techniques. The resulting meso-scale forecast is downscaled to wind speeds at individual turbines using two approaches, namely an Artificial Neural Network (ANN) model and a novel statistical downscaling technique. A novel HWSS event model is subsequently applied to predict the number of turbines in HWSS mode. The novel contributions resulting from this work are listed in the following subsections

6.2.2 Ensemble Synthesis using the Mean-Variance Portfolio Theorem

The Mean-Variance Portfolio Theorem (MVPT) is implemented and evaluated for the synthesis of multi-model ensemble forecasts towards a supervised target, namely the wind speed measured at an on-site meteorological mast. The results are compared to a two-layered ANN implementation. It is shown that the MVPT performs superior to the averaging of the multi-model ensemble wind speeds, with a Mean Absolute Error (MAE) skill score of approximately 5 % over the best-performing NWP model. The ANN implementation performs superior in terms of accuracy, with a MAE skill score of approximately 8.3 % over the best-performing NWP model. The MVPT approach, however, executes approximately 24-30 times faster compared to the ANN model for the considered dataset and model topologies. The novel MVPT methodology thus has good potential for application with large ensembles,

or where computational expedience is a consideration.

6.2.3 Development of a Statistical Downscaling Technique

A novel statistical downscaling technique is proposed to translate a meso-scale wind speed into multiple archetypal profiles that are statistically representative of the turbine wind speeds at a utility-scale wind farm. The methodology employs a Monte Carlo simulation comprising an optimisation loop with a random sampling process of an optimised site-specific spatial wind speed distribution, a turbine ranking and mapping procedure, as well as an optimisable random generator seed. The optimisation procedure is implemented to return different spatial wind speed distributions, partitioned by the wind flow conditions associated with different seasons. It is shown that the proposed method performs well, with a MAE of approximately 0.8 ms^{-1} for any given season.

The proposed methodology has potential application in studies where a meso-scale wind speed profile has to be translated into site-specific power output profiles for individual turbines, including medium and long-term studies to determine capacity factor, short-term forecasting of power generation profiles in an operational context, and specialised applications such as forecasting the risk of HWSS events.

6.2.3.1 Optimised Site-Specific Spatial Wind Speed Profiles

The proposed methodology for deriving optimal spatial wind speed distributions represents a novel contribution. As demonstrated in literature, site-specific wind speed distributions are used extensively in the determination of equivalent wind farm power curves. The derivation of multiple optimised distributions that are partitioned according to wind flow conditions has potential application in wind farm site characterisation, as well as for forecasting applications.

6.2.3.2 Tempro-Spatial Partitioning

The tempro-spatial partitioning of wind flow data represents a unique approach. In this investigation, wind farm data is partitioned into discrete wind speed and wind direction ranges in order to encapsulate the spatial variability experienced by wind turbines due to wind speed and wind direction changes. Temporal partitions are further applied to isolate seasonal meteorological processes. The results obtained demonstrate that the tempro-spatial partitioning yields favourable results in the sense that different statistical features are found for the optimised spatial wind speed distributions. The results, furthermore, show a similar MAE for the individual turbine wind speed errors across all seasons.

6.2.3.3 Turbine Ranking Model for the Bijective Mapping of Wind Speeds

A novel turbine ranking model is developed as a means to map the statistically sampled wind speeds to wind turbines based on wind flow conditions. An ANN model is trained and validated on a test dataset for subsequent use in the estimation of the ascending order of wind speed magnitudes at the site.

6.2.4 Short-Term Forecasting of Wind Speed Threshold Events

The forecasting of high wind speed events has received limited attention in literature. Two novel approaches are implemented and evaluated for the short-term forecasting of the number of turbines exceeding a pre-determine threshold at a utility-scale wind farm.

An ANN model is proposed to translate an input meso-scale forecast directly into a number of wind turbines in event mode. It is demonstrated that the formulated ANN model is adept at forecasting both frequent and infrequent events using an input parameter set comprising a wind speed ensemble, and a wind direction forecast. The results show that this model is capable of forecasting infrequent events with a limited dataset at the cost of a large number of false alarms. The model is adept at forecasting mid to large events, but does not produce a skilful forecast for small events.

The proposed statistical downscaling model is utilised in the forecasting of the number of turbines exceeding a pre-determined threshold at a large wind farm. The meso-scale ensemble wind speed forecast is improved for high wind speeds using an original approach, namely an intermediary ANN model with a custom loss function to penalise the errors at high wind speeds. The results demonstrate that this approach yields a marginally improved forecast with fewer false alarms.

6.3 Modelling, Quantification, and Comparison of Relative Risk of HWSS Events

A novel methodology is proposed to empirically evaluate the risk of loss of generation due to HWSS events at a given site, based on simulated, or measured, historicity. This proposed methodology aims to provide a framework to quantify the risk of HWSS events for individual sites as well as for geographic regions to guide strategic and investment decisions. The model topology incorporates a spatial wind speed downscaling model, an HWSS event model, and a risk assessment model based on the theory of survival analysis. The model is implemented and results are presented for two selected sites from a meso-scale reanalysis dataset. Site comparison is performed using survival models to determine the relative temporal risk of HWSS occurrence between two target sites for various HWSS event levels. The results show that the temporal risk of HWSS events at a singular site can be quantified from historical data using survival analysis. This has potential merit for forecasting applications. This technique is subsequently extended to the quantification of the relative, empirical risk of HWSS events for multiple wind farms using the Cox PH model. Lastly, model development and statistical validation is demonstrated for application to HWSS event analysis when the assumption of proportionality is violated. Although the methodology is demonstrated for HWSS events, it can be applied for any event of interest, such as defined ramp-rate exceedances, and drop below cut-in.

6.4 Proposals for Further Research

This research has uncovered potential avenues for further investigation. The following topics have been

identified:

- Generation of synthetic ensembles for synthesis using the MVPT.

The generation of synthetic ensembles has received attention in literature. Synthetic ensembles can be created using a WRF forecast as a guide, or by using historical forecasting errors. It is postulated that the application of the MVPT can add a contribution to the synthesis of these ensembles, due to its ability to incorporate a large number of input wind speeds into its optimisation algorithm, as well as for its computational expedience. The MVPT could, alternatively, be utilised for a principal component analysis, or alternatively, for the weight initialisation of an ANN model for synthesis of the ensemble wind speeds into a singular, more accurate forecast.

- Optimising the spatial partitions for the proposed statistical downscaling technique.

The proposed statistical downscaling method currently employs a static partitioning of the data into 4 wind speed, and 8 wind direction ranges. Further research is planned for the optimisation of the partitioning methodology using clustering and other techniques.

- The short-term forecasting of power band probabilities for wind farm applications.

The model topologies investigated in this dissertation are essentially spatial forecasting models in that they inherently account for the micro-scale spatial effects for an averaged sampling interval. The trained models are capable of learning the meso to micro-scale transfer function using measured nacelle wind speed data. The ability of these models, the ANN model in particular, to forecast the probability of wind farm power output within discretised bands is targeted for investigation. Custom loss functions could potentially be utilised to improve the power forecast for certain bands of interest, i.e. high power bands.

- Short-term forecasting of HWSS events using survival analysis.

Survival analysis is utilised, in its original form, to forecast life expectancy based on empirical evidence, i.e. the relationship between the predictand and a set of environmental covariates. This is analogous to the forecasting of the time to the occurrence of events at a wind farm for given environmental variables such as forecast data, time of day, time from the previous event, etc. An investigation is planned into the potential utilisation of survival models for regression forecasting for wind farm applications.

- Generation of relative risk maps of HWSS potential.

The proposed survival analysis techniques can, in principle, be extended to derive the relative risk for a large number of wind farm sites. Parametric survival models are, furthermore, targeted for the derivation of relative temporal risk. The risk of HWSS, and other events such as ramping, can be visualised in the form of geographical maps. This output could potentially inform siting practices.

- Hybrid short-term forecasting of ramp rates using a novel statistical downscaling technique.

Ramp-rate forecasting for the day ahead is identified as an area for further research using the models developed in this dissertation.

6.5 List of Research Publications

This research has generated the following publications:

- M. Groch and H. J. Vermeulen, "Modeling High Wind Speed Shut-Down Events using Meso-Scale Wind Profiles and Survival Analysis," *IEEE Transactions on Power Systems,* Early Access.
- M. Groch and H. J. Vermeulen, "Short-Term Ensemble NWP Wind Speed Forecasts using Mean-Variance Portfolio Optimization and Neural Networks," *2019 IEEE International Conference on Environment and Electrical Engineering and 2019 IEEE Industrial and Commercial Power Systems Europe (EEEIC / I&CPS Europe)*, Genova, Italy, 2019, pp. 1-6.
- M. Groch and H. J. Vermeulen, "Ramp-Rate Risk Characterization and Comparison using Survival Theory," *2019 10th International Renewable Energy Congress (IREC)*, Sousse, Tunisia, 2019, pp. 1-6.
- M. Groch and H. J. Vermeulen, "Wind Speed Event Forecasting using a Hybrid WRF and ANN model," *2019 9th International Conference on Power and Energy Systems (ICPES)*, Perth, Australia, 2019. Accepted
- M. Groch and H. J. Vermeulen, "Multi-Point Locational Wind Speed Estimation from Meso-Scale Wind Speeds for Wind Farm Applications," *2019 9th International Conference on Power and Energy Systems (ICPES)*, Perth, Australia, 2019. Accepted
- C. Y. Janse van Vuuren, H. J. Vermeulen, and M. Groch, "Optimal Siting of Wind Energy Capacity for Minimum Residual Load Variance," *2019 9th International Conference on Power and Energy Systems (ICPES)*, Perth, Australia, 2019. Accepted

References

[1] N. Kumar, P. Besuner, S. Lefton, D. Agan and D. Hileman, "Power Plant Cycling Costs," National Renewable Energy Laboratory, Denver, CO, USA, 2012.

[2] H. Auer and R. Haas, "On integrating large shares of variable renewables into the electricity system," *Energy,* vol. 115, no. 3, pp. 1592-1601, 2016.

[3] A. Dimitrovski and K. Tomsovic, "Impact of Wind Generation Uncertainty on Generating Capacity Adequacy," in *9th International Conference on Probabilistic Methods Applied to Power Systems (PMAPS)*, Stockholm, Sweden, 2006.

[4] S. O. George, H. B. George and S. V. Nguyen, "Risk Quantification Associated with Wind Energy Intermittency in California," *IEEE Trans. Power Syst.,* vol. 24, no. 4, pp. 1937-1944, 2011.

[5] B. J. Kirby, J. Dyer , C. Martinez, R. A. Shoureshi, R. Guttromson and J. Dagle, "Frequency COntrol Concerns in the North American Electric Power System," Oak Risge National Laboratory, TN, USA, 2002.

[6] P. Coughlan, J. O'Sullivan and N. Kamaluddin, "High Wind Speed Shutdown Analysis," in *Universities Power Engineering Conference (UPEC)*, London, U.K., 2012.

[7] H. MacDonald, G. Hawker and K. Bell, "Analysis of Wide-Area Availability of Wind Generators During Storm Events," in *2014 International Conference on Probabilistic Methods Applied to Power Systems (PMAPS)*, Durham, UK, 2014.

[8] N. K. Detlefsen, P. E. Sorensen and P. B. Eriksen, "Managing critical weather conditions in a large-scale wind based European power system — The twenties project," in *2011 IEEE Power and Energy Society General Meeting*, Detroit, MI, USA, 2011.

[9] N. A. Cutululis, M. Litong-Palima and P. E. Sorensen, "Offshore Wind Power Production in Critical Weather Conditions," in *European Wind Energy Conf. and Exhibition (EWEA)*, Vancouver, BC, Canada, 2013.

[10] M. Marquis, J. Wilczak, M. Ahlstrom, J. Sharp, A. Stern, J. Charles Smith and S. Calvert, "Forecasting the Wind to Reach Significant Penetration Levels of Wind Energy," *Amer. Meteor. Soc.,* vol. 91, pp. 1159-1171, 2011.

[11] M. I. Ahlstrom and R. M. Zavadil, "The Role of Wind Forecasting in Grid Operations and

Reliability," in *IEEE/PES Trans. and Distr. Conf. Exposition*, Dalian, China, 2005.

[12] A. Costa, A. Crespo, J. Navarro, G. Lizcano, H. Madsen and E. Feitosa, "A review on the young history of the wind-power short-term prediction," *Renewable and Sustainable ENergy Reviews,* vol. 12, pp. 1725-1744, 2008.

[13] C. Gallego-Castillo, A. Cuvera-Tejero and O. Lopez-Garcia, "A review on the recent history of wind power ramp forecasting," *Renewable and Sustainable Energy Reviews,* vol. 52, pp. 1148-1157, 2015.

[14] C. W. Potter, E. Grimit and B. Nijssen, "Potential benefits of a dedicated probabilistic rapid ramp event forecast tool," in *2009 IEEE/PES Power Systems Conference and Exposition*, Seattle, WA, USA, 2009.

[15] National Grid, "High Wind Speed Shutdown Workgroup Report," National Grid, 2013.

[16] S. S. Soman, H. Zareipour, O. Malik and P. Mandal, "A review of wind power and wind speed forecasting methods with different time horizons," in *North American Power Symposium*, Arlington, TX, USA, 2010.

[17] A. M. Foley, P. G. Leahy, A. Marvuglia and E. J. McKeogh, "Current methods and advances in forecasting of wind power generation," *Renewable Energy,* vol. 37, pp. 1-8, 212.

[18] J. Olauson, M. Bergkvist and J. Ryden, "Simulating intra hourly wind power fluctuationson a power system level," *Wind Energy,* vol. 20, no. 6, 2016.

[19] N. Troy, D. Flynn and M. O'Mally, "The importance of sub-hourly modelling with a high penetration of wind generation," in *Proc. IEEE Power Energy Soc. General Meeting*, San Diego, CA, USA, 2012.

[20] I. Orlanski, "A Rational Subdivision of Scales for Atmospheric Processes," *Bulletin American Meteorology Society,* vol. 56, no. 5, pp. 527-530, 1975.

[21] B. Barbosa de Alencar, C. De Mattos Affonso, R. C. Limao de Oliveira, J. L. Moya Rodriguez, J. C. Leite and J. C. Reston Filho, "Different Models for Forecasting Wind Power Generation: Case Study," *Energies,* vol. 10, no. 12, 2017.

[22] M. Lei, L. Shiyan, J. Chuanwen, L. Hongling and Z. Yan, "A review on the forecasting of wind speed and generated power," *Renewable and Sustainable Energy Reviews,* vol. 13, pp. 915-920, 2009.

[23] G. Giebel, R. Brownsword, G. Kariniotakis, M. Denhard and C. Draxl, "The State-of-the-art in short term prediction of wind power: A literature overview," Riso DTU, Denmark, 2011.

[24] L. Landberg, G. Giebel, H. A. Nielsen, T. Nielsen and H. Madsen, "Short-term Prediction - An Overview," *Wind Energy,* vol. 6, pp. 273-280, 2003.

[25] (NCAR), National Center for Atmosheric Research, "The Weather Research and Forecasting Model," [Online]. Available: https://www.mmm.ucar.edu/weather-research-and-forecasting-model. [Accessed 12 03 2019].

[26] E. M. Carlini, G. Giannuzzi, C. Pisani, A. Vaccaro and D. Villacci, "Physical and statistical downscaling for wind power forecasting," in *Proc. Int. Symposium Power Electronics, Electrical Drives, Automation and Motion (SPEEDAM)*, Anacarpi, Italy, 2016.

[27] M. Bilal, K. Solbakken and Y. Birkelund, "Wind speed and direction predictions by WRF and WindSim coupling over Nygardsfjell," *J. Phys.: Conf. Ser.,* vol. 753, pp. 1-9, 201.

[28] A. J. Deppe and W. A. Gallus Jr., "A WRF Ensemble for Improved Wind Speed Forecasts at Turbine Hub Height," *Weather and Forecasting,* vol. 28, no. 1, pp. 212-228, 2013.

[29] Chang and W. Y., "A Literature Review of Wind Forecasting Methods," *J. Power Energy Engineering,* vol. 2, pp. 161-168, 2014.

[30] Y. Zhang, J. Wang and X. Wang, "Review on probabilistic forecasting of wind power generation," *Renewable and Sustainable Energy Reviews,* vol. 32, pp. 255-270, 2014.

[31] National Center for Atmospheric Research, "WRF-ARW V3: User's Guide," 2017.

[32] W. C. Skamarock, J. B. Klemp, J. Dudhia, D. O. Gill, D. M. Barker, M. G. Duda, X. Huang, W. Wang and J. G. Powers, "A Description of the Advanced Research WRF Model Version 3.," June 2008. [Online]. Available: https://opensky.ucar.edu/islandora/object/technotes%3A500/datastream/PDF/view. [Accessed 20 April 2019].

[33] J. Zhao, Z. Guo, Z. Su, Z. Zhao, Z. Xiao and F. Liu, "An improved multi-step forecasting model based on WRF ensembles and creative fuzzy systems for wind speed," *Applied Energy,* vol. 162, pp. 808-826, 2016.

[34] S. S. Eide and J. B. Bremnes, "Bayesian Model Averaging for WInd speed Ensemble Forecasing using Wind Speed and Direction," *American Meteorological Society,* pp. 2217-2227.

[35] M. Abuella and B. Chowdhury, "Random Forest Ensemble of Support Vector Regression for Solar Power Forecasting," in *Innovative Samrt Grid Technologies*, Washington, DC, USA, 2017.

[36] M. Surcel, I. Zawadski and M. K. Yau, "On the Filtering Properties of Ensemble Averaging for Storm-Scale Precipitation Forecasts," *American Meteorological Society,* pp. 1093-1105, 2014.

[37] P. Pinson and R. Hagedorn, "Verification of the ECMWF ensemble forecasts of wind speed against analyses and observations.," *Meteorological Applications,* vol. 19, pp. 484-500, 2012.

[38] H. Markowitz, "Portfolio Selection," *The Journal of Finance,* vol. 7, no. 1, pp. 77-91, 1952.

[39] G. West, "An Introduciton to Modern Portfolio Theory: Markowitz, CAP-M, APT and Black-Litterman," Financial modelling Agency, 2006.

[40] L. J. Gitman, C. J. Zutter, W. Elali and A. Al Roubaie, "Chapter 5 Risk and Return," in *Principles of Managerial Finance*, Essex, England, Pearson, 2006, p. 234.

[41] C. M. Baby, K. Verma and R. Kumar, "Short term wind speed forecasting and wind energy estimation: A case study of Rajasthan," in *2017 International Conference on Computer, Communications and Electronics (Comptelix)*, Jaipur, India, 2017.

[42] H. Holttinen, J. Miettinen and S. Sillanpaa, "Wind power forecasting accuracy and uncertainty in Finland," VTT Technical Research Centre of Finland, Espoo, Finland, 2013.

[43] J. Manero, J. Bejar and U. Cortes, ""Dust in the Wind...", Deep Learning Application to Wind Energy Time Series Forecasting," *Energies,* vol. 12, no. 12, pp. 1-20, 2019.

[44] D. Siuta, G. West and R. Stull, "WRF Hub-Height wind Forecast Sensitivity to PBL Scheme, Grid Length, and Initial Condition Choice in Complex Terrain.," *American Meteorology Society,* vol. 32, no. 2, pp. 493-509, 2017.

[45] National Centres for Environmental Information, "Global Forecast System (GFS)," National Oceanic and Atmospheric Administration (NOAA), [Online]. Available: https://www.ncdc.noaa.gov/data-access/model-data/model-datasets/global-forcast-system-gfs. [Accessed 10 04 2019].

[46] A. N. Hahmann, C. Lennard, J. Badger, C. L. Vincent, M. C. Kelly, P. J. H. Volker, B. Argent and J. Refslund, "Mesoscale modeling for the Wind Atlas of South Africa (WASA) project," DTU Wind Energy, Denmark, 2015.

[47] National Center for Atmonspheric Research, "Frequently Asked Questions: Miscellaneous," 04 05 2016. [Online]. Available: http://www2.mmm.ucar.edu/wrf/users/FAQ_files/Miscellaneous.html. [Accessed 27 04 2019].

[48] NCAR UCAR: Earth Observing Laboratory., "Wind Direction Quick Reference," [Online]. Available: https://www.eol.ucar.edu/content/wind-direction-quick-reference.

[49] F. Castellani, D. Terzi, K. S. Hansen and J. S. Rodrigo, "Analyzing wind farm efficiency on complex terrains," in *Journal of Physics: Conference Series*, Copenhagen, Denmark, 2014.

[50] K. Xie, H. Yuang, B. Hu and C. Li, "Optimal layout of a wind farm considering multiple wind directions," in *International Conference on Probabilistic Methods Applied to Power Systems (PMAPS)*, 2014.

[51] E. Cali, B. Lange, J. Dobschinski, M. Kurt, C. Moehrlen, B. Lange, U. Focken and K. Rohrig, "Artificial neural network based Wind Power Forecasting using a multi-model approach," in *7th International Workshop on Large Scale Integration of Wind Power and on Transmission Networks for Offshore Wind Farms*, Madrid, Spain, 2008.

[52] Y. Degeilh and C. Singh, "A quantitative approach to wind farm diversification and reliability," *Electrical Power and Energy Systems,* vol. 33, no. 2, pp. 303-314, 2011.

[53] F. J. Santos-Alamillos, D. Pozo-Vasquez, J. A. Ruiz-Arais, V. Lara-Fanego and J. Tovar-Pescador, "A methodology for evaluating the spatial variability of wind energy resources: Application to assess the potential contribution of wind energy to baseload power," *Renewable Energy,* vol. 69, pp. 147-156, 2014.

[54] C. Lowery and M. O'Malley, "Optimizing wind farm locations to reduce variability and increase generation," in *Int. Conf. Prob. Methods Applied Power Syst. (PMAPS)*, 2014.

[55] M. K. McWilliam, G. C. Kooten and C. Crawford, "A method for optimizing the location of wind farms," *Renewable Energy,* vol. 48, pp. 287-299, 2012.

[56] F. J. Santos-Alamillos, N. S. Thomaidis, J. Usaola-Garcia, J. A. Ruiz-Arias and D. PozoVasquez, "Exploring the mean-variance portfolio optimization approach or planning wind repowering actions in Spain," *Renewable Energy,* vol. 106, pp. 335-342, 2017.

[57] B. Pfaff, Financial Risk Modelling and Portfolio Optimization with R, New Delhi: Wiley, 2013.

[58] M. Groch and H. J. Vermeulen, "Short-Term Ensemble NWP Wind Speed Forecasts using Mean-Variance Portfolio Optimization and Neural Networks," in *International Conference on Environmental and Electrical Engineering*, Genova, Italy., 2019.

[59] G. Mu, M. Yang, D. Wang, G. Yan and Y. Qi, "Spatial dispersion of wind speeds and its influence on the forecasting error of wind power," *J. Mod. Power Syst. and Clean Energy,* 2015.

[60] H. Certinay, F. A. Kuipers and A. N. Guven, "Optimal siting and sizing of wind farms," *Renewable Energy,* vol. 101, pp. 51-58, 2017.

[61] "Best Practice Guidelines for Mesoscale Wind Mapping Projects for the World Bank," 2010. [Online]. Available: https://www.esmap.org/sites/esmap.org/files/MesodocwithWBlogo.pdf..

[62] F. Castellani, D. Astolfi, L. Terzi, K. S. Hansen and J. S. Rodrigo, "Analysing wind farm

efficiency on complex terrains," in *in Proc. J. Phys.: Conf. Ser.*, Copenhagen, Denmark, 2014.

[63] J. P. Deane, G. Drayton and B. P. O. Gallachoir, "The impact of sub-hourly modelling in power systems with significant levels of renewable generation," *Appl. Energy,* vol. 113, pp. 152-158, 2014.

[64] S. Salcedo-Sanz, A. M. Perez-Bellido, E. G. Ortiz-Garcia, A. Portilla-Figueras, L. Prieto and D. Paredes, "Hybridizing the fifth generation mesoscale model with artificial neural networks for short-term wind speed prediction," *Renewable Energy,* vol. 34, pp. 1451-1457, 2009.

[65] F. Castellani , D. Astolfi, M. Mana, M. Burlando, C. Meissner and E. Piccioni, "Wind Power Forecasting Techniques in complex terrain: ANN vs. ANN-CFD hybrid approach," *J. Phys.: Conf. Ser.,* vol. 753, pp. 1-10, 2016.

[66] L. Li, Y. Q. Liu, Y. P. Yang, S. Han and Y. M. Wang, "A physical approach of the short-term wind power prediction based on CFD pre-calculated flow fields," *J. Hydrodyn.,* vol. 2, no. 1, pp. 56-61, 2013.

[67] S. Li, D. C. Wunsch, E. A. O'Hair and M. G. Giesselmann, "Using neural networks to estimate wind turbine power generation," *IEEE Trans. Energy Convers.,* vol. 16, no. 3, pp. 276-282, 2001.

[68] B. Alonzo, R. Plougonven, M. Mougeot, A. Fischer, A. Dupre and P. Drobinski, "From Numerical Weather Prediction outputs to Accurate Local Surface Wind Speed: Statistical Modeling Forecasts," in *Forecasting and Risk Management for Renewable Energy*, Paris, France, 2017.

[69] D. Fasbender and T. B. M. J. Ouarda, "Spatial Bayesian Model for Statistical Downscaling of AOGCM to Minimum and Maximum Daily Temperatures," *Journal of Climate,* vol. 23, no. 19, pp. 5222-5242, 2010.

[70] A. I. Estanqueiro, R. F. Aguiar, J. A. G. Saraiva, R. M. G. Castro and J. M. F. D. Jesus, "On the effect of utility grid chracteristics on wind park power output fluctuations," in *in Proc. British Wind Energy Conf.*, York, 1993.

[71] M. Shinozuka and C. M. Jan, "Digital simulations of random processes and its applications," *J. Sound Vib.,* vol. 25, no. 1, pp. 111-128, 1972.

[72] J. Mann, "Wind field simulation," *Prob. Eng. Mech.,* vol. 13, no. 4, pp. 269-282, 1998.

[73] M. Gibescu, A. J. Brand and W. L. Kling, "Estimation of Variability and Predictability of Large-Scale Wind Energy in the Netherlands," *Wind Energy,* vol. 12, pp. 241-260, 2008.

[74] P. E. Sorensen, A. D. Hansen and P. A. C. Rosas, "Wind models for simulation of power fluctuations from wind farms," *J. Wind Eng. Ind. Aerodyn.,* vol. 90, pp. 1381-1402, 2002.

[75] P. E. Sorensen, N. A. Cutululis, A. Vigueras-Rodriguez, L. E. Jensen, J. Hjerrild, M. H. Donovan and H. Madsen, "Power fluctuations from large wind farms," *IEEE Trans. Power Syst.,* vol. 22, no. 3, pp. 958-965, 2007.

[76] P. E. Sorensen, N. A. Cutululis, A. Vigueras-Rodriguez, H. Madsen, P. Pinson, L. E. Jensen, J. Hjerrild and M. Donovan, "Modelling of power fluctuations from large offshore wind farms," *Wind Energy,* vol. 11, pp. 29-43, 2008.

[77] P. B. Norgaard and H. Holttinen, "A multi-turine power curve approach," in *in Proc. Nordic Wind Power Conf.*, Goteborg, Sweden, 2004.

[78] M. He, L. Yang, J. Zhang and V. Vittal, "A Spatio-Temporal Analysis Approach for Short-Term Forecast of Wind Farm Generation," *IEEE Trans. Power Syst.,* vol. 29, no. 4, pp. 1611-1622, 2014.

[79] A. J. Lamadrid, W. Jeon, H. Lu and T. Mount, "The Case for a Simple Two-Sided Electricity Market," in *Int. Conf. Syst. Sciences*, Hawaii, 2017.

[80] E. Gil, J. Toro and G. Gutierrez-Alcaraz, "Day-ahead reserve scheduling approaches under wind uncertainty," in *IEEE Power and Energy Soc. Gen. Meeting*, 2017.

[81] G. Giebel, "On the benefits of distributed generation of wind energy in Europe," PhD Dissertation, Dept. Phys., Univ. Oldenburg, Oldenburg, Germany, 2000.

[82] L. Landberg, M. A. Hansen, K. Vesterager and W. Bergstrom, "Implementing wind forecasting at a utility," Rise National Laboratory, Rosklde, Denmark, 1997.

[83] H. Holttinen, "Hourly wind power fluctuations in Nordic countries," *Wind Energy,* vol. 8, no. 2, pp. 173-195, 2005.

[84] A. J. Lamadrid, T. Mount and W. Jeon, "The Effect of Stochastic Wind Generation on Ramping Costs and the System Benefits of Storage," in *46th Hawaii Int. Conf. Syst. Sciences*, Hawaii, 2013.

[85] M. Matsumoto and T. Nishimura, "Marsenne twister: A 623-dimensionally equidistributed uniform pseudo-random number generator," *ACM Trans. Modeling Comput. Simulat.,* vol. 8, no. 1, pp. 3-30, 1998.

[86] J. Kennedy and R. Eberhart, "Particle Swarm Optimization," in *in Proc. Int. Conf. Neural Networks (ICNN'95)*, Perth, Australia, 1995.

[87] R. C. Eberhart and Y. Shi, "Particle Swarm Optimization: Developments, Applications and Resources," in *in Proc. 2001 Congr. Evol. Comput.* , Seoul, South Korea, 2001.

[88] U. Khair, H. Fahmi, S. A. Hakim and R. Rahim, "Forecasting error calculation with mean absolute deviation and mean absolute percentage error," in *in Proc. J. Phys.: Conf. Ser.*, Medan, Indonesia, 2017.

[89] S. Kim and H. Kim, "A new metric of absolute percentage error for intermittent demand forecasts," *Int. J. Forecasting,* vol. 32, no. 3, pp. 669-679, 2016.

[90] A. Bossavy, R. Girard and G. Kariniotakis, "Forecasting ramps of wind power production with numerical weather ensembles," *Wind Energy,* vol. 16, no. 1, pp. 51-63, 2013.

[91] J. W. Taylor, "Probabilistic forecasting of wind power ramp events using autoregressive logit models," *European Journal of Operations Research,* vol. 259, no. 2, pp. 703-712, 2017.

[92] M. J. Kay, N. Cutler, A. Micolich, I. MacGill and H. Outhred, "Emerging challenges in wind energy forecasting in Australia," *Australian Meteorological and Oceanographic Journal ,* vol. 58, pp. 99-106, 2009.

[93] T. Boneh, G. T. Weymouth, P. P. R. Newham, J. Bally, A. E. Nicholson and K. B. Korb, "Fog Forecasting for Melbourne Airport Using a Bayesian Decision Network," *Weather and Forecasting,* vol. 30, pp. 1218-1233, 2007.

[94] D. Zheng, M. SHi, Y. Wang, A. T. Eseye and J. Zhang, "Day-Ahead Wind Power Forecasting Using a Two-Stage Hybrid Modeling Approach Based on SCADA and Meteorological Information, and Evaluating the Impact of Input-Data Dependency on Forecasting Accuracy," *Energies,* vol. 10, 2017.

[95] A. Tesfaye, J. H. Zhang, D. H. Zheng and D. Shiferaw, "Short-Term Wind Power Forecasting Using Artificial Neural Networks for Resource Scheduling in Microgrids," *International Journal of Science and Engineering Applications ,* vol. 5, no. 3, pp. 144-151, 2016.

[96] M. Mana, M. Burlando and C. Meißner, "Evaluation of two ANN Approaches for the Wind Power Forecast in a Mountainous Site," *International Journal of Renewable Energy Research,* vol. 7, no. 4, pp. 1629-1638, 2017.

[97] F. Cassola, M. Burlando, M. Antonelli and C. F. Ratto, "Optimization of the Regional Spatial Distribution of Wind Power Plants to Minimize the Variability of Wind Energy Input into Power Supply Systems," *J. Appl. Metrology and Climatology,* vol. 47, no. 12, p. 30993116, 2008.

[98] J. Cunha and P. Ferreira, "Designing Electricity Generation Portfolios using the Mean-Variance

Approach," *Int. J. Sust. Energy planning Manage.,* vol. 4, pp. 17-30, 2014.

[99] A. Staid and S. D. Guikema, "Risk Analysis for U.S. Offshore Wind Farms: The Need for an Integrated Approach," *Risk Analysis,* vol. 35, no. 4, pp. 587-593, 2015.

[100] J. C. Hansen, N. G. Mortensen, T. Cronin, M. Nielsen, A. N. Hahmann, J. Badger and X. G. Larsén, "Wind Atlas for South Africa (WASA) – Best practice guide for application of WASA," DTU Wind Energy, 2014.

[101] R. Singh and K. Mukhopadhyay, "Survival analysis in clinical trials: Basics and must know areas," *Perspectives Clinical Res.,* vol. 2, no. 4, pp. 145-148, 2011.

[102] D. Machin, Y. B. Cheung and M. K. B. Parmar, Survival Analysis: A Practical Approach. 2nd ed., Hoboken, New Jersey, USA: John Wiley & Sons Ltd., 2006.

[103] M. Mills, Introducing Survival and Event History Analysis, London: Sage Publications Ltd., 2012.

[104] D. R. Cox, "Regression Models and Life-Tables," *J. Royal Stat. Soc.,* vol. 34, no. 2, pp. 187-220, 1972.

[105] S. Guo and D. Zeng, "An overview of semiparametric models in survival analysis," *J. of Stat. Planning and Inference,* pp. 1-16, 2013.

[106] P. Allison, Handbook of Data Analysis, London: Sage Publications Ltd., 2011.

[107] S. L. Spruance, J. E. Reid, M. Grace and M. Samore, "Minireview. Hazard Ratio in Clinical Trials," *Antimicrobial Agents and Chemotherapy,* vol. 48, no. 8, pp. 2787-2792, 2004.

[108] C. A. Bellera, G. MacGoran, M. Debled, C. Tunon de Lara, V. Brouste and S. Mathoulin-Pelissier, "Variables with time-varying effects and the Cox model: Some statistical concepts illustrated with a prognostic factor study in breast cancer," *BMC Medical Res. Methodology,* vol. 10, no. 20, 2010.

[109] T. Therneau, C. Crowson and E. Atkinson, "Using Time Dependent Covariates and Time Dependent Coefficients in the Cox Model," 2019.

[110] P. Denholm, M. Hand, M. Jackson and S. Ong, "Land-Use Requirements of Modern Wind Power Plants in the United States," National Renewable Energy Laboratory, Golden, CO, USA, 2009.

[111] K. Knorr, B. Zimmermann, S. Bofinger, A. K. Gerlach, T. Bischof-Niemz and C. Mushwana, "Wind and Solar Resource Aggregation Study for South Africa," Fraunhofer IWES, 2016.

[112] A. Hamman, C. Lennard, J. Badger, C. Vincent, M. Kelly, P. Volker, B. Agent and J. Refslund, "Mesoscale modeling for the Wind Atlas of South Africa (WASA) project," DTU Wind Energy, Denmark, 2015.

[113] I. Etikan, S. Abubakar and R. Alkassim, "The Kaplan Meier Estimate in Survival Analysis," *Biometrics and Biostatics Int. J.,* vol. 5, no. 2, 2017.

[114] W. W. M. Abeysekera and M. R. Sooriyarachchi, "Use of Schoenfeld's global test to test the proportional hazards assumption in the Cox proportional hazards model: an application to a clinical study," *J. Nat. Sci. Found. Sri Lanka,* vol. 37, no. 1, pp. 41-51, 2008.

[115] S. Park and D. J. Hendry, "Reassessing Schoenfeld residual tests of proportional hazards in political science event history analyses," *American Journal of Political Science,* vol. 59, no. 4, pp. 1072-1087, 2015.

[116] Z. Zhang, J. Reinikainen, K. A. Adeleke, M. E. Pieterse and C. G. M. Groothuis-Outshoorn, "Time-varying covariates and coefficients in Cox regression models," *Annals of Translational Medicine,* vol. 6, no. 7, 2018.